

AD-A209 051

Report No. PSI-9098/TR-737

AFGL-TR-87-0337

SPACE SHUTTLE PLASMA/FLOWFIELD INTERACTIONS

James C. Person  
George E. Caledonia  
David Resendes  
Guy Weyl  
Andrew T. Lintz  
Daniel E. Hastings

Physical Sciences Inc.  
Research Park, P.O. Box 3100  
Andover, MA 01810

11 December 1987

Scientific Report No. 1

APPROVED FOR PUBLIC RELEASE; DISTRIBUTION UNLIMITED

Prepared for  
AIR FORCE GEOPHYSICS LABORATORY  
Air Force Systems Command  
United States Air Force  
Hanscom AFB, MA 01731-5000

DTIC  
ELECTE  
JUN 20 1989  
S D

89 6 20 002

"This technical report has been reviewed and is approved for publication"

Allen Rubin

ALLEN RUBIN  
Contract Manager

Charles P. Pike

CHARLES P. PIKE  
Branch Chief

FOR THE COMMANDER

Rita C. Sagalyn

RITA C. SAGALYN  
Division Director

This report has been reviewed by the ESD Public Affairs Office (PA) and is releasable to the National Technical Information Service (NTIS).

Qualified requestors may obtain additional copies from the Defense Technical Information Center. All others should apply to the National Technical Information Service.

If your address has changed, or if you wish to be removed from the mailing list, or if the addressee is no longer employed by your organization, please notify AFGL/DAA, Hanscom AFB, MA 01731. This will assist us in maintaining a current mailing list.

Do not return copies of this report unless contractual obligations or notices on a specific document requires that it be returned.

UNCLASSIFIED

SECURITY CLASSIFICATION OF THIS PAGE

## REPORT DOCUMENTATION PAGE

1a. REPORT SECURITY CLASSIFICATION UNCLASSIFIED			1b. RESTRICTIVE MARKINGS None	
2a. SECURITY CLASSIFICATION AUTHORITY N/A since unclassified			3. DISTRIBUTION/AVAILABILITY OF REPORT Approved for public release; distribution unlimited	
2b. DECLASSIFICATION/DOWNGRADING SCHEDULE N/A since unclassified				
4. PERFORMING ORGANIZATION REPORT NUMBER(S) PSI-9098/TR-737			5. MONITORING ORGANIZATION REPORT NUMBER(S) AFGL-TR-87-0337	
6a. NAME OF PERFORMING ORGANIZATION Physical Sciences Inc.		6b. OFFICE SYMBOL (If applicable) 8K 901	7a. NAME OF MONITORING ORGANIZATION Air Force Geophysics Laboratory	
6c. ADDRESS (City, State and ZIP Code) Research Park, P.O. Box 3100 Andover, MA 01810			7b. ADDRESS (City, State and ZIP Code) Hanscom Air Force Base, MA 01731-5000	
8a. NAME OF FUNDING/SPONSORING ORGANIZATION Air Force Geophysics Lab.		8b. OFFICE SYMBOL (If applicable) FQ7620	9. PROCUREMENT INSTRUMENT IDENTIFICATION NUMBER F-19628-85-C-0098	
8c. ADDRESS (City, State and ZIP Code) Air Force Systems Command, USAF Hanscom Air Force Base, MA 01731-5000			10. SOURCE OF FUNDING NOS.	
			PROGRAM ELEMENT NO. 65502F	PROJECT NO. 5501
11. TITLE (Include Security Classification) Space Shuttle Plasma/Flowfield Interactions				
12. PERSONAL AUTHOR(S) Person, James C.; Caledonia, George E.; Resendes, David; Weyl, Guy; Lintz, Andrew T.; and Hastings, Daniel E.				
13a. TYPE OF REPORT Scientific Report No.1		13b. TIME COVERED FROM 860912 TO 870911		14. DATE OF REPORT (Yr., Mo., Day) 1987 December 11
				15. PAGE COUNT 144
16. SUPPLEMENTARY NOTATION				
17. COSATI CODES			18. SUBJECT TERMS (Continue on reverse if necessary and identify by block number)	
FIELD	GROUP	SUB. GR.	Space shuttle, Ions, Electrons, Ionization mechanisms, Plasma simulation, Langmuir probe, Critical Ionization Velocity. (1d)	
19. ABSTRACT (Continue on reverse if necessary and identify by block number)  Plasma phenomena around large space structures operating in low earth orbit are examined. Our particular emphasis is on phenomena that may lead to enhanced plasmas as a result of gas injections. The ultimate goal is the design of a Shuttle-borne experiment to study plasma enhancement. One section provides a review of Langmuir probe theory with a re-analysis of some of the measurements performed on earlier Shuttle flights. The major portion of the report describes modeling the critical ionization velocity (CIV) phenomenon, which has been proposed as an important source of plasma enhancement when neutral molecules have a sufficiently large velocity relative to a magnetized plasma. We present an analysis of the linear dispersion theory for both cold plasmas and plasmas that have thermal energy. <del>We present</del> results from computer simulations using a particle-in-cell code to simulate the plasma				
20. DISTRIBUTION/AVAILABILITY OF ABSTRACT UNCLASSIFIED/UNLIMITED <input checked="" type="checkbox"/> SAME AS RPT. <input type="checkbox"/> DTIC USERS <input type="checkbox"/>			21. ABSTRACT SECURITY CLASSIFICATION Unclassified	
22a. NAME OF RESPONSIBLE INDIVIDUAL Dr. Allen G. Rubin			22b. TELEPHONE NUMBER (Include Area Code) (617) 377-2933	22c. OFFICE SYMBOL AFGL/PHK

effects that result when a beam of fast ions interacts with a background plasma. Most of these simulations include molecular physical effects such as charge exchange, elastic collisions, and excitation and ionization by fast electrons. An appendix gives the Phase 0/1 Accident Risk Assessment report for the experiment design.

1. Checklist for  
 2. 1975-1980  
 3. 1981-1985  
 4. 1986-1990  
 5. 1991-1995  
 6. 1996-2000  
 7. 2001-2005  
 8. 2006-2010  
 9. 2011-2015  
 10. 2016-2020  
 11. 2021-2025  
 12. 2026-2030  
 13. 2031-2035  
 14. 2036-2040  
 15. 2041-2045  
 16. 2046-2050  
 17. 2051-2055  
 18. 2056-2060  
 19. 2061-2065  
 20. 2066-2070  
 21. 2071-2075  
 22. 2076-2080  
 23. 2081-2085  
 24. 2086-2090  
 25. 2091-2095  
 26. 2096-2100  
 27. 2101-2105  
 28. 2106-2110  
 29. 2111-2115  
 30. 2116-2120  
 31. 2121-2125  
 32. 2126-2130  
 33. 2131-2135  
 34. 2136-2140  
 35. 2141-2145  
 36. 2146-2150  
 37. 2151-2155  
 38. 2156-2160  
 39. 2161-2165  
 40. 2166-2170  
 41. 2171-2175  
 42. 2176-2180  
 43. 2181-2185  
 44. 2186-2190  
 45. 2191-2195  
 46. 2196-2200  
 47. 2201-2205  
 48. 2206-2210  
 49. 2211-2215  
 50. 2216-2220  
 51. 2221-2225  
 52. 2226-2230  
 53. 2231-2235  
 54. 2236-2240  
 55. 2241-2245  
 56. 2246-2250  
 57. 2251-2255  
 58. 2256-2260  
 59. 2261-2265  
 60. 2266-2270  
 61. 2271-2275  
 62. 2276-2280  
 63. 2281-2285  
 64. 2286-2290  
 65. 2291-2295  
 66. 2296-2300  
 67. 2301-2305  
 68. 2306-2310  
 69. 2311-2315  
 70. 2316-2320  
 71. 2321-2325  
 72. 2326-2330  
 73. 2331-2335  
 74. 2336-2340  
 75. 2341-2345  
 76. 2346-2350  
 77. 2351-2355  
 78. 2356-2360  
 79. 2361-2365  
 80. 2366-2370  
 81. 2371-2375  
 82. 2376-2380  
 83. 2381-2385  
 84. 2386-2390  
 85. 2391-2395  
 86. 2396-2400  
 87. 2401-2405  
 88. 2406-2410  
 89. 2411-2415  
 90. 2416-2420  
 91. 2421-2425  
 92. 2426-2430  
 93. 2431-2435  
 94. 2436-2440  
 95. 2441-2445  
 96. 2446-2450  
 97. 2451-2455  
 98. 2456-2460  
 99. 2461-2465  
 100. 2466-2470  
 101. 2471-2475  
 102. 2476-2480  
 103. 2481-2485  
 104. 2486-2490  
 105. 2491-2495  
 106. 2496-2500  
 107. 2501-2505  
 108. 2506-2510  
 109. 2511-2515  
 110. 2516-2520  
 111. 2521-2525  
 112. 2526-2530  
 113. 2531-2535  
 114. 2536-2540  
 115. 2541-2545  
 116. 2546-2550  
 117. 2551-2555  
 118. 2556-2560  
 119. 2561-2565  
 120. 2566-2570  
 121. 2571-2575  
 122. 2576-2580  
 123. 2581-2585  
 124. 2586-2590  
 125. 2591-2595  
 126. 2596-2600  
 127. 2601-2605  
 128. 2606-2610  
 129. 2611-2615  
 130. 2616-2620  
 131. 2621-2625  
 132. 2626-2630  
 133. 2631-2635  
 134. 2636-2640  
 135. 2641-2645  
 136. 2646-2650  
 137. 2651-2655  
 138. 2656-2660  
 139. 2661-2665  
 140. 2666-2670  
 141. 2671-2675  
 142. 2676-2680  
 143. 2681-2685  
 144. 2686-2690  
 145. 2691-2695  
 146. 2696-2700  
 147. 2701-2705  
 148. 2706-2710  
 149. 2711-2715  
 150. 2716-2720  
 151. 2721-2725  
 152. 2726-2730  
 153. 2731-2735  
 154. 2736-2740  
 155. 2741-2745  
 156. 2746-2750  
 157. 2751-2755  
 158. 2756-2760  
 159. 2761-2765  
 160. 2766-2770  
 161. 2771-2775  
 162. 2776-2780  
 163. 2781-2785  
 164. 2786-2790  
 165. 2791-2795  
 166. 2796-2800  
 167. 2801-2805  
 168. 2806-2810  
 169. 2811-2815  
 170. 2816-2820  
 171. 2821-2825  
 172. 2826-2830  
 173. 2831-2835  
 174. 2836-2840  
 175. 2841-2845  
 176. <



## TABLE OF CONTENTS

<u>Section</u>	<u>Page</u>
1.0 INTRODUCTION	1
2.0 MEASUREMENT OF ELECTRON TEMPERATURE AND DENSITY	4
2.1 ANALYSIS OF SHUTTLE PROBE DATA	9
2.2 EFFECT OF SOLAR RADIATION ON MEASURED CURRENT	10
2.3 CONCLUSIONS	12
3.0 SIMULATION OF CRITICAL IONIZATION VELOCITY EFFECTS	13
3.1 LINEAR DISPERSION THEORY OF WAVES IN A "COLD" PLASMA	14
3.1.1 Introduction	14
3.1.2 Perturbation Theory	15
3.2 ION BEAM STREAMING INTO A BACKGROUND ION-ELECTRIC PLASMA IN THE COLD PLASMA APPROXIMATION	20
3.3 COMPUTER SIMULATION OF ION BEAM STREAMING INTO A BACKGROUND ION-ELECTRON PLASMA	27
3.4 WAVES IN A "HOT" PLASMA IN A MAGNETIC FIELD	37
3.4.1 General Theory	37
3.4.2 Dispersion Relation for a "Hot" Plasma in a Magnetic Field	43
3.4.3 Parametric Study of CIV	52
3.5 COMPUTER SIMULATION OF MOLECULAR AND PLASMA EFFECTS	55
3.5.1 Introduction	55
3.5.2 Equations for CIV Process	58
3.5.3 Description of Method of Computer Simulations	60
3.5.3.1 Approximations in the Plasma Simulations	60
3.5.3.2 Approximations that Should be Tested in Further Work	64
3.5.4 Details of the Simulation of Molecular Physics	66
3.5.4.1 Method of Simulating Electron-Neutral Collisions	66
3.5.4.2 Absolute Cross Sections for Elastic and Inelastic Scattering	69

## CONTENTS (CONCLUDED)

<u>Section</u>	<u>Page</u>
3.5.4.3 Elastic Scattering Angular Distribution	69
3.5.4.4 Inelastic Scattering Angular Distribution	69
3.5.4.5 Method of Simulating Ion-Neutral Collisions	70
3.5.5 Results of Computer Simulations	72
3.5.5.1 Fraction of Electrons Heated	73
3.5.5.2 Rate of Electron Heating	80
3.5.5.3 Disposition of the Energy of the Fast Ion Beam	80
3.5.5.4 Effects of Ion-Neutral Elastic Collisions	89
3.5.5.5 Molecular Effects of Increased Neutral Density	89
3.5.5.6 Requirement for a Minimum Density of Beam Ions	90
3.5.5.7 Effects of Kinetic Energy of Fast Beam Ions	97
3.5.5.8 Importance of Charge Exchange as an Energy Source for CIV	97
3.5.6 Summary of Simulation Results	101
ACNOWLEDGMENTS	103
REFERENCES	104
APPENDIX	109

# FIGURES

<u>Figure</u>		<u>Page</u>
1.	Sheath thickness.	5
2.	Typical current versus voltage characteristic of a probe.	5
3.	Electron trajectory in the sheath.	8
4.	Current versus voltage $n = 2.6 \times 10^6 \text{ cm}^{-3}$ .	9
5.	Current versus voltage $n = 10^4 \text{ cm}^{-3}$ .	10
6.	Photoelectric yield of Au as a function of wavelength.	11
7.	Plot of the real ( $\omega_r$ ) and imaginary ( $\gamma$ ) parts of $\omega$ versus $k_x v$ .	26
8a.	Growth of the electric field energy at two angles $\psi$ between the magnetic field and beam velocity.	30
8b.	Growth of the electric field energy at two angles $\psi$ between the magnetic field and beam velocity.	31
9.	Velocity along the direction of the fast ion beam as a function of distance at a time of $199.975/\Omega_e$ .	32
10a.	Electron kinetic energy at two angles $\psi$ between $\bar{B}$ and $\bar{v}_x$ .	33
10b.	Electron kinetic energy at two angles $\psi$ between $\bar{B}$ and $\bar{v}_x$ .	34
11a.	Ion drift energy for two angles $\psi$ between $\bar{B}$ and $\bar{v}_x$ .	35
11b.	Ion drift energy for two angles $\psi$ between $\bar{B}$ and $\bar{v}_x$ .	36
12.	Coordinate system with magnetic field along the z-axis.	40
13.	Parametric dependence of maximum growth rate on ratio of beam to background number densities.	54
14.	Parametric dependence of maximum growth rate on ratio of parallel to perpendicular components of wave vector.	54
15.	Parametric dependence of maximum growth rate on ratio of electron plasma to cyclotron frequencies.	55
16.	Field energy for two runs where $f_{b0}$ is 0.5 and $E_{kb}$ is 1.	74

# FIGURES (CONCLUDED)

<u>Figure</u>		<u>Page</u>
17.	Maximum fraction of electrons heated to an energy of $I/2$ during the first 461 time units as a function of the number density of neutral molecules.	81
18.	Maximum fraction of electrons heated to an energy of $I$ during the first 461 time units as a function of the number density of neutral molecules.	82
19.	Rate of heating 0.001 of the electrons to an energy of $I/2$ as a function of the number density of neutral molecules.	83
20.	Rate of heating 0.001 of the electrons to an energy of $I$ as a function of the number density of neutral molecules.	84
21.	Fraction of total energy in the electron kinetic energy after 461 time units as a function of the number density of neutral molecules.	86
22.	Fraction of total energy in the beam ion kinetic energy after 461 time units as a function of the number density of neutral molecules.	87
23.	Fraction of total energy in the ambient ion kinetic energy after 461 time units as a function of the number density of neutral molecules.	88
24.	Number of elastic collisions of the ambient ions with neutrals during 461 time units as a function of the number density of neutral molecules.	91
25.	Number of elastic collisions of the beam ions with neutrals during 461 time units as a function of the number density of neutral molecules.	92
26.	Number of elastic collisions of the beam ions with neutrals during 461 time units as a function of the number density of neutral molecules.	93
27.	Number of charge exchange collisions of the ambient ions with neutrals during 461 time units as a function of the number density of neutral molecules.	94
28.	Number of charge exchange collisions of the beam ions with neutrals during 461 time units as a function of the number density of neutral molecules.	95



## 1.0 INTRODUCTION

This research project is directed towards examining the impact of gas injections from large space structures operating in low earth orbit. Our particular emphasis is on phenomena which may lead to enhanced plasmas about the structure.

This first annual report on the project describes several related efforts aimed to develop an understanding of the relevant plasma/flow phenomena with the ultimate goal of designing a Shuttle-borne experiment to study plasma enhancement.

One of the primary Shuttle diagnostics for studying plasma properties is the Langmuir probe. Section 2 provides a review of probe theory with a re-analysis of some of the measurements performed on earlier Shuttle flights.

A relatively detailed description of our modeling on critical ionization velocity (CIV) effects is provided in Section 3. The critical ionization velocity effect originally proposed by Alfven (1954) may be an important source of plasma enhancement around large space structures such as the Shuttle orbiter or the future space station. Papadopoulos (1984) proposed that the glow observed near the surfaces of the Shuttle was the result of electrons heated by a plasma instability produced by reflection of some of the ionospheric ions when the Shuttle moves through the ionosphere. Indeed, the ionic environment about the orbiter is observed to have periods where the ion density increases dramatically (Siskind, et al., 1984). The electron energy distribution often is not a simple Maxwellian distribution (Raitt, et al., 1984; Murphy, et al., 1986; Raitt, et al., 1987). In addition orbiter operations, such as thruster firings, flash evaporator releases, and water dumps are observed to enhance electrostatic noise and to increase the plasma density fluctuations (Pickett, et al., 1985). Thus there is evidence that plasma instabilities, and possibly CIV processes, are produced as the result of orbiter operations. If CIV processes are occurring, it is not clear if

these result from reflection of streaming ions (Papadopoulos, 1984), ionization of metastable states (McNeil, Lai, and Murad, 1987), or ionization of dimers or trimers formed during the free expansion into space (Murad, et al., 1986). Section 3 describes a model for the two stream instability which is used to gauge the importance of CIV around Shuttle.

The primary objective of this program is to conceptually design a well diagnosed injection experiment to be flown on space Shuttle for the purpose of studying the critical ionization velocity process. This experiment will concomitantly provide reliable data on the "ambient" plasma fields around the orbiter. The experiment would employ infrared active species and be deployed in conjunction with the IBSS experiment in order to take advantage of the outstanding ultra-violet and infrared radiation diagnostics available in that payload. The CIV experiment would also utilize radiation and plasma diagnostics placed within the Shuttle bay.

Specifically we propose to inject gases from the Shuttle bay in low earth orbit under conditions which should lead to enhanced plasma due to the CIV phenomena. The key is in choosing the right species to inject. Gases cool when they expand into a near vacuum, as the random motion in thermal energy is converted into directed motion. The cooling gas forms dimers, trimers, and possibly higher clusters. A dimer (or a higher cluster) has two advantages over the corresponding monomer in reducing its critical velocity ( $v_c$ ) value: it has a slightly lower ionization potential and it has twice (or  $n$  times) the mass. Thus releasing the gas under conditions where the free expansion favors production of dimers or trimers should enhance the prospects for CIV processes (Murad, et al., 1986). Our experimental gas release will form such dimers and higher clusters, and their smaller  $v_c$  values will enhance the probability that the CIV process will produce enhanced ionization.

At present we intend to inject four distinct gases. First a null injection, utilizing a rare gas such as neon. This species does not have a favorable ionization potential for fostering CIV at low earth orbital velocities of 8

km/s and thus any observed plasma fluctuations may be ascribed to perturbations due to the injected flow. Two other gases to be injected are NO and CO<sub>2</sub>. These species have both the merit of being typical rocket exhaust gases, and having dimers with ionization potentials corresponding to equivalent critical ionization velocities below orbital velocity. Indeed for ram direction injection the monomers themselves may ionize through CIV. These polar molecules and their ions exhibit infrared bands which are within the spectral range of the IBSS payload. Furthermore the bands of the neutral and ionic species may be resolved from each other. Lastly in the case of CO<sub>2</sub><sup>+</sup>, the dissociative recombination process produces electronically excited CO, whose radiation can be monitored by the AIS instrument. Thus any radiation resulting from the CIV effect directly caused by the injection of these two species may be readily monitored by the IBSS payload. The last species to be injected will be xenon which should be readily ionized by the CIV process (Mobius, et al., 1979; Axnas, 1980).

The experiment design is still in the preliminary stages. A Phase 0/1 Accident Risk Assessment report has been filed and is included as an appendix to this volume. Furthermore a Preliminary Design Review has just been completed. The viewgraphs presented at this review are provided in a separate volume.

## 2.0 MEASUREMENT OF ELECTRON TEMPERATURE AND DENSITY

The measurement of electron density ( $n_e$ ) and temperature ( $T$ ) in the Shuttle environment can readily be performed by use of a Langmuir probe. The theory of Langmuir probes under conditions where the particle mean free path is large as compared to the probe and sheath dimensions and where the effect of magnetic field on charged particle orbits is negligible is well understood (Langmuir, 1961; Chen, 1963; Schott, 1968). We show in Fig. 1 the plasma sheath thickness as a function of  $n_e$ . Since a plasma is a good conductor, the electric field will be zero inside the plasma and application of a voltage onto a probe in contact with the plasma will result in a current being drawn from the edge of the sheath. The electron gyroradius in a magnetic field ( $B$ ) of 0.3 Gauss is given by:

$$R = 11.2 \sqrt{T} \quad (\text{cm}) \quad (1)$$

where  $T$  is in eV.  $R$  varies inversely with  $B$ . The ion gyroradius will be larger by the square root of the ion to electron mass ratio. One sees from Eq. (1) that if the probe dimensions are of the order of 3 cm or less, then electrons will have straight orbits and magnetic field effects can be neglected. At low electron densities ( $n_e < 10^4 \text{ cm}^{-3}$ ) the probe when biased positively with respect to the plasma, will draw electrons from a distance so large that the magnetic field is expected to play a role in the conduction independent of probe size.

We show in Fig. 2 a typical current versus voltage characteristic. In region III the probe is biased negatively with respect to the plasma and is attracting ions. In region I the probe is biased positively and is attracting electrons. When the probe is at the sheath potential  $V_s$ , i.e., when there is no voltage difference between the probe and the plasma, the current to the probe is:

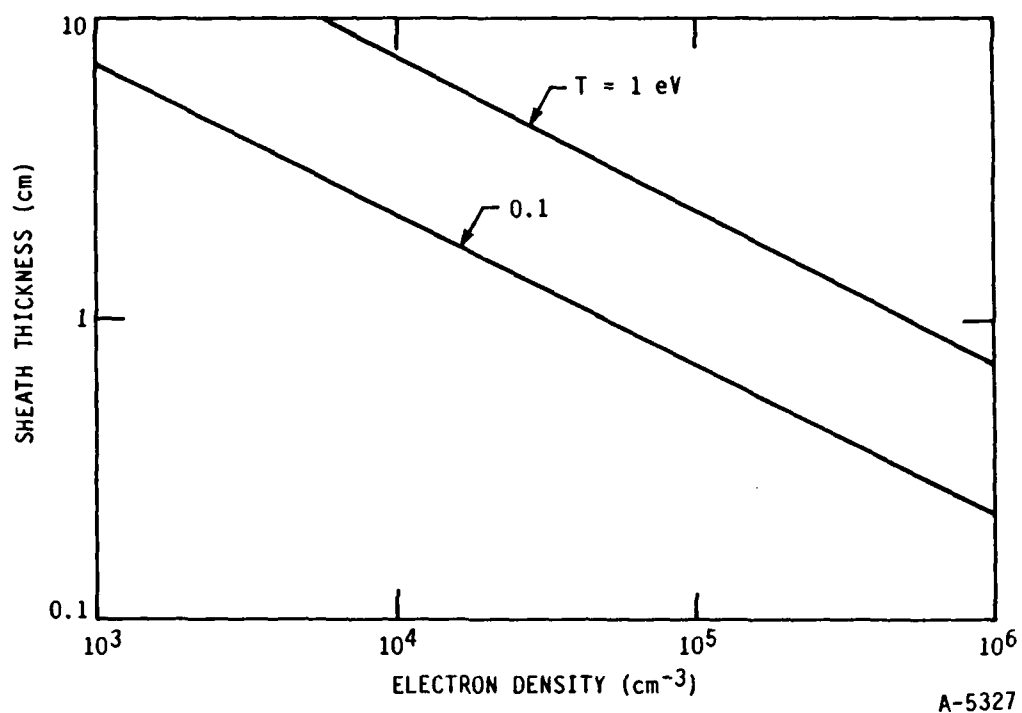


Figure 1. Sheath thickness.

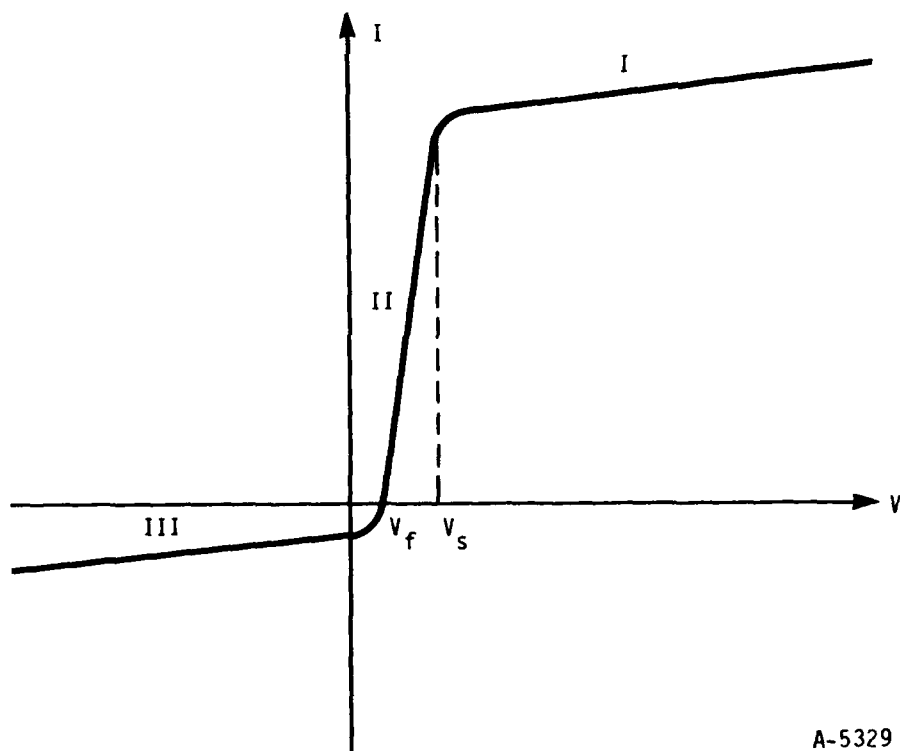


Figure 2. Typical current versus voltage characteristic of a probe.

$$I = \left| e \left[ \frac{n_i c_i}{4} - \frac{n_e c_e}{4} \right] \right| A_p \approx \frac{e n_e c_e}{4} A_p \quad (2)$$

where  $A_p$  is the area of the probe, and  $c_{i(e)}$  the mean velocity  $(8 kT/\pi m)^{1/2}$  of the ions (electrons). In the last step we used the fact that the ion current could be neglected since the electron thermal velocity is so much larger than the ion velocity. The floating potential  $V_f$  is the potential at which the ion and electron currents cancel and where the probe draws no net current. The transition region II is a region where the probe is biased negatively with respect to the plasma but not so much as to completely repel the electrons. It is a region where the current is still dominated by flow of electrons to the probe.

The maximum current that a probe can collect is:

$$I = e \frac{n_p c}{4} A_{sh} \quad (3)$$

where  $n_p$  is the plasma density ( $n_p = n_e$ ) and  $A_{sh}$  the area encompassed by the edge of the sheath. The slope of the  $I$  versus  $V$  curve in region II will yield the electron temperature, since, when electrons are repelled, it can be shown that Eq. (1) still holds with  $A_{sh}$  being equal to the probe area  $A_p$  and  $n$  varying as

$$n = n_0 \exp(-e|V|/kT)$$

where  $V$  is the (negative) potential with respect to the plasma. We therefore have

$$\frac{d \ln I}{d|V|} = - \frac{e}{kT} \quad (4)$$

Once the electron temperature is known, the electron density can be derived from the saturation current which varies proportionately with  $n_p \sqrt{T}$ . One difficulty in determining  $n_p$  exactly is that the sheath area will change with

applied voltage. When the sheath is very thin as compared to the probe dimensions then  $A_{sh}$  is practically equal to the probe area  $A_p$ , and the saturation current appears to be practically independent of probe voltage.

When the probe is attracting electrons one can calculate the current by following the electron trajectories, starting from the edge of the sheath. The geometry is shown in Fig. 3, for either a spherical probe, or an infinitely long cylindrical probe. A particle starting at the edge of the sheath at point M will hit the probe (at point N) if the angle  $\theta$  shown in the figure is less than some critical angle  $\theta_c$  which depends on the initial radial velocity  $u$ . By integrating over all  $u$  and all angles  $\theta < \theta_c(u)$  one obtains, for a spherical probe, the current:

$$I = A_p j_r F \quad (5)$$

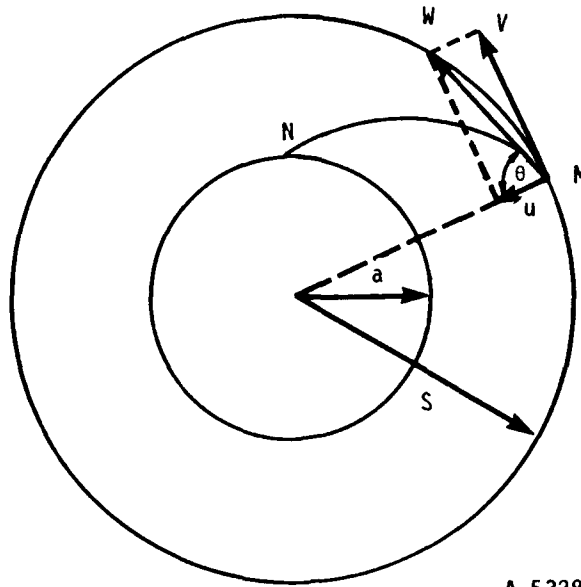
where  $A_p = 4\pi a^2$ ,  $j_r = (n_e c/4)$  and

$$F = \frac{s^2}{a^2} (1 - \exp[-\phi]) + \exp[-\phi] \quad (6)$$

with

$$\phi = \frac{a^2}{s^2 - a^2} \frac{eV}{kT} \quad (7)$$

If the sheath thickness is very small as compared to  $a$ , then, when  $eV \gtrsim kT$ ,  $\phi \gg 1$ ,  $F \approx s^2/a^2 \approx 1$ , and the current is given by Eq. (3) with  $A_{sh} = A_p$ . If  $T$  is known, then it is an easy matter to derive  $n$  from the current. If the sheath thickness is small as compared to  $a$ , we can use the Langmuir-Tonks equation for space charge limited flow in planar geometry to calculate the sheath thickness as a function of probe voltage with respect to the plasma (Cobine, 1968).



A-5328

Figure 3. Electron trajectory in the sheath.

$$I = A_p \frac{(2 e/m)^{1/2} V^{3/2}}{9\pi(s-a)^2} = 2.33 \times 10^{-6} \frac{A_p}{(s-a)^2} V^{3/2} \quad (\text{amps}) \quad (8)$$

where in the last step  $A_p$  is in  $\text{cm}^2$ ,  $V$  in volts and  $(s-a)$  in cm. Both  $s$  and  $n$  can be calculated from Eqs. (3) and (8) if  $T$  is known since  $A_{sh}/A_p = s^2/a^2$ .

When the sheath thickness is comparable to or larger than the probe radius, it is not straightforward to derive  $n$  from the saturation current, and one must solve Poisson's Equation taking into account particle trajectories with plasma density as a parameter. Only a detailed comparison of the theoretical  $I$  versus  $V$  characteristics with the measured one will yield  $n$ , once  $T$  is known.



## 2.1 ANALYSIS OF SHUTTLE PROBE DATA

Murphy, et al. (1986) used a spherical probe of radius  $a = 3$  cm to measure  $n$  and  $T$  in the Shuttle environment. They present two characteristics corresponding to  $n = 2 \times 10^6 \text{ cm}^{-3}$  and  $n = 10^4 \text{ cm}^{-3}$ . Their data is shown in Figs. 4 and 5. They calculated  $T_e$  by fitting the slope given by Eq. (4) to region II of the characteristic, after correcting the characteristic for the ion current. Because of the large velocity of the Shuttle with respect to the ionospheric plasma, the ion current will be  $I_i = n_i W \pi a^2$ , where  $W$  ( $= 8 \text{ km/s}$ ) is the Shuttle velocity with respect to the plasma. This is an order of magnitude larger current than one would draw if the probe had no motion with respect to the background plasma. Based on the electron temperature and density that they derive from their data, we calculate the sheath thickness to be 3 and 0.2 cm for  $n_e = 10^4$  and  $2 \times 10^6 \text{ cm}^{-3}$ , respectively. The sheath thickness is therefore of the order of the probe radius at the lower density. We have used Eqs. (5) to (7) to calculate the electron current as a function

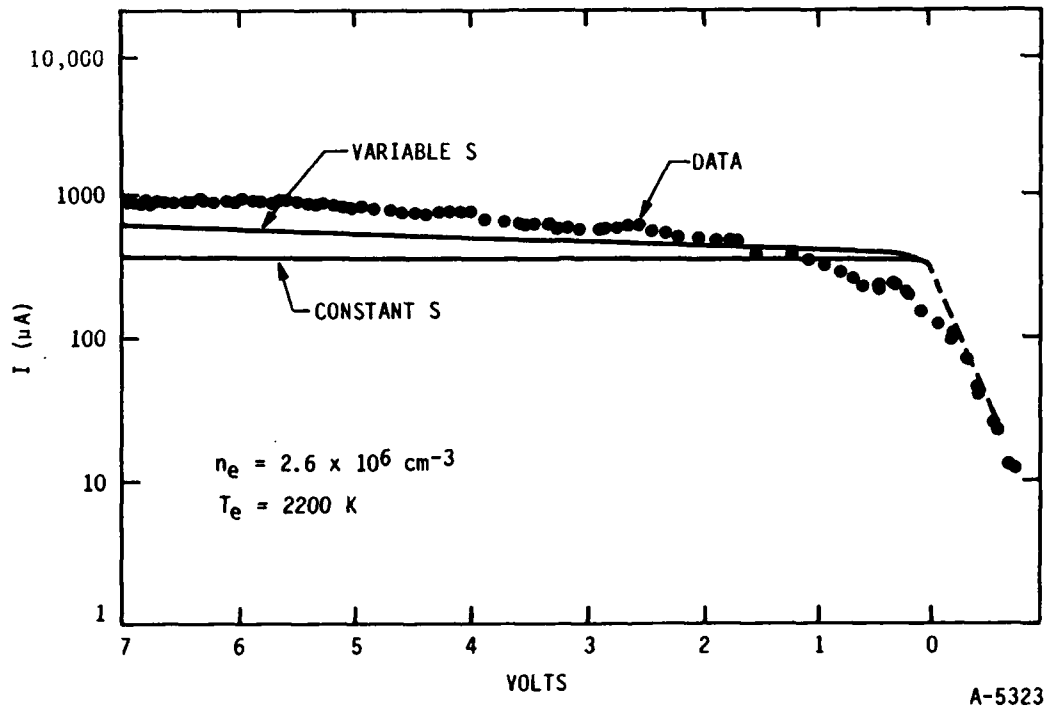


Figure 4. Current versus voltage  $n = 2.6 \times 10^6 \text{ cm}^{-3}$ .

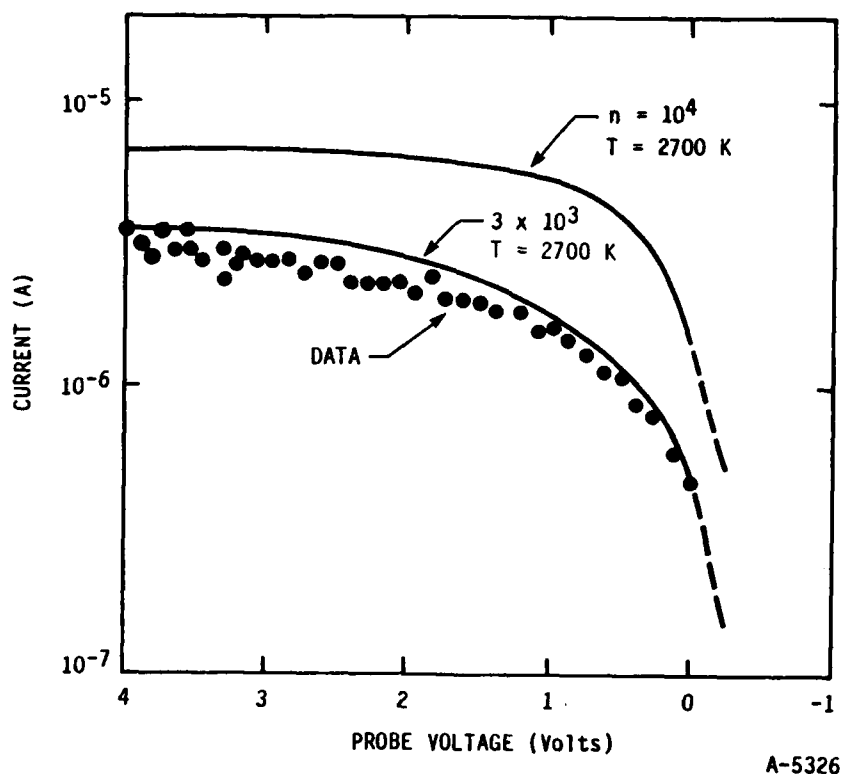


Figure 5. Current versus voltage  $n = 10^4 \text{ cm}^{-3}$ .

of  $V$  for  $V$  positive. The potential of the probe is measured with respect to the Shuttle body, however, and the potential with respect to the plasma at the location of the probe is unknown. We translated the characteristic so that the calculated current would fall on top of the measured current in the retarding region II. We took  $s-a = 3 \text{ cm}$  when  $n_e = 10^4 \text{ cm}^{-3}$  and calculated  $s$  from Eqs. (3) and (8) when  $n_e = 2 \times 10^6 \text{ cm}^{-3}$ . We see that we obtain reasonable agreement with Murphy et al.'s measurements when  $n_e = 2 \times 10^6 \text{ cm}^{-3}$ , but find a saturation current too large by a factor of three when we set  $n_e = 2 \times 10^6 \text{ cm}^{-3}$ . Our results indicate that the actual plasma density is a factor of three to four times lower than the density derived by Murphy et al.

## 2.2 EFFECT OF SOLAR RADIATION ON MEASURED CURRENT

Photoelectrons are generated by the solar XUV photons that are incident in the probe and will affect the current when the probe is biased negatively with

respect to the plasma. We calculate the effect for a gold plated probe, such as the one used by Murphy et al. (1965). Let  $\Phi_S(\lambda)$  be the solar flux in photons/cm<sup>2</sup> s per unit wavelength interval. Let  $\eta(\lambda)$  be the quantum efficiency of the electron ejection process. Integrating over the probe and over wavenumber, we calculate the following photo-electron current ( $q$  = electron charge).

$$I_S = -2\pi qa^2 \int_0^{\pi/2} \cos \theta d(\cos \theta) \int \Phi_S(\lambda) \eta(\lambda) d\lambda$$

$$I_S = \pi qa^2 \int \Phi_S(\nu) \eta(\lambda) d\lambda .$$

We show in Fig. 6 the photo-electric yield of gold (Samson, 1967). It only becomes appreciable at wavelength  $\lambda < 130$  nm. Integrating the photon efficiency times an average solar flux over  $\lambda$ , we find a photo electric current of  $\sim 8 \times 10^4$  el/cm<sup>2</sup> s leading to  $I_S = 3.6 \times 10^{-8}$  A. This current is a factor of four below the detection threshold in Murphy et al.s (1968) measurements.

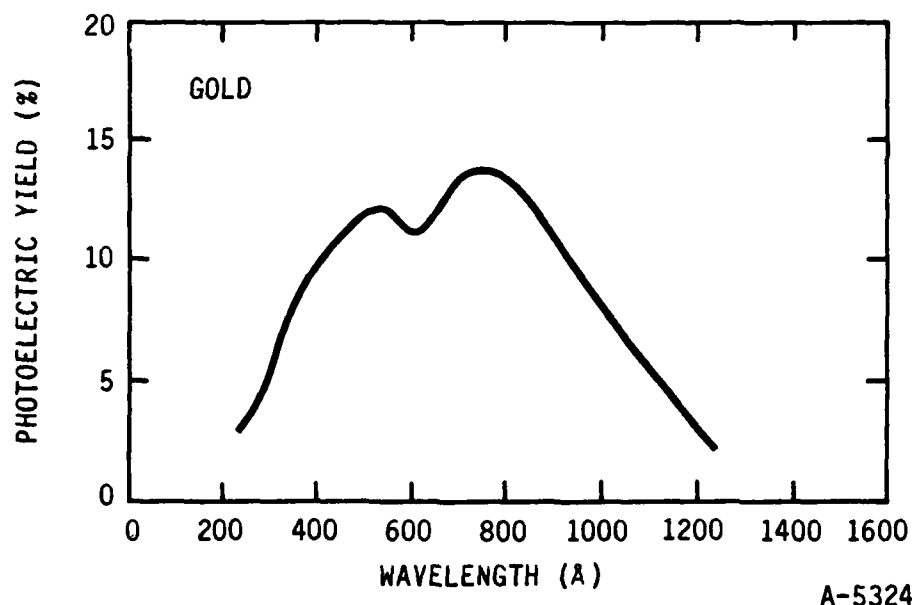


Figure 6. Photoelectric yield of Au as a function of wavelength.

### 2.3 CONCLUSIONS

Probe theory under the conditions of Murphy et al.'s (1968) experiments reproduces pretty well the experimental results at high electron densities ( $n = 2 \times 10^6 \text{ cm}^{-3}$ ) but indicates that at lower electron density ( $n = 10^4 \text{ cm}^{-3}$ ), where the sheath thickness is comparable to the probe radius, they overestimated  $n$  by a factor of three to four. The photo-electric yield of gold is shifted to short enough wavelengths that the current generated by solar illumination is below the measurement threshold.

### 3.0 SIMULATION OF CRITICAL IONIZATION VELOCITY EFFECTS

The critical ionization velocity (CIV) effect was first proposed by Alfven (1954) in the context of his model on the origin of the solar system. The proposal states that there is a rapid ionization whenever a neutral gas moves across the magnetic field with a velocity relative to a plasma exceeding the value

$$v_c = (2I/m_b)^{0.5} ,$$

where  $I$  is the ionization potential of the neutral gas and  $m_b$  is the mass of the ion formed upon ionization. There is now considerable evidence for CIV ionization at velocities near  $v_c$  from various laboratory experiments (Danielsson, 1973; Himmel et al., 1976). Recently there have been experiments with chemical releases in space (Newell, 1985). One of these shows CIV ionization (Haerendel, 1982), but others show only a small amount or do not detect any (Wescott, et al., 1986a,b; Kelley, et al. 1986; Torbert and Newell, 1986). In other releases the plasma changes could result from processes other than CIV (Sasaki, et al., 1985), or from the ion beam released (Sasaki, et al., 1986).

We have investigated CIV phenomena for conditions that can occur when a beam of neutral gas molecules is released from the Shuttle in low earth orbit. Here we are interested in modeling both the molecular phenomena and the plasma effects that result from the formation of a beam of fast ions moving across a magnetized plasma. We first present the linear dispersion theory, then we present simulation results for a simplified plasma. Next we present more linear dispersion theory for a warm plasma. We conclude with simulations of the molecular and plasma effects in combination.

### 3.1 LINEAR DISPERSION THEORY OF WAVES IN A "COLD" PLASMA

#### 3.1.1 Introduction

Here we are concerned with small amplitude wave motions of a cold ionized gas. This is one of the few plasma situations for which it is possible to give a systematic account. The cold plasma is of interest because it can support many of the varied types of wave motion which are present at non-zero temperatures, but without any of the mathematical subtleties that are inherent in a solution of the kinetic equations for a hot plasma. A cold plasma means, in this context, an unbounded, electron-ion plasma of zero thermal velocities. Such a system is actually a model, the limits of the validity of which can best be inferred from the theory for a hot plasma.

In what follows we develop the linear theory of waves in a "cold" plasma. This follows closely the text of Montgomery and Tidman (1964). The theory is subsequently applied to a situation of practical interest in the design of the space shuttle experiment to test the critical ionization velocity hypothesis.

Let us assume that each of the species of charge has a number density  $n_i$ , a velocity  $\bar{v}_i$ , no pressure gradients, and obeys an equation of continuity and an equation of motion:

$$\frac{\partial}{\partial t} n_i + \bar{\nabla} \cdot (n_i \bar{v}_i) = 0 \quad \frac{d}{dt} = \frac{\partial}{\partial t} + \bar{v} \cdot \bar{\nabla} \quad (9)$$

$$\frac{\partial}{\partial t} \bar{v}_i + \bar{v}_i \cdot \bar{\nabla} \bar{v}_i = \frac{e_i}{m_i} (\bar{E} + \frac{1}{c} \bar{v}_i \times \bar{B}) \quad (10)$$

$\bar{E}$  and  $\bar{B}$  satisfy Maxwell's equations

$$\bar{\nabla} \cdot \bar{E} = 4\pi \rho \quad \bar{\nabla} \cdot \bar{B} = 0 \quad (11)$$

$$\bar{\nabla} \times \bar{E} = -\frac{1}{c} \frac{\partial \bar{B}}{\partial t} \quad \bar{\nabla} \times \bar{B} = \frac{4\pi}{c} \bar{j} + \frac{1}{c} \frac{\partial \bar{E}}{\partial t} \quad (12)$$

(Note that we are using Gaussian units here.) The charge and current densities are:

$$\rho = \sum_i e_i n_i \quad \bar{j} = \sum_i e_i n_i \bar{v}_i \quad (13)$$

### 3.1.2 Perturbation Theory

The Eqs. (9) through (13) with appropriate initial and/or boundary conditions, determine the plasma variables of state  $n_i$  and  $\bar{v}_i$  as functions of  $\bar{x}$  and  $t$ . They are nonlinear and very difficult to solve. A perturbation-theoretic solution about a uniform equilibrium is possible, however, and useful for many purposes.

Let us assume a uniform magnetic field  $\bar{B}_0$  in the zero order system and set

$$\begin{aligned} \bar{v} &= \bar{u} + \bar{v} & \bar{E} &= \bar{E} \\ \bar{B} &= \bar{B}_0 + \bar{B} & \bar{n} &= \bar{N}_i + \bar{n} \end{aligned} \quad (14)$$

where  $\bar{u}_i$ ,  $\bar{B}_0$ , and  $\bar{N}_i$  are independent of  $\bar{x}$  and  $t$ .

Let  $\sum_i \bar{N}_i e_i = 0$ ,  $\sum_i \bar{N}_i e_i \bar{u}_i = 0$  (15)

and  $\sum_i \bar{u}_i \times \bar{B}_0 = 0$  (16)

i.e., there is no charge or current density in the zero-order system and the zero order velocities are parallel to  $\bar{B}_0$  (no force).

Substituting Eq. (14) into Eqs. (8) through (13) and keeping linear terms only gives the linear system of equations:

$$\frac{\partial}{\partial t} \bar{n}_i^{(1)} + \bar{N}_i \bar{\nabla} \cdot \bar{v}_i^{(1)} + (\bar{\nabla} \bar{n}_i^{(1)}) \cdot \bar{u}_i = 0 \quad (17)$$

$$\frac{\partial}{\partial t} \bar{v}_i^{(1)} + \bar{u}_i \cdot \nabla \bar{v}_i^{(1)} = \frac{e_i}{m_i} \left[ \bar{E}^{(1)} + \frac{1}{c} \bar{v}_i^{(1)} \times \bar{B}_0 + \frac{1}{c} \bar{u}_i \times \bar{B}^{(1)} \right] \quad (18)$$

$$\bar{\nabla} \times \bar{B}^{(1)} = \frac{4\pi}{c} \bar{j}^{(1)} + \frac{1}{c} \frac{\partial}{\partial t} \bar{E}^{(1)}, \quad \bar{\nabla} \cdot \bar{B}^{(1)} = 0 \quad (19)$$

$$\nabla \times \bar{E}^{(1)} = -\frac{1}{c} \frac{\partial}{\partial t} \bar{B}^{(1)}, \quad \bar{\nabla} \cdot \bar{E}^{(1)} = 4\pi \rho^{(1)} \quad (20)$$

where  $\bar{j}^{(1)} = \sum_i e_i (\bar{N}_i \bar{v}_i^{(1)} + \bar{n}_i^{(1)} \bar{u}_i)$  (21)

$$\rho^{(1)} = \sum_i e_i \bar{n}_i^{(1)} \quad (22)$$

The linear system (17) through (22) has constant coefficients, and may be solved using Fourier transforms in  $\bar{x}$  and  $t$ . Hence we seek solutions for which all the perturbed quantities have a dependence  $e^{i(\bar{k} \cdot \bar{x} - \omega t)}$  so that (17) through (22) become an algebraic system of linear, homogeneous equations. Initial and/or boundary conditions can be satisfied by linearly superposing these solutions into wave packets, i.e., Fourier distributions in  $\bar{k}$  and/or  $\omega$ .

Thus, we define the symmetric Fourier transform pair:

$$\bar{F}(\bar{x}, t) = \frac{1}{(2\pi)^2} \int d^3k d\omega \tilde{F}(\bar{k}, \omega) e^{i(\bar{k} \cdot \bar{x} - \omega t)} \quad (23a)$$

$$\tilde{F}(\bar{k}, \omega) = \frac{1}{(2\pi)^2} \int d^3x dt \bar{F}(\bar{x}, t) e^{-i(\bar{k} \cdot \bar{x} - \omega t)} \quad (23b)$$

Time differentiation, taking the div. and taking the curl in the direct space is equivalent to multiplying the Fourier coefficients by  $(-i\omega)$ ,  $i\bar{k}$ , and  $i\bar{k} \times$  respectively. The relations between the Fourier coefficients for (17) through (22) are:

$$-i\omega \tilde{n}_i^{(1)} + N_i i\bar{k} \cdot \tilde{v}_i^{(1)} + i\tilde{n}_i^{(1)} \bar{k} \cdot \bar{u}_i = 0 \quad (17')$$

$$-i\omega \tilde{v}_i^{(1)} + i\bar{u}_i \cdot \bar{k} \tilde{v}_i^{(1)} = \frac{e_i}{m_i} [\tilde{E}^{(1)} + \frac{1}{c} \tilde{v}_i^{(1)} \times \bar{B}_0 + \frac{1}{c} \bar{u}_i \times \tilde{B}^{(1)}] \quad (18')$$

$$i\bar{k} \times \tilde{B}^{(1)} = \frac{4\pi}{c} \tilde{j}^{(1)} - \frac{i\omega}{c} \tilde{E}^{(1)}, \quad i\bar{k} \cdot \tilde{B}^{(1)} = 0 \quad (19')$$

$$i\bar{k} \times \tilde{E}^{(1)} = \frac{i\omega}{c} \tilde{B}^{(1)}, \quad i\bar{k} \cdot \tilde{E}^{(1)} = 4\pi \tilde{\rho}^{(1)} \quad (20')$$

$$\tilde{j}^{(1)} = \sum_i e_i (N_i \tilde{v}_i^{(1)} + \tilde{n}_i^{(1)} \bar{u}_i) \quad (21')$$

$$\tilde{\rho}^{(1)} = \sum_i e_i \tilde{n}_i^{(1)} \quad (22')$$



Equations (17') through (22') are a closed set for the Fourier coefficients and could be used to solve for them, whence by integration (inverse Fourier transform), our original system of equations could be solved for the plasma variables of state (under the appropriate boundary conditions). Having assumed a normal mode solution, the linear, homogeneous system (17') through (22') gives us the normal modes (eigenvectors) and normal frequencies (eigenvalues).

In the next section we shall be interested in a case for which  $\bar{u}_i \times \bar{B}_0 \neq 0$ . The derivations presented here apply provided we do not consider  $\bar{k} = \omega = 0$ . This is not a serious limitation since we shall not be interested in transforming back to the direct space  $(\bar{x}, t)$ .

Our approach is to eliminate all perturbed variables in favor of the perturbed electric field. In this form we will obtain the dot product of a dyadic with the perturbed electric field equal to zero. The dyadic may be interpreted as the dielectric response of the plasma. Taking the curl of (20') we find

$$\begin{aligned} i\bar{k} \times (i\bar{k} \times \bar{E}^{(1)}) &= \frac{i\omega}{c} i\bar{k} \times \bar{B}^{(1)} \\ &= \frac{i\omega}{c} \left[ \frac{4\pi}{c} \sum_i e_i (N_i \bar{v}_i^{(1)}) + N_i \frac{\bar{k} \cdot \bar{v}_i^{(1)}}{\omega - \bar{k} \cdot \bar{u}_i} \bar{u}_i \right] - \frac{i\omega}{c} \bar{E}^{(1)} \end{aligned}$$

In arriving at this result we have used (19'), (21'), and (17'), respectively. This equation can be simplified by using the vector identity

$$\bar{a} \times (\bar{b} \times \bar{c}) = (\bar{a} \cdot \bar{c})\bar{b} - (\bar{a} \cdot \bar{b})\bar{c}$$

The resulting simplified equation is

$$\begin{aligned} (\omega^2 - c^2 k^2) \bar{E}^{(1)} + c^2 \bar{k} (\bar{k} \cdot \bar{E}^{(1)}) &= -4\pi i \omega \bar{j}^{(1)} \\ &= -4\pi i \omega \sum_i e_i N_i (\bar{v}_i^{(1)}) + \bar{u}_i \frac{\bar{k} \cdot \bar{v}_i^{(1)}}{(\omega - \bar{k} \cdot \bar{u}_i)} \end{aligned} \quad (24)$$

On the right hand side  $\bar{v}_i$  is still present. However, Eq. (18') (and Eq. (22')) are still at our disposal. Introducing the cyclotron frequency vector

$$\bar{\Omega}_1 \equiv \frac{e_1 \bar{B}_0}{m_1 c} , \quad (25)$$

Eq. (18') becomes:

$$-i(\omega - \bar{k} \cdot \bar{u}_1) \bar{v}_1^{(1)} = \frac{e_1}{m_1} [\bar{E}^{(1)} + \frac{1}{c} \bar{u}_1 \times \bar{B}^{(1)}] - \bar{\Omega}_1 \times \bar{v}_1^{(1)} \quad (26)$$

In this last equation,  $\bar{B}^{(1)} = \frac{c}{\omega} \bar{k} \times \bar{E}^{(1)}$  (see Eq. (20')) and hence it remains to solve for  $\bar{v}_1^{(1)}$  in terms of  $\bar{E}^{(1)}$ . We do this by first recalling the identity:

$$\bar{v}_1^{(1)} \equiv \frac{\bar{\Omega}_1 (\bar{\Omega}_1 \cdot \bar{v}_1^{(1)})}{\Omega_1^2} - \frac{\bar{\Omega}_1 \times (\bar{\Omega}_1 \times \bar{v}_1^{(1)})}{\Omega_1^2} . \quad (27)$$

Next, we take the dot and cross product of Eq. (26) with  $\bar{\Omega}_1$  trying to take advantage of Eq. (27). From the dot product of Eq. (27) with  $\bar{\Omega}_1$  we get

$$\frac{\bar{\Omega}_1 (\bar{\Omega}_1 \cdot \bar{v}_1^{(1)})}{\Omega_1^2} = \frac{\frac{e_1}{m_1}}{-i(\omega - \bar{k} \cdot \bar{u}_1)} (\bar{\Omega}_1 \cdot \bar{E}^{(1)} + \frac{1}{c} \bar{\Omega}_1 \cdot (\bar{u}_1 \times \bar{B}^{(1)})) \frac{\bar{\Omega}_1}{\Omega_1^2} .$$

Adding this result to the curl of Eq. (26) with  $\bar{\Omega}_1$  we find

$$-i(\omega - \bar{k} \cdot \bar{u}_1) \frac{\bar{\Omega}_1 \times \bar{v}_1^{(1)}}{\Omega_1^2} + \frac{\frac{e_1}{m_1}}{-i(\omega - \bar{k} \cdot \bar{u}_1)} (\bar{\Omega}_1 \cdot \bar{E}^{(1)} + \frac{1}{c} \bar{\Omega}_1 \cdot (\bar{u}_1 \times \bar{B}^{(1)})) \frac{\bar{\Omega}_1}{\Omega_1^2}$$

$$= \frac{e_1}{m_1} \frac{\bar{\Omega}_1}{\Omega_1^2} \times (\bar{E}^{(1)} + \frac{1}{c} \bar{u}_1 \times \bar{B}^{(1)}) + \frac{\bar{\Omega}_1 (\bar{\Omega}_1 \cdot \bar{v}_1^{(1)})}{\Omega_1^2} - \frac{\bar{\Omega}_1 \times (\bar{\Omega}_1 \times \bar{v}_1^{(1)})}{\Omega_1^2} .$$

The last two terms on the right hand side are nothing but  $\tilde{\mathbf{v}}_1^{(1)}$ . Hence this last equation may be rewritten as:

$$\begin{aligned} \tilde{\mathbf{v}}_1^{(1)} + i(\omega - \bar{\mathbf{k}} \cdot \bar{\mathbf{u}}_1) \frac{\bar{\Omega}_1 \times \tilde{\mathbf{v}}_1^{(1)}}{\Omega_1^2} &= \frac{\frac{e_1}{m_1}}{-i(\omega - \bar{\mathbf{k}} \cdot \bar{\mathbf{u}}_1)} [\bar{\Omega}_1 \cdot \tilde{\mathbf{E}}^{(1)} + \frac{1}{c} \bar{\Omega}_1 \cdot (\bar{\mathbf{u}}_1 \times \tilde{\mathbf{B}}^{(1)})] \frac{\bar{\Omega}_1}{\Omega_1^2} \\ &\quad - \frac{e_1}{m_1} \frac{\bar{\Omega}_1}{\Omega_1^2} \times (\tilde{\mathbf{E}}^{(1)} + \frac{1}{c} \bar{\mathbf{u}}_1 \times \tilde{\mathbf{B}}^{(1)}) \end{aligned} \quad (28)$$

From Eq. (26):

$$+\bar{\Omega}_1 \times \tilde{\mathbf{v}}_1^{(1)} = +i(\omega - \bar{\mathbf{k}} \cdot \bar{\mathbf{u}}_1) \tilde{\mathbf{v}}_1^{(1)} + \frac{e_1}{m_1} [\tilde{\mathbf{E}}^{(1)} + \frac{1}{c} \bar{\mathbf{u}}_1 \times \tilde{\mathbf{B}}^{(1)}] \quad (29)$$

Substituting Eq. (29) into Eq. (28), and using  $\tilde{\mathbf{B}}^{(1)} = \frac{c}{\omega} \bar{\mathbf{k}} \times \tilde{\mathbf{E}}^{(1)}$  we find:

$$\begin{aligned} \tilde{\mathbf{v}}_1^{(1)} &= \frac{-e_1/m_1}{\Omega_1^2 - (\omega - \bar{\mathbf{k}} \cdot \bar{\mathbf{u}}_1)^2} \{ i(\omega - \bar{\mathbf{k}} \cdot \bar{\mathbf{u}}_1) [\tilde{\mathbf{E}}^{(1)} + \frac{1}{\omega} \bar{\mathbf{u}}_1 \times (\bar{\mathbf{k}} \times \tilde{\mathbf{E}}^{(1)})] \\ &\quad + \bar{\Omega}_1 \times [\tilde{\mathbf{E}}^{(1)} + \frac{1}{\omega} \bar{\mathbf{u}}_1 \times (\bar{\mathbf{k}} \times \tilde{\mathbf{E}}^{(1)})] - \frac{i\bar{\Omega}_1}{(\omega - \bar{\mathbf{k}} \cdot \bar{\mathbf{u}}_1)} \\ &\quad \cdot \bar{\Omega}_1 \cdot [\tilde{\mathbf{E}}^{(1)} + \frac{1}{\omega} \bar{\mathbf{u}}_1 \times (\bar{\mathbf{k}} \times \tilde{\mathbf{E}}^{(1)})] \} \end{aligned} \quad (30)$$

Substitution of Eq. (30) into (24) gives an equation of the form

$$\tilde{\mathbf{R}} \cdot \tilde{\mathbf{E}}^{(1)} = 0, \quad (31)$$

where  $\tilde{\mathbf{R}}$  is a 3 x 3 dyadic involving known quantities.  $\tilde{\mathbf{R}}$  may also be written as a 3 x 3 matrix. It is well known that a necessary condition for such an equation to have a nontrivial solution is that the determinant of the matrix vanish. Letting  $|\mathbf{R}| = 0$  gives an equation for the normal frequencies  $\omega = \omega(\bar{\mathbf{k}})$ .

### 3.2 ION BEAM STREAMING INTO A BACKGROUND ION-ELECTRIC PLASMA IN THE COLD PLASMA APPROXIMATION

Let us fix a coordinate system on the background ion-electron plasma and take

$$\vec{B} = (0, 0, B_0) = B_0 \hat{Z} \quad (32a)$$

$$\vec{k} = (k_x, 0, k_z) = k_x \hat{X} + k_z \hat{Z} \quad (32b)$$

$$\vec{u} = (v, 0, 0) = v \hat{X} \quad (32c)$$

We want to solve the normal mode problem for  $\omega(\vec{k})$ . Specifically, we solve (see Eq. (24) of previous subsection)

$$(\omega^2 - c^2 k^2) \vec{E} + c^2 \vec{k}(\vec{k} \cdot \vec{E}) = -4\pi i \omega \vec{j} \quad (33)$$

where

$$\vec{j} = \sum_1 e_1 N_1 (\vec{v}_1 + \vec{u}_1 \frac{\vec{k} \cdot \vec{v}_1}{(\omega - \vec{k} \cdot \vec{u}_1)}) \quad (34)$$

$$\text{and } \vec{v}_1 \equiv \vec{v}_{1(1)} + \vec{v}_{1(2)} \quad (35a)$$

with

$$\vec{v}_{1(1)} = \frac{-e_1/m_1}{\Omega_1^2 - (\omega - \vec{k} \cdot \vec{u}_1)^2} \{ i(\omega - \vec{k} \cdot \vec{u}_1) \vec{E} + \vec{\Omega}_1 \times \vec{E} - i \frac{\vec{\Omega}_1}{(\omega - \vec{k} \cdot \vec{u}_1)} \vec{\Omega}_1 \cdot \vec{E} \} \quad (35b)$$

$$\vec{v}_{1(2)} = \frac{-e_1/m_1}{\Omega_1^2 - (\omega - \vec{k} \cdot \vec{u}_1)^2} \{ [i(\omega - \vec{k} \cdot \vec{u}_1) + \vec{\Omega}_1 \times - i \frac{\vec{\Omega}_1}{(\omega - \vec{k} \cdot \vec{u}_1)} \vec{\Omega}_1 \cdot ]$$

$$\cdot \frac{\vec{u}_1 \times (\vec{k} \times \vec{E})}{\omega} \} \quad (35c)$$

Since  $\vec{j} = \vec{\sigma} \cdot \vec{E}$ , Eq. (35) may be rewritten as:

$$(\omega^2 - c^2 k^2) \vec{I} \cdot \vec{E} + c^2 \vec{k}(\vec{k} \cdot \vec{E}) + 4\pi i \omega \vec{\sigma} \cdot \vec{E} = 0, \quad (36)$$

which may be expressed as

$$\vec{R} \cdot \vec{E} = 0 \quad (37)$$

$\vec{R}$  is called the dielectric tensor since it gives the dielectric response of the plasma.

In Eqs. (33) through (37)  $\vec{E}$ ,  $\vec{j}$ , and  $\vec{v}$  are the first order in perturbation theory Fourier coefficients of the electric field, current density, and velocity of species  $l$  of the previous section;  $\vec{v}_{(1)}$  represents the electrostatic and  $\vec{v}_{(2)}$  the magnetic contribution to the perturbed velocity. For simplicity of notation we have dropped the tilde and superscript (1) and below we designate a generic plasma species by the subscript  $l$  instead of  $i$  as in the previous subsection. Here subscript  $l$  indicates background ions unless it appears as a summation variable.

To solve Eq. (33) we evaluate Eq. (35), substitute the result into Eq. (34) for each plasma species, sum over species and finally substitute that result into Eq. (33), thereby obtaining an equation of the form  $\vec{R} \cdot \vec{E} = 0$  which is then solved for the normal frequencies under suitable approximations.

For background ions and electrons the streaming velocity is zero ( $u_l = 0$ , where  $l$  denotes either ions or electrons). In this case Eq. (35c) is identically zero. After some algebra, the right hand side of Eq. (33) for each background species is found to be

$$-4\pi i \omega \vec{j}_l = \frac{i \omega_{pl}^2}{\Omega_l^2 - \omega^2} \begin{pmatrix} i \omega E_x - \Omega_l E_y \\ i \omega E_y + \Omega_l E_x \\ i \omega E_z - i \frac{\Omega_l^2}{\omega} E_z \end{pmatrix} \quad (38)$$

In Eq. (38),  $\omega_{pl} \equiv \left( \frac{4\pi N_l e_l^2}{m_l} \right)^{1/2}$  is the plasma frequency,  $\Omega_l = \frac{e_l B_0}{m_l c}$  is the cyclotron frequency and we have introduced Cartesian coordinates. A similar calculation for the streaming ions, neglecting the magnetic terms (we perform simulations using an electrostatic code) gives:

$$\begin{aligned}
-4\pi i \omega \bar{J}_b(1) &= \frac{i \omega_{pb}^2}{\Omega_b^2 - (\omega - k_x V)^2} \begin{pmatrix} i(\omega - k_x V) E_x - \Omega_b E_y \\ i(\omega - k_x V) E_y + \Omega_b E_x \\ i(\omega - k_x V) E_z - i \frac{\Omega_b^2 E_z}{(\omega - k_x V)} \end{pmatrix} \\
&+ \frac{i \omega_{pb}^2}{[\Omega_b^2 - (\omega - k_x V)^2](\omega - k_x V)} \left[ i(\omega - k_x V)(k_x V E_x + k_z V E_z) - \Omega_b k_x V E_y - \frac{i \Omega_b^2 k_z V E_z}{\omega - k_x V} \right] \begin{pmatrix} 1 \\ 0 \\ 0 \end{pmatrix} \quad (39)
\end{aligned}$$

Here the subscript b refers to beam ions. Subscripts, i, e, whenever they appear, designate background ions and electrons, respectively. The magnetic and the full electromagnetic contribution to the current density have also been evaluated. The results will not be written down since we shall subsequently be interested in the electrostatic approximation. Dropping the magnetic terms in the current density amounts to taking  $kV/\omega \ll 1$  as a comparison of the electrostatic and magnetic terms shows. Making use of Eqs. (33), (34), (38), and (39), the matrix elements of the dielectric tensor, as defined by Eq. (37), may be written down explicitly:

$$R_{xx} = \omega^2 - c^2 k_z^2 + \frac{\omega_{pe}^2 \omega^2}{\Omega_e^2 - \omega^2} + \frac{\omega_{pi}^2 \omega^2}{\Omega_i^2 - \omega^2} + \frac{\omega_{pb}^2 \omega^2}{\Omega_b^2 - (\omega - k_x V)^2}$$

$$R_{xy} = \frac{i \omega_{pe}^2 \Omega_e \omega}{\Omega_e^2 - \omega^2} + \frac{i \omega_{pi}^2 \Omega_i \omega}{\Omega_i^2 - \omega^2} + \frac{i \omega_{pb}^2 \Omega_b \omega^2}{[\Omega_b^2 - (\omega - k_x V)^2](\omega - k_x V)}$$

$$R_{xz} = c^2 k_x k_z - \frac{\omega_{pb}^2 k_z V \omega}{(\omega - k_x V)^2}$$

$$R_{yx} = \frac{-i \omega_{pe}^2 \Omega_e \omega}{\Omega_e^2 - \omega^2} - \frac{i \omega_{pi}^2 \Omega_i \omega}{\Omega_i^2 - \omega^2} - \frac{i \omega_{pb}^2 \Omega_b \omega}{\Omega_b^2 - (\omega - k_x V)^2}$$

$$R_{yy} = \omega^2 - c^2 k^2 + \frac{\omega_{pe}^2 \omega^2}{\Omega_e^2 - \omega^2} + \frac{\omega_{pi}^2 \omega^2}{\Omega_i^2 - \omega^2} + \frac{\omega_{pb}^2 (\omega - k_x V) \omega}{\Omega_b^2 - (\omega - k_x V)^2}$$

$$R_{yz} = R_{zy} = 0$$

$$R_{zx} = c^2 k_x k_z$$

$$R_{zz} = \omega^2 - c^2 k_x^2 - \omega_{pe}^2 - \omega_{pi}^2 - \frac{\omega_{pb}^2 \omega}{(\omega - k_x V)} \quad (40)$$

We next wish to solve for the normal frequencies. To obtain tractable expressions, we look for normal frequencies  $\omega$  such that

$$\Omega_{i,b} \ll \omega \ll \Omega_e \quad (41)$$

Making use of Eq. (41), the dielectric tensor becomes:

$$R_{xx} = \omega^2 - c^2 k_z^2 + \frac{\omega_{pe}^2 \omega^2}{\Omega_e^2} - \omega_{pi}^2 - \frac{\omega_{pb}^2 \omega^2}{(\omega - k_x V)^2}$$

$$R_{xy} = \frac{i \omega_{pe}^2 \omega}{\Omega_e} - \frac{i \omega_{pi}^2 \Omega_i}{\omega} - \frac{i \omega_{pb}^2 \Omega_b \omega^2}{(\omega - k_x V)^3}$$

$$R_{xz} = c^2 k_x k_z - \frac{\omega_{pb}^2 (k_z V) \omega}{(\omega - k_x V)^2}$$

$$R_{yx} = \frac{-i \omega_{pe}^2 \omega}{\Omega_e} + \frac{i \omega_{pi}^2 \Omega_i}{\omega} + \frac{i \omega_{pb}^2 \Omega_b \omega}{(\omega - k_x V)^2}$$

$$R_{yy} = \omega^2 - c^2 k^2 + \frac{\omega_{pe}^2 \omega^2}{\Omega_e^2} - \omega_{pi}^2 - \frac{\omega_{pb}^2 \omega}{(\omega - k_x V)}$$

$$R_{yz} = 0$$

$$R_{zx} = c^2 k_x k_z \quad R_{zy} = 0$$

$$R_{zz} = \omega^2 - c^2 k_x^2 - \omega_{pe}^2 - \omega_{pi}^2 - \frac{\omega_{pb}^2}{\omega - k_x V} \quad . \quad (42)$$

For the normal frequencies we demand  $\det \tilde{R} = 0$ , i.e.,

$$|R| = R_{xx}R_{yy}R_{zz} - R_{xy}R_{yx}R_{zz} - R_{xz}R_{zx}R_{yy} = 0 \quad . \quad (43)$$

To obtain a reasonably simple dispersion relation we further restrict ourselves to frequencies  $\omega$  such that  $\omega/kc \ll 1$  (which is also a consequence of the electrostatic approximation). We are interested in beam ions nearly perpendicular to the magnetic field as this produces the most electron heating and so we take  $k_z/k_x \ll 1$ . Carrying out the algebra in Eq. (43), dividing by  $c^4 k_x^2 k^2$  and keeping the largest contributions only, we arrive at

$$0 = 1 + \frac{\omega_{pe}^2}{\Omega_e^2} - \frac{\omega_{pi}^2}{\omega^2} - \frac{\omega_{pb}^2}{(\omega - k_x V)^2} + \left(\frac{k_z}{k_x}\right)^2 \left[ 1 - \frac{\omega_{pe}^2}{\omega^2} - \frac{\omega_{pi}^2}{\omega^2} - \frac{\omega_{pb}^2}{\omega(\omega - k_x V)} \right] - \frac{k_z}{k_x} \frac{\omega_{pb}^2 (k_z V)}{\omega(\omega - k_x V)^2} \quad . \quad (44)$$

Noting that  $k_z/k_x \ll 1$  and that  $\omega_{pe}^2 \gg \omega_{pb}^2$ , Eq. (36) may be given approximately by:

$$1 + \frac{\omega_{pe}^2}{\Omega_e^2} - \frac{\omega_{pi}^2}{\omega^2} - \frac{\omega_{pb}^2}{(\omega - k_x V)^2} - \left(\frac{k_z}{k_x}\right)^2 \frac{\omega_{pe}^2}{\omega^2} = 0 \quad . \quad (45)$$

This result is to be compared to the result of McBride and coworkers (1972).

$$1 + \frac{\omega_{pe}^2}{\Omega_e^2} - \frac{\omega_{pb}^2}{(\omega - k_x V)^2} - \left(\frac{k_z}{k}\right)^2 \frac{\omega_{pe}^2}{\omega^2} = 0 \quad . \quad (46)$$



The difference between Eqs. (45) and (46) is  $(k_z/k_x)^2$  versus  $(k_z/k)^2$ , which is negligible because  $k^2 \approx k_x^2$ . Whereas the McBride result is obtained as the cold limit of a warm theory, the derivation here has as starting point a cold plasma. Note also that in McBride's work there are no background ions.

Let us assume equal masses and charges for streaming and background ions, and equal charges for electrons and ions. Furthermore, let us define the lower hybrid frequency by

$$\omega_{lh}^2 \equiv \frac{\omega_{pi}^2}{1 + \frac{\omega_{pe}^2}{\Omega_e^2}} \quad (47)$$

Upon dividing Eq. (45) through by  $1 + \omega_{pe}^2/\Omega_e^2$ , using Eq. (47) and noting that  $\omega_{pe}^2 = (m_i/m_e)(N_e/N_i)\omega_{pi}^2$  and  $\omega_{pb}^2 = (N_b/N_i)\omega_{pi}^2$ , Eq. (45) may be rewritten as

$$\omega_{lh}^2(1 + \delta^2) \frac{1}{\omega^2} + \epsilon_r \frac{\omega_{lh}^2}{(\omega - k_x V)^2} = 1 \quad (48a)$$

$$\text{where} \quad \delta^2 = (k_z/k_x)^2(m_i/m_e)(N_e/N_i) \quad (48b)$$

$$\epsilon_r = N_b/N_i \quad (48c)$$

This result is to be compared to Abe and Machida (1985). The difference is that there

$$\omega_{lh}^2 = \frac{\omega_{pi}^2}{1 + \left(\frac{\omega_{pe}}{\Omega_e}\right)^2 \left(\frac{k_x}{k}\right)^2} \quad (49)$$

For  $k_z \ll k_x$ , Eqs. (47) and (49) are essentially identical.

The dispersion relation (Eq. (48)) is easily written as a quartic polynomial in  $\omega(k)$  and solved numerically. A plot of  $\omega$  versus  $k_x V$  appears in Fig. 7. Our

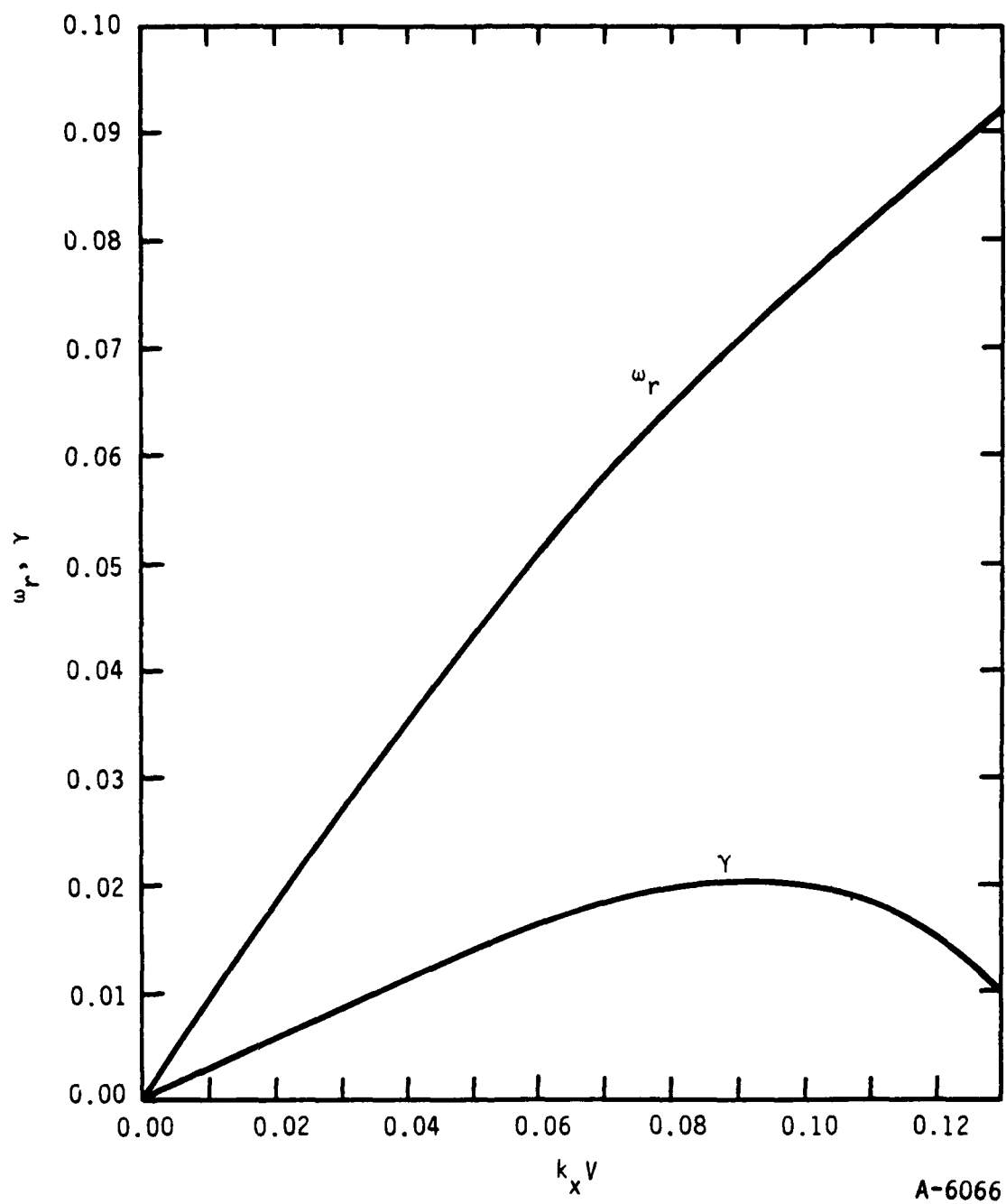


Figure 7. Plot of the real ( $\omega_r$ ) and imaginary ( $\gamma$ ) parts of  $\omega$  versus  $k_x V$ .

choice of parameter normalizations are such that the velocity of the beam, the mass, cyclotron frequency, and the charge of the electron are all unity. In addition the number density of electrons and ions is taken to be the same. The figure shows the real ( $\omega_r$ ) and imaginary ( $\gamma$ ) parts of  $\omega(k)$  as a function of  $k_x V$ .

Physically,  $\gamma$  gives the unstable growth rate of electrostatic waves. We are interested in domains of  $k$  space where  $\gamma$  is non-zero for the following reason. In order that the electrons be heated as required by the CIV hypothesis, the plasma must be able to transfer energy from the beam to the background electrons. This is achieved via a plasma instability which pumps energy from the beam to the electrostatic field which is then imparted to the electrons. In Fig. 7 the maximum growth rate is  $\gamma = 0.02$  and is achieved at  $k_x V \approx 0.095$ . From the well known relation from finite Fourier transforms  $k = (2\pi/L)n$ , with  $n$  an integer, we can readily calculate the period of the physical length of the system which leads to instability.

### 3.3 COMPUTER SIMULATION OF ION BEAM STREAMING INTO A BACKGROUND ION-ELECTRON PLASMA

During the year we modified the ESI plasma simulation code. This code was developed by Birdsall and coworkers (Birdsall and Langdon, 1985) for particle-in-cell simulations of plasma effects. The code is one-dimensional in position space and was originally two-dimensional in velocity space with the magnetic field directed perpendicularly to the plane of the velocity vectors. We have modified ESI to be three-dimensional in velocity space, so that we now consider four of the six dimensions of phase space for each particle. We now allow the magnetic field to be at any angle with the ion beam velocity vector; we take the ion beam velocity vector to be along the  $x$  axis, where  $x$  is the one position variable in the code. With the modification we can now simulate the conditions that we developed the linear theory for in Subsection 3.2 above. We ignore collisions with neutral molecules for the results in this section. Such collisions are considered in Subsection 3.5.

The case of the fast ion beam streaming into a plasma represents a version of the CIV experiments where a fast neutral beam is injected into the ambient plasma of the ionosphere about the space shuttle. This is because the ionization of the fast neutrals produces a beam of fast ions, as there is little momentum change of the neutral molecule when it is ionized. For the simulation we take the electron plasma frequency  $\omega_p$  of the ambient plasma to be equal to the electron cyclotron frequency,  $\Omega_e$ . For example, if the magnetic field B is 0.33 Gauss then the ambient electron density  $n_e$  is  $1.06 \times 10^4 \text{ cm}^3$ , or  $n_e$  is  $1.98 \times 10^4 \text{ cm}^3$  for a B of 0.45 Gauss, as

$$\omega_p/\Omega_e = 3.21 \times 10^{-3} n_e^{1/2}/B$$

when B is in Gauss and  $n_e$  is in number/cm<sup>3</sup>.

McBride and coworkers (1972) show that the maximum growth rate  $\gamma$  occurs when the angle  $\psi$  between the beam velocity vector and the magnetic field is

$$\psi_{\max} = 90^\circ - \sin^{-1}(m_e/m_i)^{1/2} ,$$

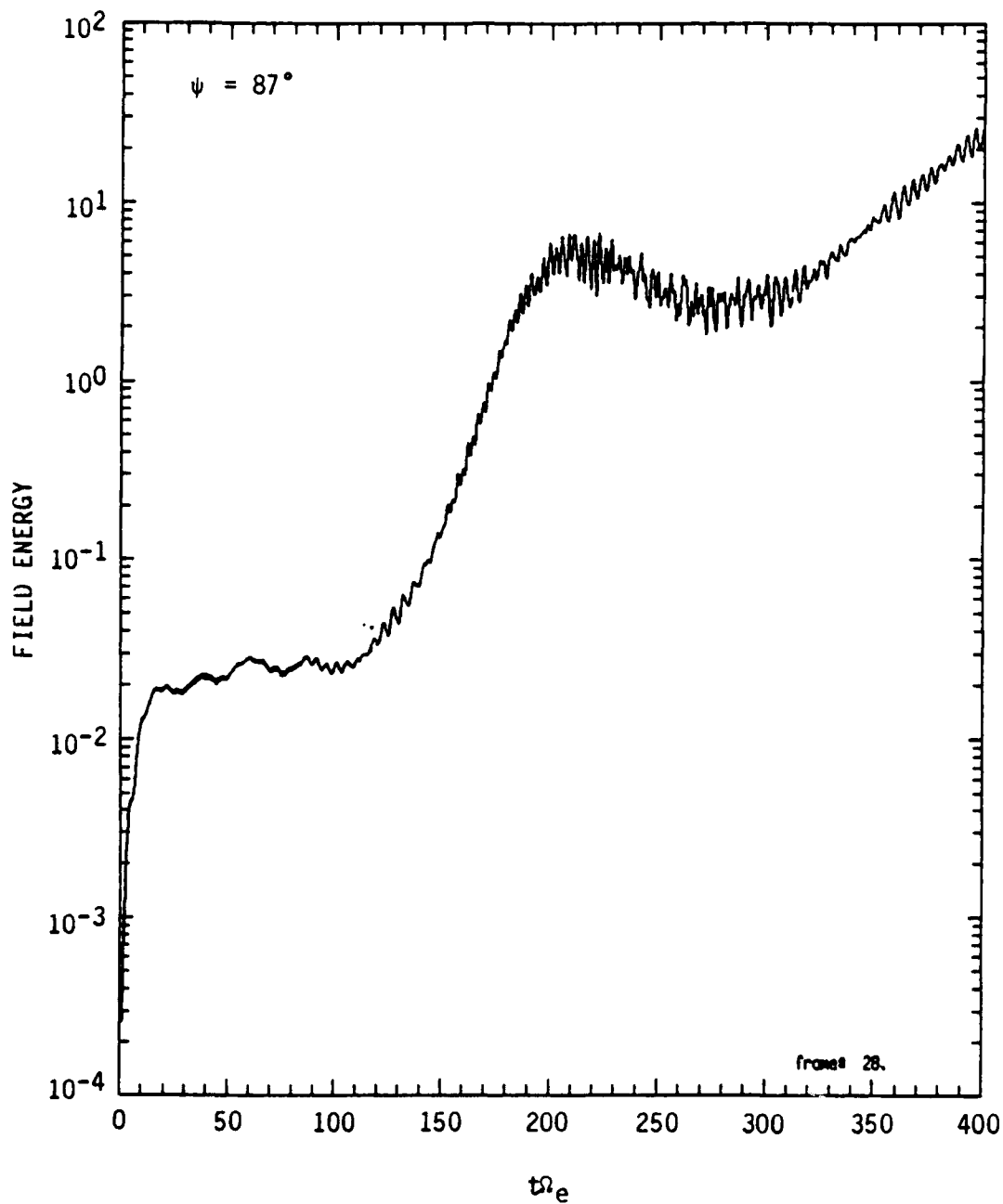
where  $m_e$  and  $m_i$  use the masses of the electron and the ion, respectively. We now present the results of simulations for two values of  $\psi$ . We use an artificially high  $m_e/m_i$  ratio of 0.01, which speeds the computation while still preserving the essential physics that ions are much more massive than electrons. Also, we take the ions to be unmagnetized (i.e., they have an infinite gyroradius), which correctly represents the other important physical difference between the ions and electrons. The maximum growth then occurs at  $\psi_{\max} = 84.3^\circ$ . We discuss results for  $\psi$  values of 3 and 87 deg - one value slightly greater than  $\psi_{\max}$  and one value that is nearly perpendicular to  $\psi_{\max}$ . In both simulations  $\omega_p = \Omega_e$ , the velocity of the fast ion beam is 100 times the mean thermal velocity of the ambient ions (which is equal to the mean thermal velocity of the electrons so that the electron temperature is less than the ion temperature,  $T_e \approx 0.01 T_i$ ), and the number density of the fast ion beam is 10 percent of that of the ambient ions.

Figure 8 shows the growth of the electric field energy for the two angles. This shows that the field energy builds up to a value that is several times larger for  $\psi = 87^\circ$  than it does for  $\psi = 3^\circ$ . We can compare the logarithmic growth rate with that predicted by  $\gamma$  in Fig. 7 for  $\psi = 87^\circ$ . The predicted value from linear theory has  $\gamma = 0.02 \Omega_e$  while the slope of Fig. 8a (which is related to  $\gamma$  by the factor of  $2.303/2$ ) gives  $\gamma = 0.018 \Omega_e$  for times from 110 to  $140/\Omega_e$ . At later times from 140 to  $180/\Omega_e$  the slope is larger as non-linear effects dominate; here  $\gamma = 0.038 \Omega_e$  for  $\psi = 3^\circ$ ,  $\gamma = 0.012 \Omega_e$  for times from 115 to  $140/\Omega_e$  and  $\gamma = 0.034 \Omega_e$  for times from 150 to  $180/\Omega_e$ . Thus the field energy builds up even for  $\psi$  far away from  $\psi_{\max}$ .

When the field energy increases the ion beam develops wavelike structures as a result of the electrostatic field. The field then begins to trap particles, and the growth saturates. Figure 9 shows the velocity along the direction of the fast ion beam for  $\psi = 3^\circ$ . The velocity of each particle is plotted as a point, so the coherent effects are evident. The wave structure at  $v_x \approx 1$  is in the fast ion beam, while the ambient ions have nearly zero velocity. The electrons also have a wavelike structure in their velocities.

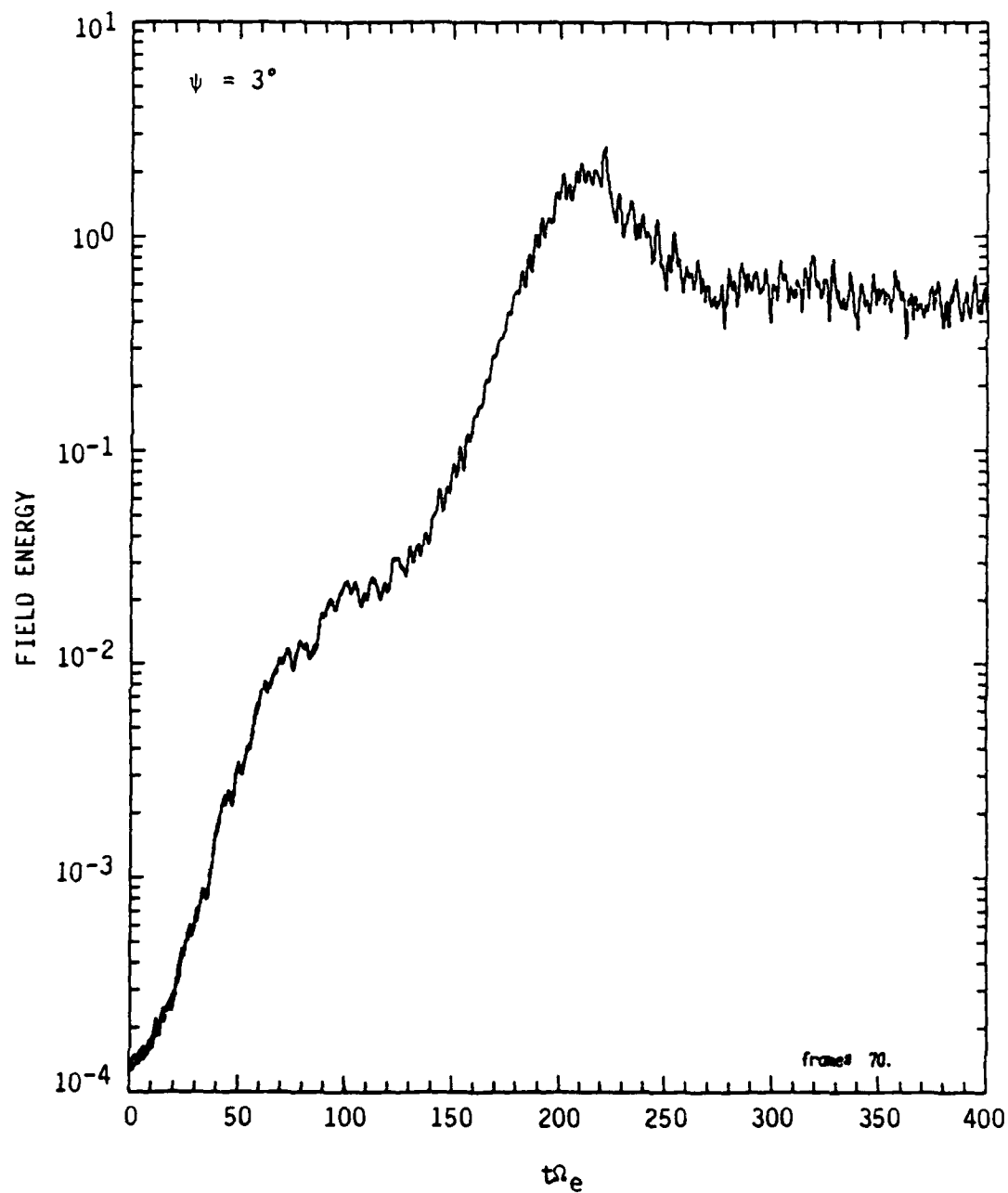
Figure 10 shows a comparison of the electron kinetic energies for the two angles. Here the perpendicular motion gives over twice as much energy to the electrons, but it is interesting that the nearly parallel motion can still heat the electrons as much as it does. The increase for times greater than  $350/\Omega_e$  is caused by a plasma effect that transfers energy back and forth between the beam ions and the electrons. Additional calculations show that the kinetic energy of the electrons has a maximum of approximately 102 at a time of  $450/\Omega_e$  and it then declines to a value of 68 at a time of  $530/\Omega_e$  (the energy units are normalized so that the initial energy in the ion beam is approximately 349).

The increase in kinetic energy of the electrons occurs at the same time as the drift energy of the fast ions decreases, which is shown in Fig. 11. Note that the initial drift energy is the same for both angles. Only a



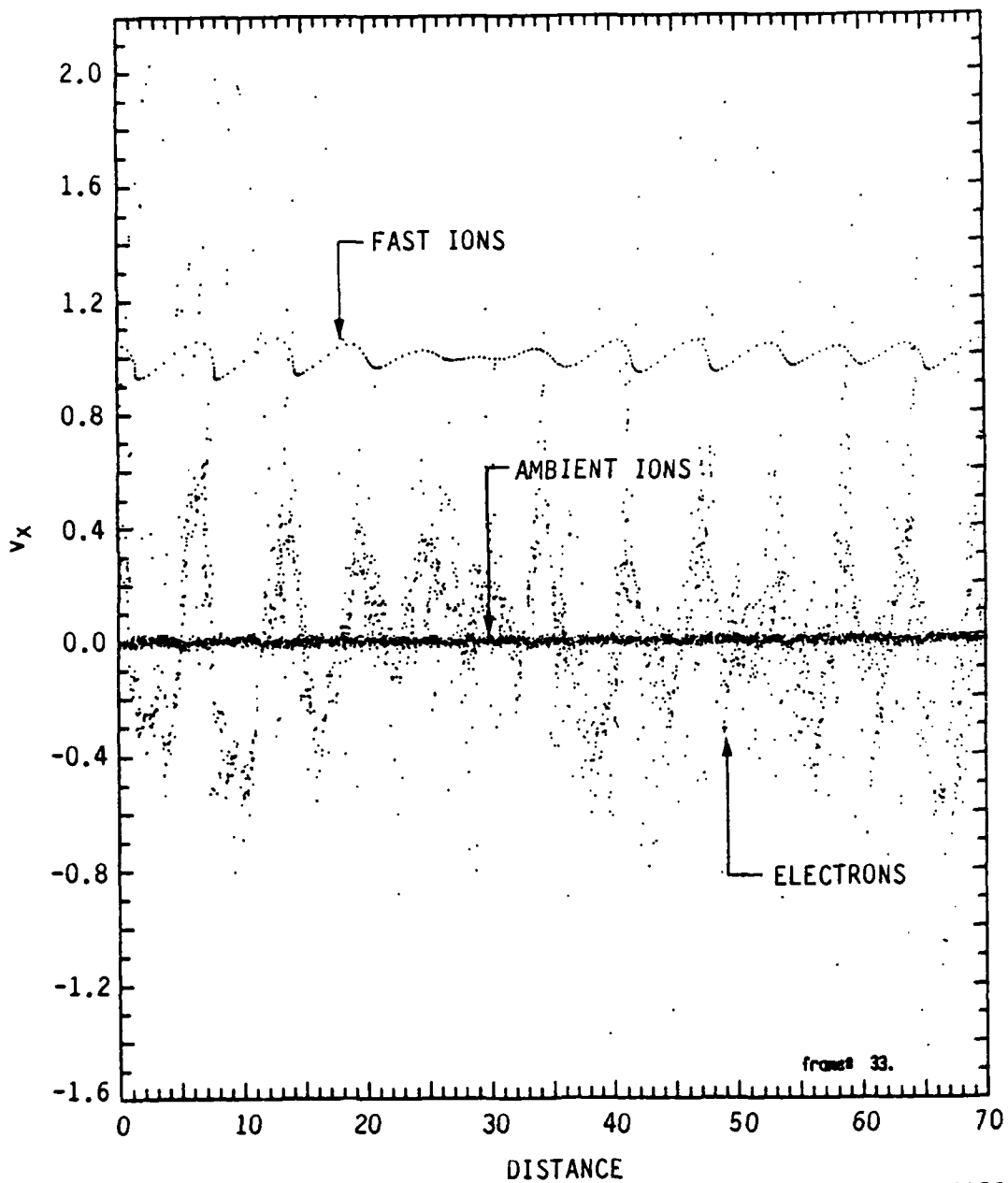
A-6148

Figure 8a. Growth of the electric field energy at two angles  $\psi$  between the magnetic field and the beam velocity. Time is measured in units of the reciprocal of the electron cyclotron frequency  $\Omega_e$ , and the energy units are such that the initial drift energy of the fast ion beam has a value of 349. Figure 8a is for  $\psi = 87^\circ$



A-6149

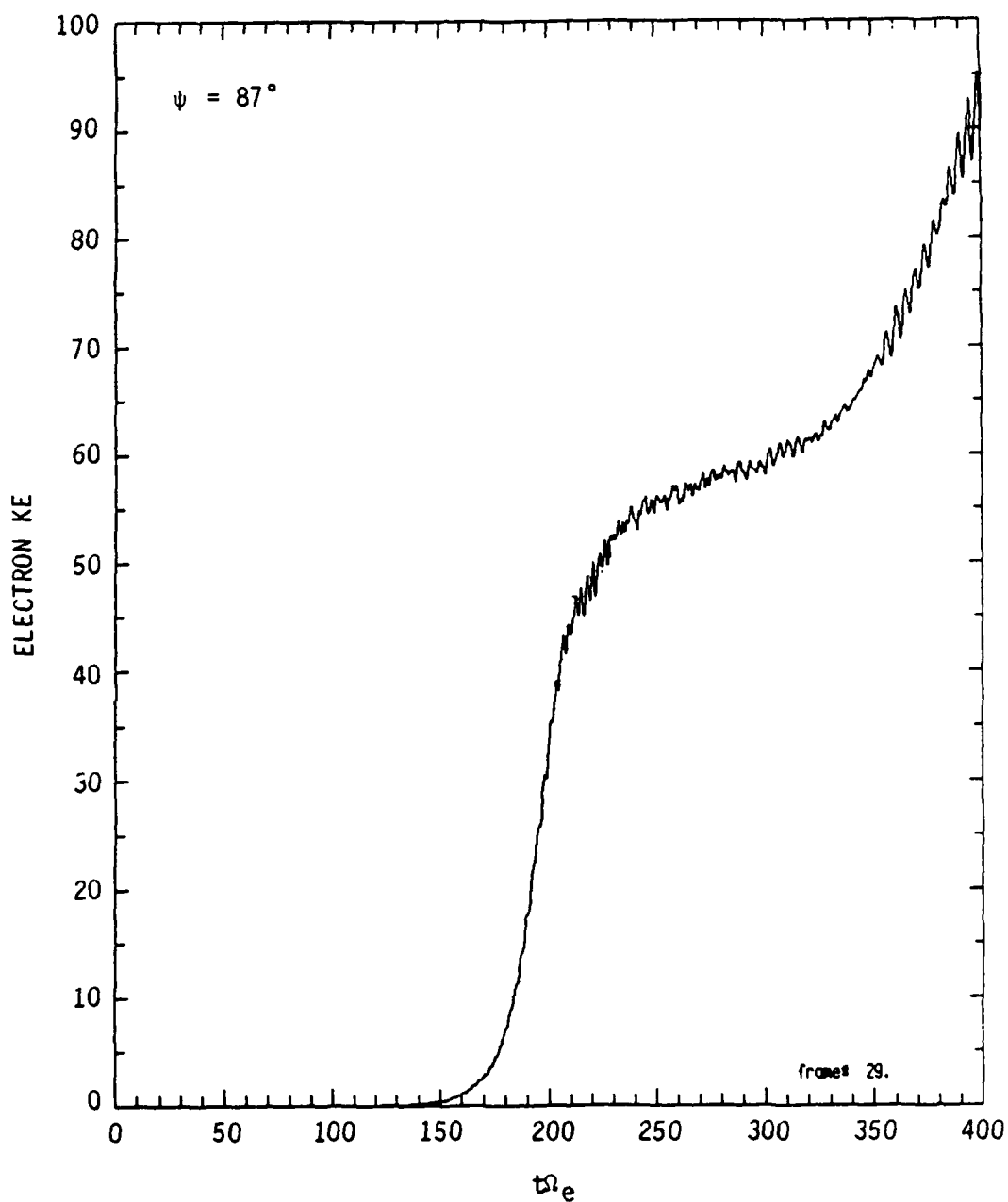
Figure 8b. Growth of the electric field energy at two angles  $\psi$  between the magnetic field and the beam velocity. Time is measured in units of the reciprocal of the electron cyclotron frequency  $\Omega_e$ , and the energy units are such that the initial drift energy of the fast ion beam has a value of 349. Figure 8b is for  $3^\circ$



A-6150

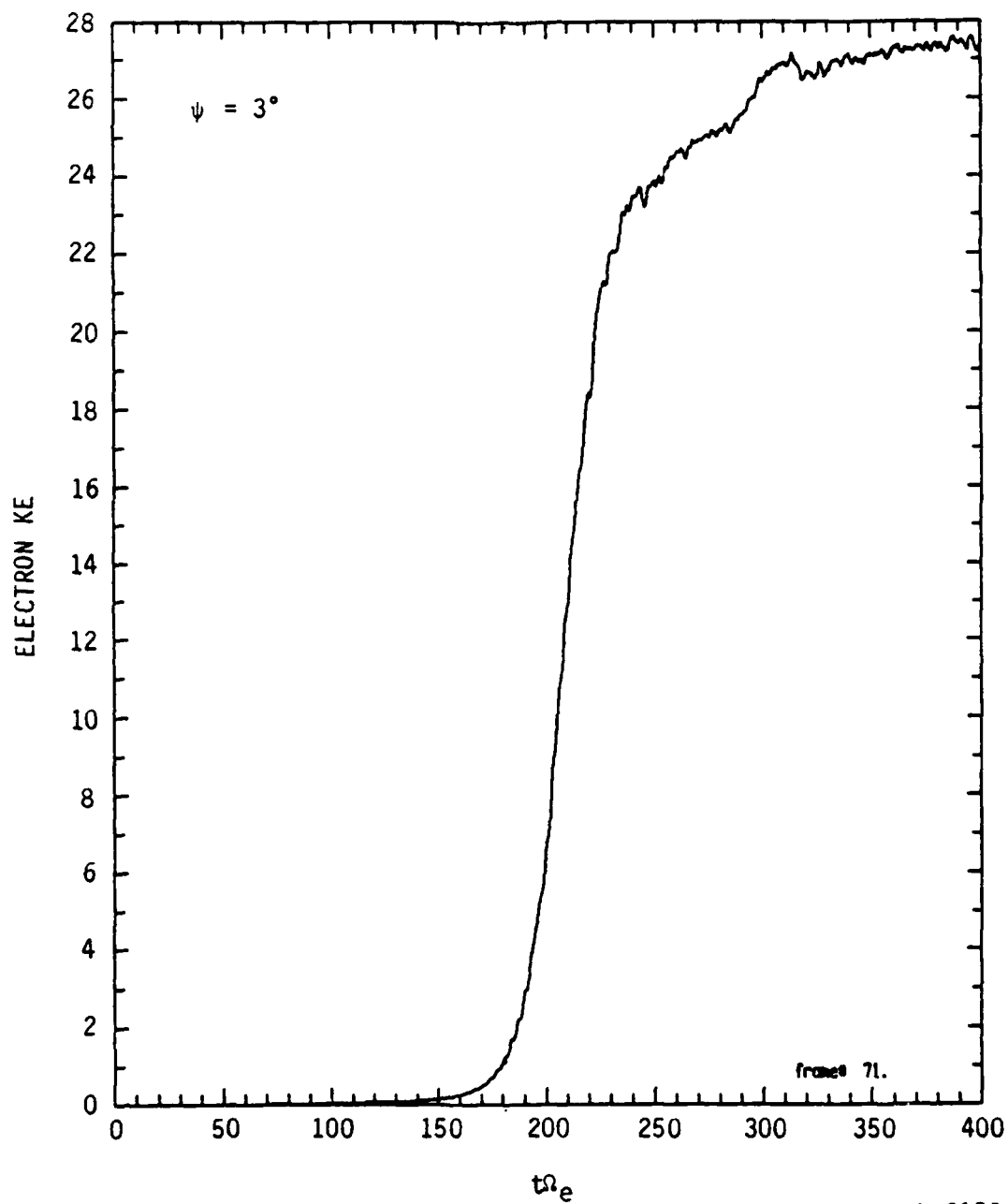
Figure 9. Velocity along the direction of the fast ion beam as a function of distance at a time of  $199.975/\Omega_e$ . The fast ions initially all had  $v_x = 1.0$ ; now their values have a coherent structure. The electrons initially had a distribution of velocity with a mean value of 0.01 - similar to that of the ambient ions





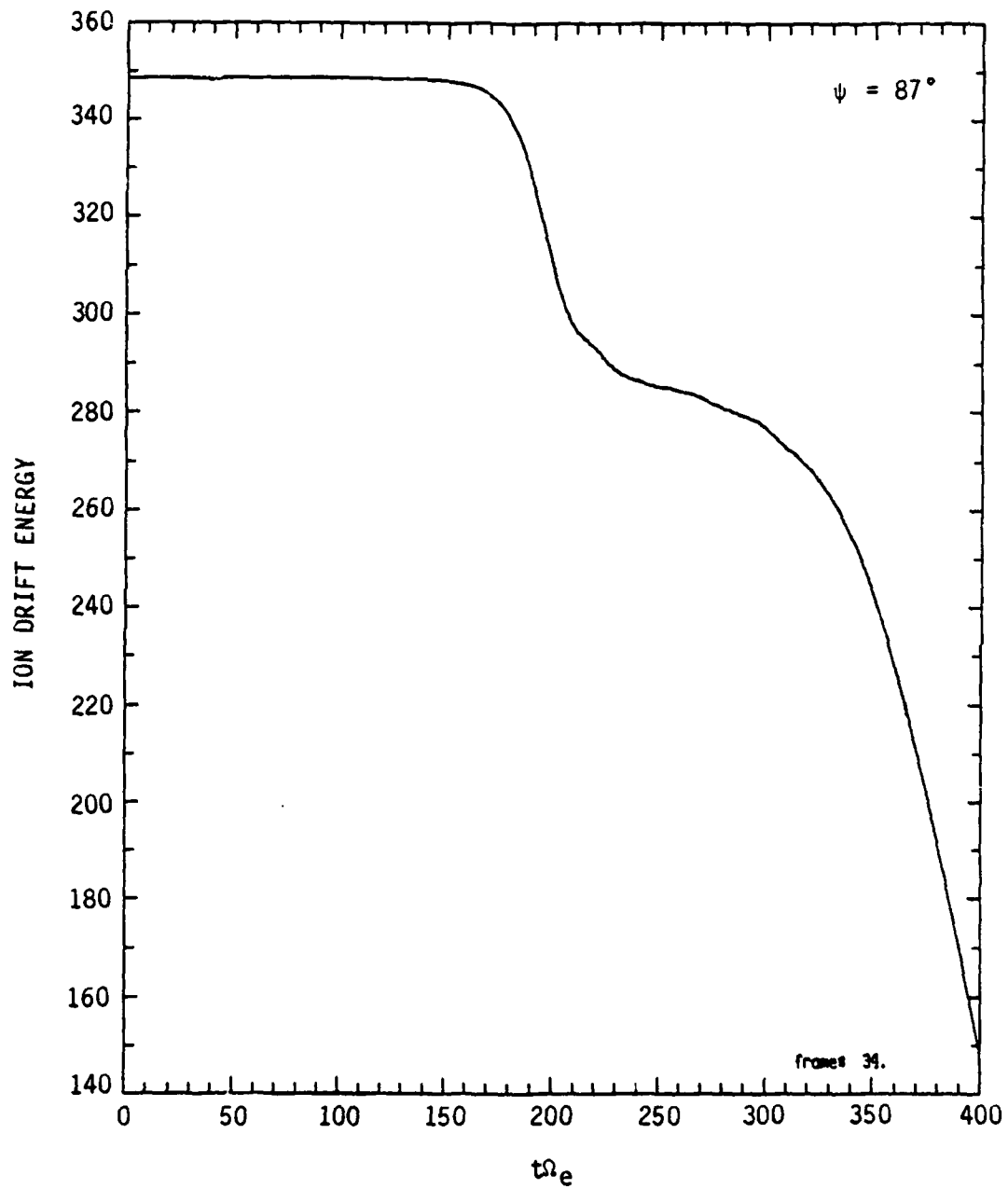
A-6151

Figure 10a. Electron kinetic energy at two angles  $\psi$  between  $\bar{B}$  and  $\bar{v}_x$ . The time units are  $1/\Omega_e$ ; energy can be normalized to the initial drift energy of the ion beam by dividing by 349. Figure 10a shows  $\psi = 87^\circ$



A-6152

Figure 10b. Electron kinetic energy at two angles  $\psi$  between  $\bar{B}$  and  $\bar{v}_x$ . The time units are  $1/\Omega_e$ ; energy can be normalized to the initial drift energy of the ion beam by dividing by 349. Figure 10b is for  $\psi = 3^\circ$



A-6153

Figure 11a. Ion drift energy for two angles  $\psi$  between  $\bar{B}$  and  $\bar{v}_x$ . The time  $t$  is measured in units of the reciprocal electron cyclotron frequency  $\Omega_e$ . Figure 11a is for  $\psi = 87^\circ$

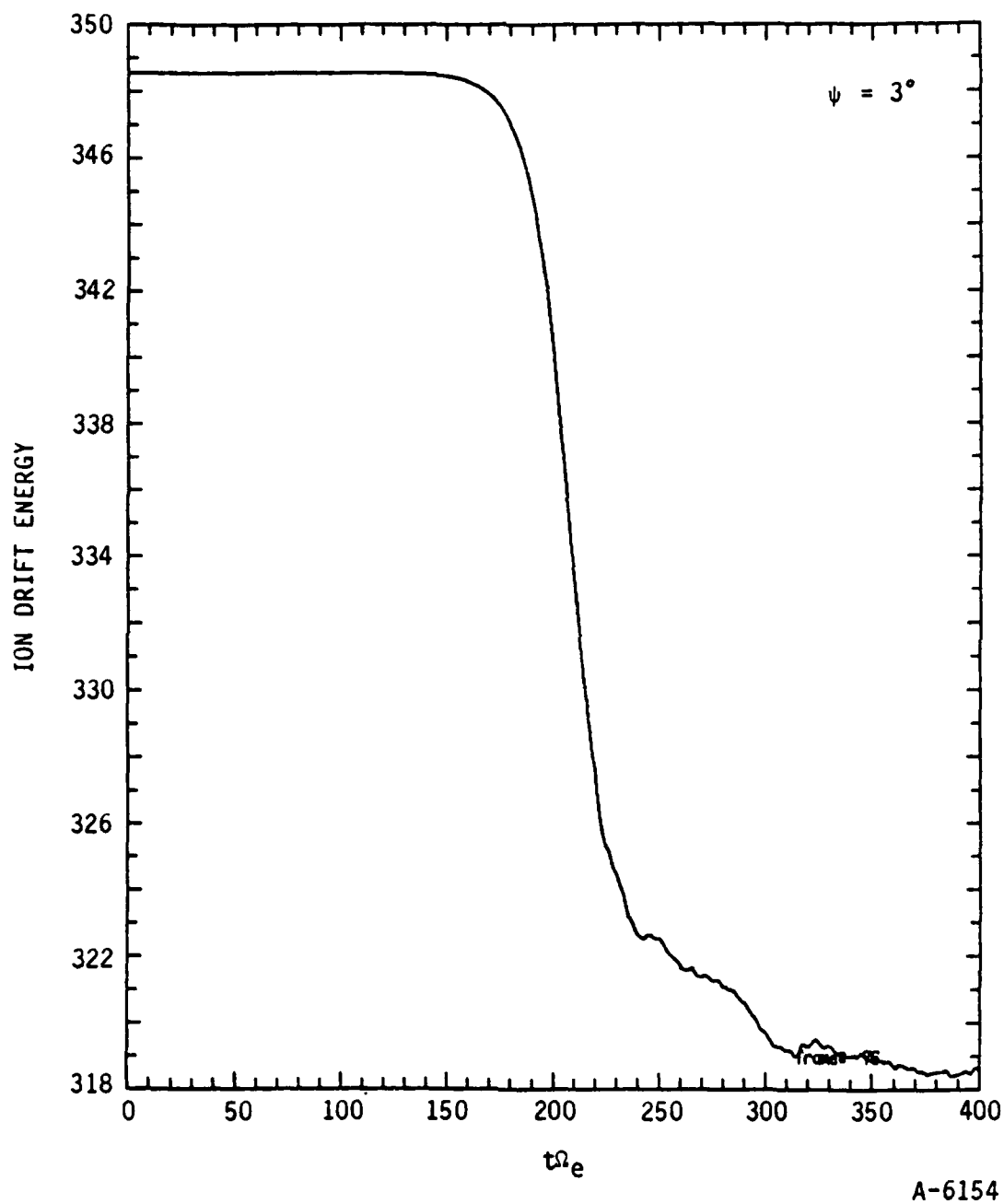


Figure 11b. Ion drift energy for two angles  $\psi$  between  $\bar{B}$  and  $\bar{v}_x$ . The time  $t$  is measured in units of the reciprocal electron cyclotron frequency  $\Omega_e$ . Figure 11b is for  $\psi = 3^\circ$ .

fraction of this energy is removed from the beam. This fraction is smaller for  $\psi = 3^\circ$ . Additional calculations show that the drift energy decreases to 112 and then increases to 215 and decreases to 130 (where 349 is the initial beam energy) at times between 400 and  $800/\Omega_e$ . In these simulations, the total energy is conserved to about 0.1 percent.

These results illustrate some of the detail available from the simulations. Note that there is electron heating over a wide range of  $\psi$  angles. However, the electron energy gain is smaller for  $\psi = 3^\circ$  than for  $\psi = 87^\circ$ . Note also that there is a delay of some  $170/\Omega_e$  before the electrons heat appreciably. Then the electrons are quickly heated in a time of about  $50/\Omega_e$ .

### 3.4 WAVES IN A "HOT" PLASMA IN A MAGNETIC FIELD

Following the philosophy for waves in a cold plasma, we study the properties of small amplitude disturbances propagated through a "hot" plasma in a uniform magnetic field. A uniform unbounded plasma is assumed. Our approach is to solve perturbatively the relativistic Vlasov kinetic (collisionless) equation assuming probability conservation and the relativistic Maxwell's equations. We begin with a brief review of the general problem in order to establish the notation and the geometry and then specialize to the system of interest for the CIV experiment.

#### 3.4.1 General Theory

The relativistic equation of motion for a particle of charge  $e$  and rest mass  $m_0$  is

$$\frac{d\vec{p}}{dt} = e(\vec{E} + \frac{1}{c} \vec{v} \times \vec{B}) \equiv \vec{G} \quad (50a)$$

$$\text{where } \vec{p} = \gamma m_0 \vec{v} ; \quad \gamma = \left[ 1 - (v/c)^2 \right]^{-1/2} . \quad (50b)$$

If we let the probable number of particles of a given species in the phase space volume element  $d\bar{x} d\bar{p}$  at  $t$  be given by

$$dN = n_0 f(\bar{x}, \bar{p}, t) d\bar{x} d\bar{p} \quad (52)$$

then the distribution function  $f$  satisfies a relativistic generalization of the collisionless Vlasov equation, namely

$$\frac{\partial f}{\partial t} + \bar{v} \cdot \frac{\partial f}{\partial \bar{x}} + \bar{G} \cdot \frac{\partial f}{\partial \bar{p}} = 0 \quad (53)$$

The forces are to be determined from Maxwell's equations

$$\begin{cases} \bar{v} \times \bar{E} = -\frac{1}{c} \frac{\partial \bar{B}}{\partial t} & \bar{v} \cdot \bar{E} = 4\pi \Sigma n_0 \int f d\bar{p} \\ \bar{v} \times \bar{B} = \frac{1}{c} \frac{\partial \bar{E}}{\partial t} + \frac{4\pi}{c} \Sigma en_0 \int f \bar{v} d\bar{p} & \bar{v} \cdot \bar{B} = 0 \end{cases} \quad (54)$$

Note that  $f$  is normalized so that the probable number density is

$$n(\bar{x}, t) = n_0 \int f d\bar{p} \quad (55)$$

The divergence equations can be thought of as initial conditions valid for all time if they are imposed at  $t=0$ .

In order to solve the complex coupled system of differential Eqs. (53) and (54) we attempt a perturbative solution about a homogeneous plasma with a uniform magnetic field  $\bar{B}_0$ , no electric fields present, the zero order distributions have no angular dependence, and the total current carried by the distributions must vanish in the zero order system. Letting

$$\begin{aligned}
f &= f^0 + f^{(1)} \\
\bar{E} &= \bar{E}^{(1)} \\
\bar{B} &= \bar{B}_0 + \bar{B}^{(1)}
\end{aligned} \tag{56}$$

and substituting  $f$ ,  $\bar{E}$ ,  $\bar{B}$  into the system (53) and (54), we obtain a system of linear equations which can be solved using Fourier-Laplace transforms, defined by:

$$(\bar{E}, \bar{B}, J, f) = \int_0^{\infty} dt e^{-st} \int_{-\infty}^{+\infty} \frac{d\bar{x}}{(2\pi)^3} e^{-i\bar{k} \cdot \bar{x}} (\bar{E}^{(1)}, \bar{B}^{(1)}, J^{(1)}, f^{(1)}) \tag{57}$$

with  $R_e(s) > 0$ , and the inversion formula

$$(\bar{E}^{(1)}, \bar{B}^{(1)}, J^{(1)}, f^{(1)}) = \int_{-\infty}^{+\infty} d\bar{k} e^{i\bar{k} \cdot \bar{x}} \int_{\sigma-i\infty}^{\sigma+i\infty} \frac{ds}{2\pi i} e^{st} (\bar{E}, \bar{B}, J, f) \tag{58}$$

From here on we deal only with transforms, so there should be no confusion between the total fields in Eq. (56) and the quantities on the left of Eq. (57). Also, unlabeled sums mean summation over charged species. The motivation of solution is the same as the cold case, that is eliminate all variables except one (the electric field is a good choice), write the resulting equations as an eigenvalue problem and solve for the eigenvalues and eigenvectors. The result of that analysis is

$$\begin{aligned}
(s^2 + c^2 k^2) \bar{E} - c^2 (\bar{k} \cdot \bar{E}) \bar{k} + 4\pi s \sum \frac{n_o e^2}{m_o \Omega_o} \int_{-\infty}^{+\infty} d\bar{p} \bar{p} \int_{+\infty}^{\phi} d\phi' G(\phi', \phi) \\
\cdot \left[ \bar{E} - \frac{1}{s} \bar{v}' \times (\bar{k} \times \bar{E}) \right] \cdot \frac{\partial f_o}{\partial \bar{p}'} = \bar{I} , \tag{59a}
\end{aligned}$$

where

$$\bar{\mathbf{I}} = s\bar{\mathbf{e}} + ic \bar{\mathbf{k}} \times \bar{\mathbf{b}} + 4\pi s \sum \frac{en_o}{m_o \Omega_o} \int d\bar{\mathbf{p}} \bar{\mathbf{p}} \int_{+\infty}^{\phi} d\phi' G(\phi', \phi) \cdot \left[ g - \frac{e}{sc} \bar{\mathbf{v}}' \times \bar{\mathbf{b}} \cdot \frac{\partial f_o}{\partial \bar{\mathbf{p}}'} \right] . \quad (59b)$$

In Eqs. (59a) and (59b)

$$G(\phi, \phi') = e^{-\left\{ \left( \frac{s + ik_{||} v_{||}}{\Omega} \right) (\phi - \phi') - \frac{k_{\perp} v_{\perp}}{\Omega} (\sin \phi' - \sin \phi) \right\}} \quad (60a)$$

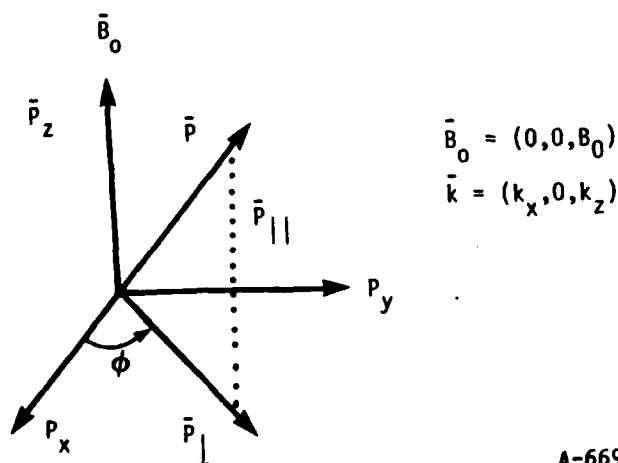
with properties

$$\begin{cases} G(\phi \rightarrow \phi' \rightarrow -\infty) \rightarrow 0 \\ G(\phi \rightarrow \phi', \phi) \rightarrow 1 \end{cases} \quad \text{All finite } \phi \quad (60b)$$

$$\Omega \equiv \frac{e|\bar{\mathbf{B}}_o|}{m_o \gamma c} \equiv \frac{\Omega_o}{\gamma} \quad \text{is the relativistic cyclotron frequency,}$$

and

$$(\bar{\mathbf{e}}, \bar{\mathbf{b}}, \bar{\mathbf{g}}) \equiv \int_{-\infty}^{+\infty} \frac{d\bar{\mathbf{x}}}{(2\pi)^3} e^{-i\bar{\mathbf{k}} \cdot \bar{\mathbf{x}}} \left( \bar{\mathbf{E}}^{(1)}(t=0), \bar{\mathbf{B}}^{(1)}(t=0), f^{(1)}(t=0) \right) . \quad (61)$$



A-6696

Figure 12. Coordinate system with magnetic field along the z-axis.



Note that the initial values  $\bar{e}, \bar{b}, \bar{g}$  have been collected in  $\bar{I}$ . In addition we have adopted a coordinate system with the constant magnetic field along the z-axis and  $\bar{k}$  in the x-z plane.

Equation (59) is conveniently written in the form

$$(s^2 + c^2 k^2) \bar{E} - c^2 \bar{k}(\bar{k} \cdot \bar{E}) + 4\pi s \hat{\sigma} \cdot \bar{E} = \bar{I} \quad (62)$$

where  $\hat{\sigma}$  is the conductivity tensor, defined through

$$\bar{J} = \hat{\sigma} \cdot \bar{E} \quad (63)$$

Equation (62) is also in the form

$$\hat{R} \cdot \bar{E} = \bar{I} \quad (64)$$

where  $\hat{R}$  is a dyadic which may be written as a 3x3 matrix, if  $\bar{E}$  and  $\bar{I}$  are written as three-component column vectors. Equation (64) has solution

$$\bar{E} = \frac{\hat{R}^C \cdot \bar{I}}{R} \quad (65)$$

where  $R$  is the determinant of the matrix  $R_{ij}$  and  $R_{ij}^C$  is the transpose of a matrix whose elements are the co-factors of the corresponding elements of  $R_{ij}$ . The elements of  $R_{ij}$  are to be obtained from Eqs. (62) and (63). The last term on the lhs of Eq. (62), i.e., Eq. (63) is the complicated part.

Subsequently we will be interested in implementing the electrostatic approximation  $\nabla \times \bar{E} = 0$ , which implies the relation  $\bar{k} \times \bar{E} = 0$  for the Fourier coefficients. Assuming a zero order distribution  $f_0 = f_0(p_\perp, p_\parallel)$ , Eq. (64) can be evaluated explicitly. The result is

$$\begin{pmatrix} R_{xx} & R_{xy} & R_{xz} \\ R_{yx} & R_{yy} & R_{yz} \\ R_{zx} & R_{zy} & R_{zz} \end{pmatrix} \begin{pmatrix} E_x \\ E_y \\ E_z \end{pmatrix} = \begin{pmatrix} I_x \\ I_y \\ I_z \end{pmatrix} \quad (66)$$

where

$$\begin{aligned}
R_{xx} &= s^2 + c^2 k_{||}^2 - 2s\pi \sum_n \frac{\omega_p^2}{\Omega_0} \int_{-\infty}^{\infty} dp_{||} \int_0^{\infty} p_{\perp}^2 dp_{\perp} \frac{n^2 \Omega^3 J_n^2(\partial f_0 / \partial p_{\perp})}{k_{\perp}^2 v_{||}^2 (s + i k_{||} v_{||} + i n \Omega)} \\
R_{xy} &= -R_{yx} = -2is\pi \sum_n \frac{\omega_p^2}{\Omega_0} \int_{-\infty}^{\infty} dp_{||} \int_0^{\infty} p_{\perp}^2 dp_{\perp} \frac{n \Omega^2 J_n J'_n(\partial f_0 / \partial p_{\perp})}{k_{\perp} v_{||} (s + i k_{||} v_{||} + i n \Omega)} \\
R_{xz} &= -c^2 k_{\perp} k_{||} - 2\pi s \sum_n \frac{\omega_p^2}{\Omega_0} \int_{-\infty}^{\infty} dp_{||} \int_0^{\infty} p_{\perp}^2 dp_{\perp} \frac{n \Omega^2 J_n^2(\partial f_0 / \partial p_{||})}{k_{\perp} v_{||} (s + i k_{||} v_{||} + i n \Omega)} \\
R_{yy} &= s^2 + c^2 k_{\perp}^2 - 2\pi s \sum_n \frac{\omega_p^2}{\Omega_0} \int_{-\infty}^{\infty} dp_{||} \int_0^{\infty} p_{\perp}^2 dp_{\perp} \frac{\Omega (J'_n)^2 (\partial f_0 / \partial p_{||})}{(s + i k_{||} v_{||} + i n \Omega)} \\
R_{yz} &= 2\pi is \sum_n \frac{\omega_p^2}{\Omega_0} \int_{-\infty}^{\infty} dp_{||} \int_0^{\infty} p_{\perp}^2 dp_{\perp} \frac{\Omega J_n J'_n (\partial f_0 / \partial p_{||})}{(s + i k_{||} v_{||} + i n \Omega)} \quad (67) \\
R_{zx} &= -c^2 k_{||} k_{\perp} - 2\pi s \sum_n \frac{\omega_p^2}{\Omega_0} \int_{-\infty}^{\infty} p_{||} dp_{||} \int_0^{\infty} p_{\perp} dp_{\perp} \frac{n \Omega^2 J_n^2(\partial f_0 / \partial p_{\perp})}{k_{\perp} v_{||} (s + i k_{||} v_{||} + i n \Omega)} \\
R_{zy} &= -2\pi is \sum_n \frac{\omega_p^2}{\Omega_0} \int_{-\infty}^{\infty} p_{||} dp_{||} \int_0^{\infty} p_{\perp} dp_{\perp} \frac{\Omega J_n J'_n (\partial f_0 / \partial p_{\perp})}{(s + i k_{||} v_{||} + i n \Omega)} \\
R_{zz} &= s^2 + c^2 k_{\perp}^2 - 2\pi s \sum_n \frac{\omega_p^2}{\Omega_0} \int_{-\infty}^{\infty} p_{||} dp_{||} \int_0^{\infty} p_{\perp} dp_{\perp} \frac{\Omega J_n^2 (\partial f_0 / \partial p_{||})}{(s + i k_{||} v_{||} + i n \Omega)}
\end{aligned}$$

The above sums are defined for  $R_e s > 0$ , and the argument of the Bessel functions is  $k_{\perp} v_{||} / \Omega = k_{\perp} p_{\perp} / m_0 \Omega_0$ . The unlabeled sums run over charge species. In arriving at Eq. (67), use has been made of the Bessel function identities

$$\int_0^{2\pi} d\phi e^{-iz[\sin(\phi-\alpha) - \sin \phi]} \begin{bmatrix} \sin \phi \sin(\phi-\alpha) \\ \sin \phi \cos(\phi-\alpha) \\ \cos \phi \sin(\phi-\alpha) \\ \cos \phi \cos(\phi-\alpha) \\ 1 \\ \sin \phi \\ \cos \phi \\ \sin(\phi-\alpha) \\ \cos(\phi-\alpha) \end{bmatrix} = 2\pi \sum_{n=-\infty}^{+\infty} e^{in\alpha} \begin{bmatrix} (J'_n)^2 \\ -\frac{in}{z} J_n J'_n \\ +\frac{in}{z^2} J_n J'_n \\ \frac{n}{z^2} J_n^2 \\ J_n^2 \\ -iJ_n J'_n \\ \frac{n}{z} J_n^2 \\ iJ_n J'_n \\ \frac{n}{z} J_n^2 \end{bmatrix} \quad (68)$$

The equation  $R=0$  will be studied below and will be described as the  $t \rightarrow \infty$  "dispersion relation", but we must bear in mind that the residues from the poles of the reciprocal of  $R$  give only a part of the asymptotic  $t \rightarrow \infty$  solution. These results reduce to the "cold" wave results in the double limit  $\gamma \rightarrow 1$  and  $T \rightarrow 0$ . The first limit is simply the nonrelativistic limit. For a more detailed derivation of these results the reader should consult Montgomery and Tidman (1964).

### 3.4.2 Dispersion Relation for a "Hot" Plasma in a Magnetic Field

The system consists of a background electron-ion plasma and streaming ions. We fix coordinates on the background ion-electron plasma and take

$$\begin{aligned} \vec{B} &= (0, 0, B_0) = B_0 \hat{z} \\ \vec{k} &= (k_x, 0, k_z) = k_{\perp} \hat{x} + k_{\parallel} \hat{z} \\ \vec{u} &= (V, 0, 0) = V_{\perp} \hat{x} \end{aligned} \quad (69)$$

In this calculation we make the electrostatic approximation. This implies that only the terms (67) are present and  $\omega/kc \ll 1$ . More explicitly we look at frequencies

$$kV_{\perp} \ll \omega \ll kc, \quad (70)$$

where  $V_{\perp}$  refers to the streaming velocity. If the initial perturbations  $\bar{e}, \bar{b}, \bar{g}$  are identically zero, then  $\bar{I} \approx \bar{O}$ .

The background distribution is taken to be:

$$f_0 = \frac{1}{2\pi m_0 \gamma^2 k_B T_{\perp}} \cdot \left( \frac{1}{2\pi m_0 \gamma^2 k_B T_{\parallel}} \right)^{1/2} e^{-\frac{p_{\parallel}^2}{2m_0 \gamma^2 k_B T_{\parallel}} - \frac{p_{\perp}^2}{2m_0 \gamma^2 k_B T_{\perp}}}, \quad (71a)$$

while the streaming ion distribution is:

$$f_0 \xrightarrow[T_{\perp} \rightarrow 0]{T_{\parallel} \rightarrow 0} \delta(p_{\parallel}) \delta(p_{\perp} - P) \quad (71b)$$

The delta function normalization is

$$\int_{-\infty}^{+\infty} dp_{\parallel} \delta(p_{\parallel}) = 1$$

$$\int_0^{2\pi} d\phi \int_0^{\infty} dp_{\perp} p_{\perp} \delta(p_{\perp} - P) = 1 \quad (72)$$

Letting  $|R| = 0$  and keeping only the largest contributions (recall  $kc \gg \omega$ ) in analogy to the "cold" plasma calculation we find, upon dividing by  $c^4 k_{\perp}^2 k_{\parallel}^2 s^2$ :

$$\hat{R}_{xx} + \left( \frac{k_{\parallel}}{k_{\perp}} \right)^2 \hat{R}_{zz} + \left( \frac{k_{\parallel}}{k_{\perp}} \right) \frac{1}{s} (\hat{R}_{xz} + \hat{R}_{zx}) = 0 \quad (73)$$

where

$$\begin{aligned}
\hat{R}_{xx} &= 1 - \frac{2\pi}{s} \sum \frac{\omega_p^2}{\Omega_o} \sum_n \int_{-\infty}^{+\infty} dp_{||} \int_0^{\infty} dp_{\perp} p_{\perp}^2 \frac{n^2 \Omega_o^3 J_n^2(\partial f_o / \partial p_{\perp})}{k_{\perp}^2 v_{\perp}^2 (s + ik_{||} v_{||} + i n \Omega)} \\
\hat{R}_{zz} &= 1 - \frac{2\pi}{s} \sum \frac{\omega_p^2}{\Omega_o} \sum_n \int_{-\infty}^{+\infty} dp_{||} p_{||} \int_0^{\infty} dp_{\perp} p_{\perp} \frac{\Omega_o J_n^2(\partial f_o / \partial p_{||})}{(s + ik_{||} v_{||} + i n \Omega)}
\end{aligned} \tag{74}$$

$$\begin{aligned}
\hat{R}_{xz} &= -2\pi \sum \frac{\omega_p^2}{\Omega_o} \sum_n \int_{-\infty}^{+\infty} dp_{||} \int_0^{\infty} dp_{\perp} p_{\perp}^2 \frac{n \Omega_o^2 J_n^2(\partial f_o / \partial p_{||})}{k_{\perp} v_{\perp} (s + ik_{||} v_{||} + i n \Omega)} \\
\hat{R}_{zx} &= -2\pi \sum \frac{\omega_p^2}{\Omega_o} \sum_n \int_{-\infty}^{+\infty} dp_{||} p_{||} \int_0^{\infty} dp_{\perp} p_{\perp} \frac{n \Omega_o^2 J_n^2(\partial f_o / \partial p_{\perp})}{k_{\perp} v_{\perp} (s + ik_{||} v_{||} + i n \Omega)}
\end{aligned}$$

We further restrict our attention to the case  $k_{||}/k_{\perp} \ll 1$  and keep lowest order terms only.

$$\frac{1}{k_{\perp} (s + i n \Omega + ik_{||} v_{||})} \approx \frac{1}{k_{\perp} (s + i n \Omega)} \left[ 1 - \frac{ik_{||} v_{||}}{s + i n \Omega} + \dots \right] \tag{75}$$

Under these circumstances, the matrix elements  $\hat{R}$  in Eq. (74) simplify. Since  $f_o$  is even in  $p_{||}$  for either of the distributions (71a, 71b), it is clear that  $\hat{R}_{xz} = \hat{R}_{zx} = 0$ .

The dispersion relation becomes:

$$\hat{R}_{xx} + \left( \frac{k_{||}}{k_{\perp}} \right)^2 \hat{R}_{zz} = 0 \tag{76}$$

The matrix elements  $\hat{R}_{xx}$ ,  $\hat{R}_{zz}$  can be found by evaluating the momentum integrals and simplifying the sums over  $n$ . We get, for background species

$$\hat{R}_{xx} = 1 + 2 \sum \frac{\omega_p^2 m_o^2 \Omega_o^2}{\gamma^2 k_B^T k_{||}^2} e^{-\frac{\gamma^2 k_B^T k_{||}^2}{m_o \Omega_o^2}} \sum_{n=1}^{\infty} \frac{n^2 I_n}{s^2 + n^2 \Omega_o^2} \quad (77a)$$

$$\hat{R}_{zz} = 1 + \frac{1}{s} \sum \omega_p^2 e^{-\frac{\gamma^2 k_B^T k_{||}^2}{m_o \Omega_o^2}} \left[ \frac{I_o}{s} + 2s \sum_{n=1}^{\infty} \frac{I_n}{s^2 + n^2 \Omega_o^2} \right] \quad (77b)$$

where the argument of  $I_n$  is  $I_n = I_n \left( \frac{\gamma^2 k_B^T k_{||}^2}{m_o \Omega_o^2} \right)$

In obtaining Eq. (77), we have noted that

$$(i) \quad \int_{-\infty}^{+\infty} dp_{||} e^{-\frac{p_{||}^2}{2m_o \gamma^2 k_B^T}} = \sqrt{2\pi m_o \gamma^2 k_B^T} \quad (78a)$$

$$(ii) \quad \int_{-\infty}^{\infty} dp_{||} p_{||}^2 J_n^2 e^{-\frac{p_{||}^2}{2m_o \gamma^2 k_B^T}} = m_o \gamma^2 k_B^T e^{-\frac{\gamma^2 k_B^T k_{||}^2}{m_o \Omega_o^2}} \quad (78b)$$

see Watson (1966, pg. 395)

with 
$$I_n = I_n \left( \frac{\gamma^2 k_B^T k_{||}^2}{m_o \Omega_o^2} \right) .$$

$$\begin{aligned}
\text{(iii)} \quad \sum_{n=-\infty}^{+\infty} \frac{n^2 I_n}{s + i n \Omega} &= s \sum_n \frac{n^2 I_n}{s^2 + n^2 \Omega^2} - i \Omega \sum_n \frac{n^3 I_n}{s^2 + n^2 \Omega^2} \\
&= 2s \sum_{n=1}^{\infty} \frac{n^2 I_n}{s^2 + n^2 \Omega^2} \quad . \quad (79)
\end{aligned}$$

The streaming ions are taken to be cold and unmagnetized, i.e.,  $\bar{B} = 0 \Rightarrow v_{\perp}/\Omega \rightarrow \infty$ , i.e., an infinite Larmor radius. Rather than proceed as above we present a derivation of the weak magnetic field limit of Eq. (59), and then evaluate  $\hat{R}_{xx}$ ,  $\hat{R}_{zz}$  for the distribution of Eq. (71b). In the weak magnetic field limit we can expand the third term of Eq. (59) by successive integrations by parts. Thus suppose we write

$$A(\phi') = \left[ \bar{E} - \frac{i}{s} \bar{v}' \times (\bar{k} \times \bar{E}) \right] \cdot \frac{\partial f_0}{\partial \bar{p}'} \quad (80)$$

The last term on the left of Eq. (59) is then

$$s \sum_{-\infty}^{+\infty} \omega_p^2 \int_{-\infty}^{+\infty} d\bar{p} \frac{\bar{p}}{\gamma} I \quad (81a)$$

where

$$I = \int_{-\infty}^{\phi} d\phi' \frac{G(\phi')}{\Omega} A(\phi') = + \int_{\infty}^{\phi} d\phi' \frac{A(\phi')}{(s + i \bar{k} \cdot \bar{v}')} \frac{\partial G}{\partial \phi'} \quad (81b)$$

In arriving at this last result we have used Eq. (60) to obtain

$$\frac{G}{\Omega} = + \frac{\partial G / \partial \phi'}{(s + i \bar{k} \cdot \bar{v}')} \quad (82)$$

If we now successively integrate Eq. (81b) by parts and substitute  $G/Q$  using Eq. (60), a series results, namely:

$$I = + \frac{A(\phi)}{s + i\bar{k} \cdot \bar{v}} - \frac{Q}{(s + i\bar{k} \cdot \bar{v})} \frac{\partial}{\partial \phi} \left( \frac{A(\phi)}{s + i\bar{k} \cdot \bar{v}} \right) + \frac{Q}{(s + i\bar{k} \cdot \bar{v})} \frac{\partial}{\partial \phi} \left[ \frac{Q}{(s + i\bar{k} \cdot \bar{v})} \frac{\partial}{\partial \phi} \left( \frac{A(\phi)}{s + i\bar{k} \cdot \bar{v}} \right) \right] - \dots \quad (83)$$

where we also have noted  $G(\phi=\phi'; \phi') = 1$ .

To zero order in  $Q$ , Eq. (59) reduces to

$$(s^2 + c^2 k^2) \bar{E} - c^2 \bar{k} (\bar{k} \cdot \bar{E}) - s \sum \omega_p^2 \int \frac{d\bar{p} \bar{p}}{\gamma(s + i\bar{k} \cdot \bar{v})} \left[ \bar{E} - \frac{i}{s} \bar{v} \times (\bar{k} \times \bar{E}) \right] \cdot \frac{\partial f_o}{\partial \bar{p}} = I \quad (84)$$

For  $kv \ll \omega$ , Eq. (84) becomes:

$$(s^2 + c^2 k^2) \bar{E} - c^2 \bar{k} (\bar{k} \cdot \bar{E}) - s \sum \omega_p^2 \int d\bar{p} \frac{\bar{p}}{\gamma(s + i\bar{k} \cdot \bar{v})} \bar{E} \cdot \frac{\partial f_o}{\partial \bar{p}} = I \quad (85)$$

Thus, using cylindrical coordinates, we thus must evaluate:

$$\hat{R}_{xx} = -s \sum \frac{\omega_p^2}{\gamma} \int_{-\infty}^{+\infty} dp_{||} \int_0^{\infty} dp_{\perp} p_{\perp} \int_0^{2\pi} d\phi p_{\perp} \cos^2 \phi \frac{(\partial f_o / \partial p_{\perp})}{s + i\bar{k}_{\perp} \bar{v}_{\perp}} \quad (86a)$$

$$\hat{R}_{zz} = -s \sum \frac{\omega_p^2}{\gamma} \int_{-\infty}^{+\infty} dp_{||} \int_0^{\infty} dp_{\perp} p_{\perp} \int_0^{2\pi} d\phi p_{||} \frac{(\partial f_o / \partial p_{||})}{s + i\bar{k}_{||} \bar{v}_{||}} \quad (86b)$$

where  $f_o$  is given by Eq. (81b) subject to the normalization Eq. (82). Straightforward integrations lead to



$$\hat{R}_{xx} = + \sum \frac{\omega_p^2}{\gamma} \frac{s^2}{(s + ik_{\perp} v_{\perp})^2} \quad (87a)$$

$$\hat{R}_{zz} = + \sum \frac{\omega_p^2}{\gamma} \frac{s}{(s + ik_{\perp} v_{\perp})} \quad (87b)$$

where  $v_{\perp} = p_{\perp}/\gamma m_0$ . Subsequently, we shall be interested in the nonrelativistic limit  $\gamma=1$ .

Restricting ourselves to frequencies

$$\Omega_{i,b} \ll \omega \ll \Omega_e \quad (88)$$

and writing

$$s = -i\omega \quad (89)$$

we obtain for the physical system under consideration

$$\begin{aligned} \hat{R}_{xx} = 1 + \frac{2\omega_{pe}^2 m_e}{k_{B\perp}^2 k_{\perp}^2} e^{-\frac{k_{B\perp}^2 k_{\perp}^2}{m_e \Omega_e^2}} \sum_{n=1}^{\infty} I_{ne} \\ - \frac{2\omega_{pi}^2 m_i \Omega_i^2}{k_{B\perp}^2 k_{\perp}^2 \omega^2} e^{-\frac{k_{B\perp}^2 k_{\perp}^2}{m_i \Omega_i^2}} \sum_{n=1}^{\infty} n^2 I_{ni} - \frac{\omega_{pb}^2}{(\omega - k_{\perp} v_{\perp})^2} \quad (90a) \\ \hat{R}_{zz} = 1 + \omega_p^2 e^{-\frac{k_{B\perp}^2 k_{\perp}^2}{m_e \Omega_e^2}} \left[ \frac{-I_{oe}}{\omega^2} + \frac{2}{\Omega_e^2} \sum_{n=1}^{\infty} \frac{I_{ne}}{n^2} \right] \end{aligned}$$

$$- \omega_{pi}^2 e^{-\frac{k_B T_i k_{\perp}^2}{m_i \Omega_i^2}} \left[ \frac{+I_{oi}}{\omega^2} + \frac{2}{\omega^2} \sum_{n=1}^{\infty} I_{ni} \right] - \frac{\omega_{pb}^2}{\omega(\omega - k_{\perp} v_{\perp})} \quad (90b)$$

In Eqs. (90a) and (90b) the subscripts e,i,b refer to electrons, background ions and beam ions, respectively.

For the sake of compactness of notation we introduce a number of definitions:

$$Z \begin{pmatrix} 1 \\ 2 \\ 3 \end{pmatrix} = \frac{2m_o \Omega^2}{k_B T_{\perp} k_{\perp}^2} - \frac{k_B T_{\perp} k_{\perp}^2}{m_o \Omega^2} \sum_{n=1}^{\infty} I_n \begin{pmatrix} 1 \\ n^2 \\ 1/n^2 \end{pmatrix} \quad (91)$$

$$v_{te} = \left( \frac{k_B T_e}{m_e} \right)^{1/2} \quad (\text{electron thermal velocity}) \quad (92a)$$

$$v_{ti} = \left( \frac{k_B T_i}{m_i} \right)^{1/2} \quad (\text{ion thermal velocity}) \quad (92b)$$

$$\omega_{lh}^2 = \frac{\omega_{pi}^2}{1 + \frac{\omega_{pe}^2}{\Omega_e^2} Z_{1e}} \quad (\text{lower hybrid frequency}) \quad (93)$$

$$\text{and} \quad \delta^2 = (k_{||}/k_{\perp})^2 \frac{m_i}{m_e} \frac{N_e}{N_i} \quad (94)$$

In addition recall the following plasma frequency relations:

$$\omega_{pe}^2 = \frac{m_i}{m_e} \frac{N_e}{N_i} \omega_{pi}^2 \quad (95a)$$

$$\omega_{pb}^2 = \frac{m_i}{m_b} \frac{N_b}{N_i} \omega_{pi}^2 = \epsilon_r \omega_{pi}^2 \quad (95b)$$

Substituting Eqs. (90a) and (90b) in the dispersion relation (Eq. (86)), dropping  $(k_{||}/k_{\perp})^2$  as well as terms of order  $(k_{||}/k_{\perp})^2 \omega_{pb,i}^2$ , we obtain upon making use of definitions (91) through (95) our final simplified dispersion relation

$$\begin{aligned} & \omega_{lh}^2 \left[ Z_{2i} + \delta^2 e^{-\left(\frac{k_{\perp} v_{te}}{Q_e}\right)^2} I_{0e} \right] \frac{1}{\omega^2} + \epsilon_r \frac{\omega_{lh}^2}{(\omega - k_{\perp} v_{\perp})^2} \\ & = 1 + \delta^2 \frac{\omega_{lh}^2}{Q_e^2} \left( \frac{k_{\perp} v_{te}}{Q_e} \right)^2 Z_{3e} \end{aligned} \quad (96)$$

Introducing the shorthand notation

$$\Phi = \omega_{lh}^2 \left[ Z_{2i} + \delta^2 e^{-\left(\frac{k_{\perp} v_{te}}{Q_e}\right)^2} I_{0e} \right] \quad (97)$$

$$\Delta = 1 + \delta^2 \frac{\omega_{lh}^2}{Q_e^2} \left( \frac{k_{\perp} v_{te}}{Q_e} \right)^2 Z_{3e} \quad (98)$$

The dispersion relation (Eq. (97)) may be rewritten more simply as:

$$\frac{\Phi}{\omega^2} + \frac{\epsilon_r \omega_{lh}^2}{(\omega - k_{\perp} v_{\perp})^2} = \Delta \quad (99)$$

For computational purposes Eq. (99) can be expressed as a quartic polynomial:

$$\omega^4 - 2\Delta k_{\perp} v_{\perp} \omega^3 + \left[ \Delta(k_{\perp} v_{\perp})^2 - \Phi - \epsilon_r \omega_{lh}^2 \right] \omega^2 + 2\Phi k_{\perp} v_{\perp} \omega - \Phi(k_{\perp} v_{\perp})^2 = 0 \quad (100)$$

### 3.4.3 Parametric Study of CIV

In this section we study the "warm" plasma dispersion relation developed previously. From an inspection of the dispersion relation, the independent parameters are  $k_{||}/k_{\perp}$ ,  $m_e/m_i$ ,  $\epsilon_r$ ,  $\omega_{pe}/\Omega_e$ ,  $v_{the}/v_{thi}$ , and  $v_{\perp}/v_{thi}$ . In what follows we examine the dependence of the maximum growth of unstable waves on each of these parameters.

The electron densities and magnetic field lie in the ranges

$$10^4 \leq n_e \leq 5 \times 10^6 \quad \text{\#}/\text{cm}^3$$

$$0.3 \leq B \leq 0.45 \quad \text{gauss}$$

so that

$$0.7 \leq \omega_{pe}/\Omega_e \leq 24$$

Adopting the nominal values of  $\bar{n} = 5 \times 10^5 \text{ cm}^{-3}$  and  $B = 0.38 \text{ gauss}$  gives us a nominal  $\omega_{pe}/\Omega_e = 6$ . The gas species that are to be ejected in the experiment are Ne, Xe, NO, and CO<sub>2</sub>. Assuming the plasma ions are essentially all O<sup>+</sup> gives us a range for the ratio of beam ion mass to background plasma ion mass of

$$1 \lesssim m_b/m_i \lesssim 8$$

This ratio appears in  $\epsilon_r = (N_b/N_i) \cdot (m_i/m_b)$ , which determines a scaling law, namely a given  $\epsilon_r$  may be obtained by increasing  $N_b/N_i$  and decreasing  $m_i/m_b$  or vice-versa. Taking the beam velocity  $v_{\perp}=1$  unit gives a range for the ion and electron thermal velocities

$$0.07 \lesssim v_{thi} \lesssim 0.09$$

$$1.2 \lesssim v_{the} \lesssim 2$$

Our nominal values are  $v_{thi} = 0.088$ , and  $v_{the} = 1.4$ . The thermal velocities were calculated from  $v_{the} = 4.19 \times 10^7 T_e^{1/2}$  and  $v_{thi} = 9.79 \times 10^5 \mu^{-1/2} T_i^{1/2}$ , where  $T_e$ ,  $T_i$  are the electron and ion temperatures in eV and  $\mu$  is the ion mass expressed in units of the proton mass. The range of temperatures of interest are  $0.08 \leq T_e \leq 0.2$  eV,  $0.05 \leq T_i \leq 0.10$  eV. Normalizing thermal velocities to the beam velocity and using a model mass ratio of  $m_e/m_i = 1/400$ , so that effectively we are using an electron mass that is 137 times as large as the physical mass of the electron, gives the above range. We summarize first the results for the dependence of the maximum growth rate on  $\epsilon_r$ . The fixed parameters are

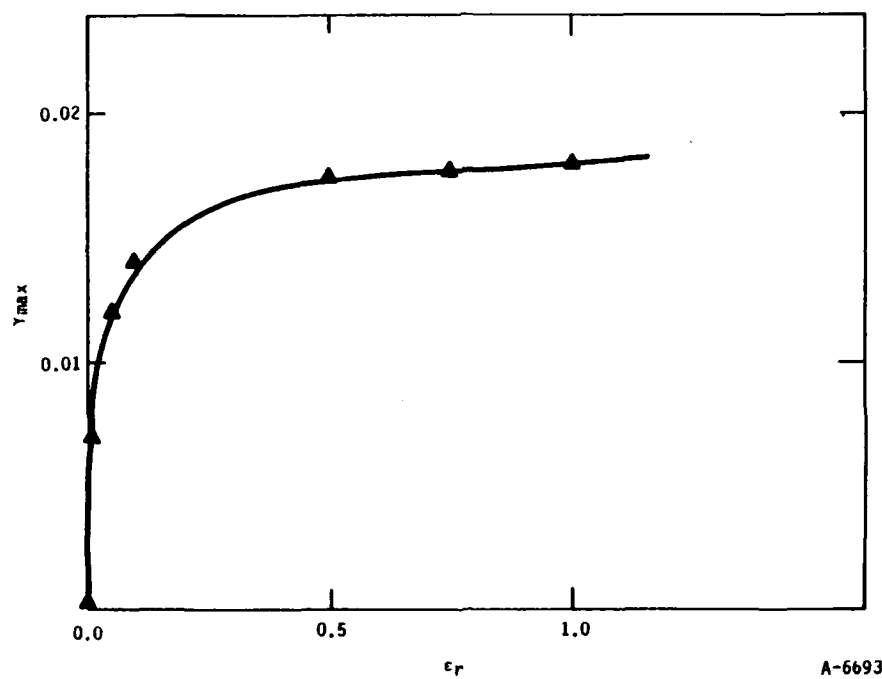
$$k_z/k_x = 0.05 = (m_e/m_i)^{1/2} \quad v_{\perp} = 1$$

$$m_e/m_i = 1/400 \quad v_{thi} = 0.088$$

$$\omega_{pe}/\Omega_e = 6 \quad v_{the} = 1.4$$

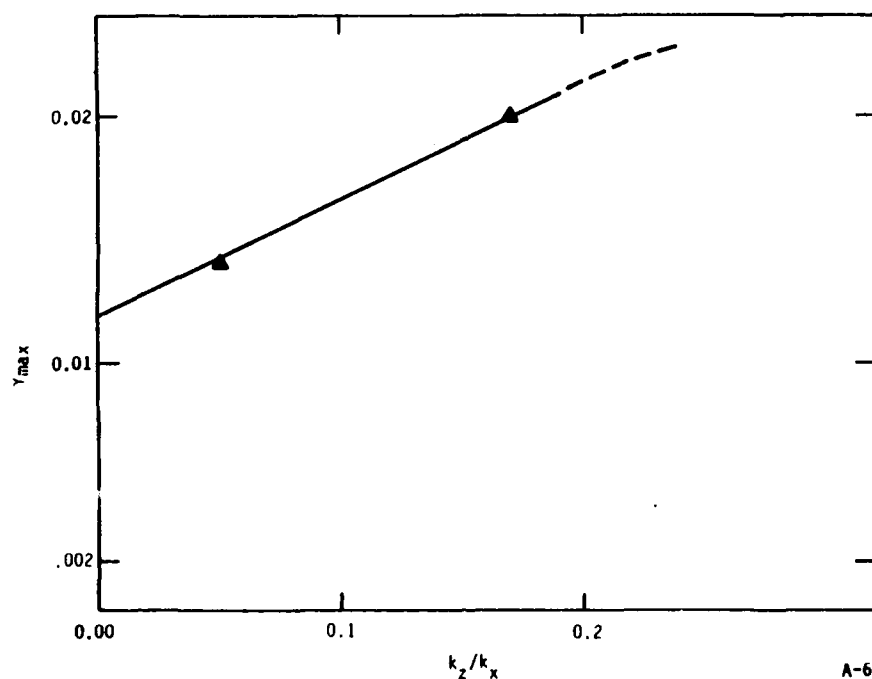
$$m_i/m_h = 1/3$$

The results are summarized in Figure 13.  $\gamma_{max}$  increases with  $\epsilon_r$  rapidly at first then saturates to  $\gamma_{max} \approx 0.018$ . This corresponds to  $N_b/N_i = 3$ , i.e., our beam density is three times as large as the background density. However the growth is appreciable even for low values of  $N_b/N_i$ . Figure 14 shows the dependence of growth rate on  $k_{||}/k_{\perp}$  which gives the inclination of the  $k$  vector relative to the direction of particle displacement and the self-consistent electric field, i.e., the  $x$ -direction. In the range of validity of the dispersion relation  $k_{||}/k_{\perp} \ll 1$ , so that the maximum growth rate increases as we fall away from the perpendicular direction. However, from preliminary simulations electron heating is maximized at  $k_{||}/k_{\perp} \approx (m_e/m_i)^{1/2}$ . Finally, Figure 15 illustrates the dependence of the maximum growth rate on  $\omega_{pe}/\Omega_e$ . Here again it increases and saturates at approximately



A-6693

Figure 13. Parametric dependence of maximum growth rate on ratio of beam to background number densities.



A-6694

Figure 14. Parametric dependence of maximum growth rate on ratio of parallel to perpendicular components of wave vector.

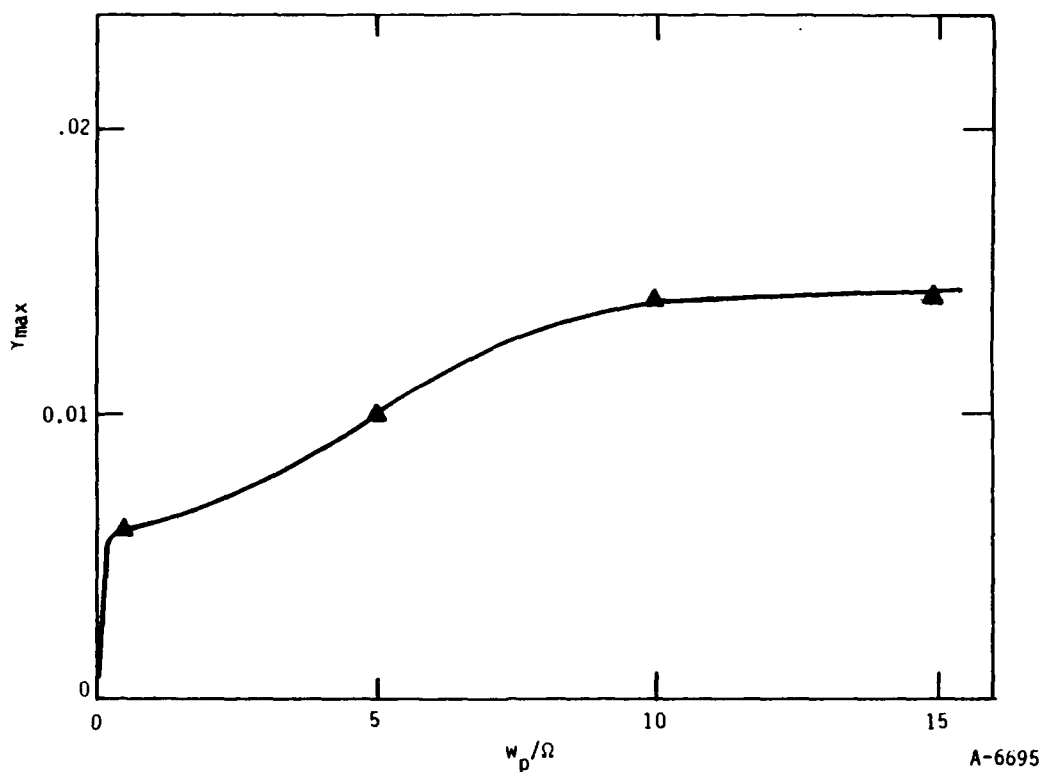


Figure 15. Parametric dependence of maximum growth rate on ratio of electron plasma to cyclotron frequencies.

### 3.5 COMPUTER SIMULATION OF MOLECULAR AND PLASMA EFFECTS

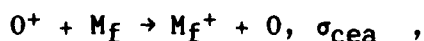
#### 3.5.1 Introduction

There is a rich variety of molecular physics involved in a plasma that is producing ionization via the CIV effect. The CIV effect seems to be more complicated than first thought. For example, the critical velocity for a discharge to occur is larger than  $v_c$  because only a fraction of the kinetic energy of the fast ions is transferred to the electrons (McBride, et al., 1972; Galeev, 1981) and because some of the electron energy goes to produce excitation rather than ionization (Newell and Torbert, 1985). The latter result could have been anticipated from the results of radiation physics studies (e.g., Platzman, 1961). However, some of the energy that goes into excitation may be recovered as a result of ionization of metastable states

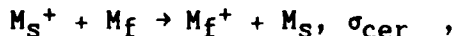
(McNeil, Lai, and Murad, 1987). Another factor that can influence ionization by CIV is the loss of ions through recombination (Murad, et al., 1986) and ion diffusion (Caledonia, et al., 1987).

There are many effects that must be considered in order to predict CIV effects. These effects include:

1. Seed ionization to initially produce the fast ions from ionization of fast neutrals in an event with low momentum transfer. This ionization could come from photoionization, ionization by fast electrons present in the ambient ionosphere, charge exchange collisions with ambient ions, and collisions with fast neutral molecules or atoms from the ambient. A comparison of the rates of these processes shows that charge exchange is the dominant process, at least for the species that have an ionization potential low enough to permit exothermic charge exchange with ionospheric ions (Caledonia, et al., 1987).
2. Charge exchange processes must be considered separately, even if they are not important in producing the seed ionization. There are two different types: charge exchange from the ambient ions (which are predominantly  $O^+$ ) to form fast ions



which has a cross section of  $\sigma_{cea}$ , and resonant charge exchange, where one beam ion charge exchanges with a fast neutral beam molecule



where the subscripts refer to slow and fast species. This process is important when the initial ion has been slowed down somewhat, so that the resonant charge exchange process increases the directed kinetic energy along the beam of the fast ions by changing a slow ion into a fast ion.



In the simulation, the ambient charge exchange process produces one new ion from the beam molecules and it removes one ion from the ambient ion population. The charge exchange processes do not change the number of electrons.

3. Plasma effects will heat the electrons and slow the fast ions by developing an electric field that develops as a result of exciting a plasma instability. This effect is discussed more in other sections, and this is the main plasma effect that we wish to simulate. The heating of the electrons is essential to provide the mechanism to increase the charge density. This field also slows the beam ions, which enhances the resonant charge exchange process.
4. Ionization of fast neutrals by these heated electrons is the mechanism to increase the plasma density. This process provides additional fast ions to heat more electrons. This step provides feedback that can produce a discharge under conditions where each fast ion transfers more energy to the plasma electrons than the average energy lost by the electrons to produce another ion pair. As a result of the ionization, there are now two electrons and a new fast ion.
5. Excitation of fast neutrals by electron collisions decreases the energy of the plasma electrons. These excited species can be ionized by low-energy electrons. (Provided that the electrons have an energy greater than  $I - X$ , where  $I$  is the ionization potential of the ground state of the molecule and  $X$  is the excitation energy of the excited state formed.) If the excited species dissociate or radiate before they are ionized, then this step is an energy sink that increases the average energy lost by the electrons to produce an ion pair. We simulate conditions where the excited molecule will usually radiate before it is ionized, so our simulation considers the excitation collisions to remove energy from the electrons.

6. Elastic collisions between the electrons and the fast neutrals will reorient the electron velocity vectors. We ignore the elastic collisions of the electrons with the ambient species, as we presume that the beam number density is much larger than the ambient number density for the regions we simulate. When the neutral density is large enough, there will be resistive heating of the electrons (Machida and Goertz, 1986). In our simulations the neutral number densities are low enough that resistive heating is not important. In our simulations we have ignored the small amount of kinetic energy that can be transferred between the massive neutrals, with a mass  $m_N$ , and the electrons, with mass  $m_e$ . The fractional energy change in a collision is of the order of  $(m_e/m_N)$ , so the major effect of the electron-neutral elastic collisions is to reorient the electron velocity vector.
7. Elastic collisions between the ions and the fast neutrals will reorient the ion velocity vectors and transfer kinetic energy. Again, we ignore the elastic collisions with the ambient neutral species.

### 3.5.2 Equations for CIV Process

In this section we give equations that describe the CIV process in the presence of the molecular physics effects of charge exchange, ionization by electron collision, electron energy loss by excitation collisions, and elastic collisions of electrons and ions with neutrals. We consider three species in the plasma: beam ions that initially have a directed velocity equal to that of the fast neutral beam, ambient ions with no directed velocity, and electrons. Both the electrons and the ambient ions have thermal energies. We consider that the neutral gas molecules can charge exchange with the ambient ions to form beam ions. In this case, we can neglect other ionization processes to form the initial ions (Caledonia, et al., 1987). We start with an initial fraction of the total number of ions as already present as beam ions.

The equation for the density of the beam component is

$$dn_b/dt = \nu_i \alpha_i n_e + \nu_{cea} n_a , \quad (101)$$

where:

$\nu_i$  is the collision frequency for ionizing collisions

$\alpha_i$  is the fraction of electrons with an energy greater than the neutral molecule ionization potential  $I$ , and

$\nu_{cea}$  is the collision frequency for charge exchange collisions with the ambient ions.

The collision frequencies are each related to an average of a cross section  $\sigma$  times the electron velocity  $v_e$

$$\nu = \langle \sigma v_e \rangle n_N , \quad (102)$$

so that  $\nu$  is proportional to the neutral number density.

The equation for the ambient ions is

$$dn_a/dt = - \nu_{cea} n_a . \quad (103)$$

The density change of the electrons is given by

$$dn_e/dt = \nu_i \alpha_i n_e , \quad (104)$$

as we neglect other ionization sources, such as photoionization, as well as loss terms such as recombination and diffusion. We maintain charge neutrality  $n_e = n_b + n_a$ .

The presence of energy gains from charge exchange, energy losses from excitation collisions and from only a fraction of the ion energy being transferred to the electrons will change the critical velocity. Mobius and coworkers (1987) derive the expression

$$v_b > v_c [(1/\eta + \kappa)/(1 + \zeta)]^{0.5} , \quad (105)$$

where  $v_c$  is the conventional critical velocity  $(2I/m_b)^{0.5}$ ,  $\eta$  is the fraction of the fast ion kinetic energy that is transferred to the electrons (which has a value of 0.8 for their derivation),  $\kappa$  is the factor for excitation losses, and  $\zeta$  gives the charge exchange effects. These factors are given by

$$\kappa = \langle \sigma_x v_e \rangle / \langle \sigma_i v_e \rangle , \quad (106)$$

where  $\sigma_x$  and  $\sigma_i$  are the cross sections for excitation and ionization, respectively. Note that we should include as excitations only those excitations that remove energy from the system by processes such as radiation and dissociation. Excited states that live long enough to be ionized are not energy losses, as these states have lower ionization energies (McNeil, Lai, and Murad, 1987). The charge exchange factor is

$$\zeta = f^{-1.33} \sigma_{cea} v_b / \langle \sigma_i v_e \rangle , \quad (107)$$

where  $f = n_b/n_e$  is the fraction of positive ions that are in the beam.

### 3.5.3 Description of Method of Computer Simulation

In order to gain insight into the CIV process, we performed various numerical simulations of plasmas. The simulations use several approximations to represent the physics while still allowing economical calculations. In this section we discuss the approximations that apply to the simulation of plasma effects in plasmas where atomic and molecular physics are absent.

3.5.3.1 Approximations in the Plasma Simulations. These simulations used a modification of the ES1 code, which is a particle-in-cell code developed by Birdsall and coworkers at the University of California (Birdsall and Langdon, 1985; Hasegawa and Birdsall, 1964). The original ES1 code considered one dimension in position space and two dimensions in velocity space (e.g.,  $x$  for

position and  $V_x$  and  $V_y$ ). As discussed earlier we have modified the code to consider three dimensions in velocity space, so that we now consider four of the six coordinates in phase space. The modification allows us to vary the angle  $\psi$  between the magnetic field and the velocity vector of the fast ions. For most of the calculations we consider the velocity vector of the fast ions to be parallel with the electric field vector, and both of these to be parallel to the one positional dimension in the simulation.

The philosophy used by Birdsall is that the simulations are intended to produce the essence of the plasmas, without all of the details. The important physical properties that the simulations have to preserve and the approximations used are discussed next.

1. The plasmas that we simulate are collisionless, as far as electron-electron collisions are concerned. This can be seen from the number of particles in the Debye cube, which is discussed below.
2. We are interested in lengths that are longer than the Debye length,  $\lambda_D$

$$\begin{aligned}\lambda_D &= [kT/(4\pi n_e e^2)]^{0.5} \\ &= 743 T^{0.5} n_e^{-0.5} \text{ cm}\end{aligned}$$

where  $T$  is the electron temperature (eV) and  $n_e$  is the electron number density ( $1/\text{cm}^3$ ). Thus, for  $T = 0.1$  eV and  $n_e = 10^6/\text{cm}^3$ ,  $\lambda_D = 0.23$  cm. The number of electrons in a Debye cube,  $N_D$  is

$$N_D = n_e \lambda_D^3 .$$

This number is large,  $1.2 \times 10^4$ , for the example with  $n_e = 10^6 \text{ cm}^3$ . From  $N_D$  we can show that the plasmas are collisionless, as far as electron-electron collisions are concerned. This is because the collisionless criterion is

$$\nu_e/\omega_{pe} \approx \ln(N_D)/N_D \ll 1.$$

where  $\nu_e$  is the electron-electron collision frequency and  $\omega_{pe}$  is the electron plasma frequency. This criterion can be satisfactorily met for our simulations with  $N_D$  values as low as 10. Another way to estimate  $\nu_e$  is to use the Coulomb cross section for a 90 degree deflection (the cross section for the deflection from multiple collisions is larger than the cross section for the deflection in a single collision), which is

$$\sigma_{90} \approx 2.6 \times 10^{-18}/E_e \text{ cm}^2,$$

when the electron kinetic energy  $E_e$  is given in eV (Krall and Trivelpiece, 1986, p. 294). Then

$$\nu_e = \sigma_{90} \nu_e n_e,$$

which is 1.5 to 150 collisions/s for  $E_e = 1$  eV and  $n_e = 10^4$  to  $10^6$ ; it is a factor of 4 lower when  $E_e = 16$  eV. Thus the assumption of collisionless plasmas seems justified for the simulations, at least for plasma densities lower than  $10^6$ , although it may not be justified for densities larger than  $10^7$ . This is because the growth times are less than 1 ms.

3. The physical picture of a plasma is that the thermal kinetic energy is large in comparison with the potential energy associated with the Coulomb forces between the ions and the electrons. The ratio

$$\text{Thermal Kinetic Energy/Microscopic Potential Energy} = N_D.$$

The fundamental physics of the plasma requires that this ratio is much greater than one, but it does not have to be larger than 10 for the simulation to be effective. Thus we do not have to actually use a simulation with  $10^4$  electrons in a Debye cube; we can get by with only 10. The plasma parameter, which should be much less than one, is the reciprocal of  $N_D$ .

4. In the simulations we use a spatial grid to simplify the calculation of the fields. This has the effect of smoothing away information on the fields and forces at distances less than one grid cell.
5. Periodic boundary conditions effectively make the length of the system infinite. This correctly embodies the physical property that we are interested in lengths much greater than the Debye length, but it fails to consider effects that result from the finite size of the system.
6. The finite size of the ambient plasma and of the fast ion beam are ignored. Also, we do not consider the density variations with distance in this calculation.
7. We assume a uniform flow of neutral particles with a constant flow velocity. The neutral particle number densities are considered to be much greater than the ion number densities, so that we do not need to follow the motion of the individual neutral particles. In the simulations we always consider the fast neutrals to have a fixed velocity of 8 km/s, which is typical of the velocity of the Orbiter. We ignore the perturbation of the neutral density as a result of collisions with neutral particles in the ambient.
8. The ionization of a fast neutral is assumed to make no change in the momentum of the heavy particle, so that the fast ion has the same momentum components that the fast neutral had before the ionization event. This is a good approximation for ionization by electron impact, and it is still a reasonable approximation for ionization by charge exchange.
9. The simulations use artificially small ratios of the mass of the ion to the mass of the electron,  $m_i/m_e$ . We used ratios of 100 to 400, rather than ratios of  $5.1 \times 10^4$  (for  $N_2^+$ ) to  $2.4 \times 10^5$  (for  $Xe^+$ ). This speeds the computation while still preserving the essential physics that the

ions are much more massive than the electrons. Also, we take the ions to be unmagnetized (i.e., they have an infinite gyroradius), which correctly represents another important physical difference between the ions and the electrons.

10. The simulations start with either a beam of fast ions, a background of thermal ions, and a background of thermal electrons, or else they start without the background of thermal ions. In all cases the plasmas are electrically neutral. That is, we take the number of electrons to equal the total number of ions, and the ions are singly charged.
11. The initial velocity distribution of the background electrons and of the background ions are each assumed to be Maxwellian initially. However, the distributions do not remain Maxwellian as the plasma heats. We follow the velocities of the individual particles.

3.5.3.2 Approximations that Should be Tested in Further Work. The validity of some of the approximations made in this analysis has not been fully tested. Their limitations should be evaluated further in future calculations. This section will discuss some of these as well as indicating simple modifications which can be used in the numerical calculations to assess their significance.

1. Finite geometry and spatial variation of background conditions have not been considered. Detailed calculation would clearly involve a significantly more complex computer program. For a finite gas cloud, however, one may anticipate that both wave energy and heated electrons may leave the system. If this happens in times comparable to or less than the times required for the waves or electrons to perform their function, converting directed energy to thermal energy and then ionizing neutrals, one would anticipate that the process would become less efficient.



The effect of wave energy leaving the system can be approximated by assuming a damping rate equal to the group velocity of the wave divided by the size of the region. This damping rate should be subtracted from the instability growth rate and can be incorporated in the numerical analysis. The waves of interest have a group velocity that is predominantly parallel to the magnetic field and is proportional to the parallel component of the wave vector. For typical conditions this damping rate is not negligible for waves of interest. In the numerical calculations the angle of the wave vector has been chosen to correspond to the maximum growth rate in an infinite uniform medium. Including damping would presumably shift the maximum growth rate to smaller values of the parallel component of the wave vector and reduce the magnitude of the maximum growth rate. The overall effect on rate and efficiency of conversion of energy to ionization should be calculated.

The effect of loss of high energy electrons from the region of interest can similarly be estimated by assuming that high energy electrons leave the region at a rate equal to the electron velocity parallel to the magnetic field divided by the size of the region. (At high neutral densities the electron may need to be considered to diffuse out of the region.) This loss of high energy electrons which are then replaced by cold ambient electrons can be added to the computer code as pseudo-collisions. Rough estimates indicate that this process may lead to a noticeable reduction in the efficiency of conversion of energy to ionization.

2. The present analysis assumes that electron-electron collisions do not occur. This is certainly valid for consideration of the wave growth and conversion of energy to electron kinetic energy. However, since electrons transfer energy very efficiently among themselves, the assumption that the electron distribution function becomes non-Maxwellian is not valid under some conditions of interest. The computer code can be modified to assume that the electrons are always Maxwellian but that

the electron temperature rises as the electron energy increases. The net effect of this on ionization efficiency is hard to predict with precision. The non-Maxwellian distribution has more electrons than a Maxwellian at intermediate energies but a sharp cutoff at high energies. Since the ionization rate depends on the number of electrons above the ionization energy, the effect on the rate of ionization will depend on where the cutoff is compared to the ionization energy. The tail of the distribution is expected to extend to electron energies that are at or above the ion kinetic energy (Papadopolous, 1984), which is above the ionization potential. Therefore the Maxwellian distribution is expected to be less efficient at producing ionization.

#### 3.5.4 Details of the Simulation of Molecular Physics

In this section we shall discuss details of how the simulation was performed. The object of the simulations was to learn more about how CIV may occur in a gas release from Orbiter. Thus, it is important to use realistic cross sections in order to see the effects that occur in an actual gas. For this simulation, we used data from nitrogen molecules to represent the processes expected for different gas releases. This simulation has ignored the energy lost to vibrational and rotational excitations. These losses are important when the electron energy is less than the energy for electronic excitation. Thus our estimates of electron heating will exceed that in a real molecular gas. The overestimate is less important for the low-pressure, high neutral beam energy runs where a significant fraction of the electrons are quickly heated above the ionization energy. We now give details of the cross section and angular distribution calculations.

3.5.4.1 Method of Simulating Electron-Neutral Collisions. The procedure is to run the plasma simulation code and allow the electrons to heat. At periodic intervals we call a subroutine to determine if an electron collision (or other molecular physics) has occurred. This is done by using the total cross section for electron-neutral collisions,

$$\sigma_{\text{tot}} = \sigma_{\text{inel}} + \sigma_{\text{el}} ,$$

which is the sum of the inelastic and elastic cross sections calculated for an electron with an energy  $E_e$ . This total cross section is used with the electron velocity  $v_e$  (but scaled to the velocity of an actual electron, rather than the velocity of the simulation electron), and the number density of the fast neutral beam  $n_N$  to compute the mean free time between collisions

$$\tau_c = 1/(\sigma_{\text{tot}} n_N v_e) .$$

This  $\tau_c$  value determines the distribution of times between collisions. We can sample this distribution by finding a random number  $R$  selected from a uniform distribution from 0 to 1 and using the equation

$$\Delta t_R = - \ln(R)/\tau_c .$$

If  $\Delta t_R$  is greater than the time that has elapsed since the last subroutine call, then the simulation considers that the electron in question had a collision. At each collision, another random number is selected to determine the nature of the collision. If this number is less than the fraction of collisions that give elastic collisions (which is equal to  $\sigma_{\text{el}}/\sigma_{\text{tot}}$ ), then the collision is elastic. If the number is larger, then the collision is inelastic and the random number is examined to see which inelastic process is excited. Here  $\sigma_{\text{tot}}$  is considered to be given by

$$\sigma_{\text{tot}} = \sigma_{\text{el}} + \sum \sigma_j (E_e, E_j) ,$$

where  $\sigma_j (E_e, E_j)$  is the inelastic cross section for transfer of an energy  $E_j$  to the neutral molecule. In practice we only used a limited number of  $E_j$  values, with one value (12 eV) to simulate excitation and several values to represent ionization. These values were taken to be the ionization potential ( $I = 15.6$  eV) plus secondary electron energies of 1, 2, 4, 7, 11, 16, 22, 30,

40, 60, and 80 eV. The maximum secondary electron energy in a collision of an electron with an initial energy of  $E_e$  is given by  $0.5(E_e - I)$ .

If the collision is elastic, we find the new direction cosines of the electron by taking two more random numbers, one to give the azimuthal scattering angle  $\phi$  (which is uniformly distributed between 0 and  $2\pi$ ), and one to give the deviation from the original direction  $\theta$ . The  $\theta$  angle is found by integrating the angular distribution  $\sigma_{el}(E_e, \theta)$  times  $\sin(\theta)d\theta$  to give a uniform probability between 0 and the total elastic cross section. The integrated distribution is used with a random number to select the value of the scattering angle  $\theta$ . In this way we allow backscattering to occur, as  $\theta$  varies between 0 and  $\pi$ .

If the collision is inelastic, we find the new direction cosines in a similar manner, except we use the inelastic angular distribution  $\sigma_j(E_e, E_j)$  for scattering by an inelastic collision that transfers an energy  $E_j$ .

The cross sections are functions of the kinetic energy of the electron. Actually, they depend on the kinetic energy of the relative motion of the electron and the neutral molecule. The electrons have much greater velocities than the molecules, even for molecules traveling at 8 km/s, as the electrons travel at  $593 E_e^{0.5}$  km/s, where  $E_e$  is the electron kinetic energy in eV. Thus an electron at 20 eV is traveling at  $2.7 \times 10^3$  km/s. In addition, the actual mass of the ion is  $5 \times 10^4$  (or more) times as great as the mass of the electron. Therefore, we need only consider the motion of the electron. In the simulation, we use cross sections based on actual data to give a realistic energy dependence.

The physical inputs into the simulation are the values of absolute cross sections  $\sigma_{el}(E)$  and  $\sigma_{inelj}(E_e, E_j)$ , the relative cross sections for angular scattering  $\sigma_{el}(E_e, \theta)$  and  $\sigma_{inelj}(E_e, E_j, \theta)$ , the relative cross section for producing a fast secondary electron at an angle  $\theta_s$ ,  $\sigma_{sec}(E_e, E_j, \theta_s)$ . In the next subsections, we shall discuss our choices for each of these values.

3.5.4.2 Absolute Cross Sections for Elastic and Inelastic Scattering. The absolute cross sections (together with the gas number density) are the parameters that determine the length of the path between collisions as well as the distribution of energy losses produced in inelastic collisions. We need a general prescription for determining  $\sigma_{el}(E_e)$  and  $\sigma_{inelj}(E_e, E_j)$  for wide ranges of  $E_e$  and  $E_j$ . For this purpose we have used the expression used by Jackman and Green (1979) (JG) for  $\sigma_{el}$  and the expression given by Porter, Jackman, and Green (1976) (PJG) for  $\sigma_{inel}$ . These expressions give values that compare with the recommended values given by Itikawa, et al. (1986) to within 10 to 20 percent. We have also compared the differential cross section,  $d\sigma_{ionj}(E_e, E_j)/dE_j$ , for producing a secondary electron with an energy ( $E_j$ -15.6) eV with Fig. 9.8 in Itikawa, et al. (1986). Here our values usually are some 5 to 15 percent high.

3.5.4.3 Elastic Scattering Angular Distribution. The relative differential scattering cross section  $\sigma_{el}(E_e, \theta)$  determines the distribution of the angular scattering by elastic processes where the electron energy  $E_e$  is unchanged during the collision. We have used either the general prescription for  $\sigma_{el}(E_e, \theta)$  given by Jackman and Green (1979) or a modification of this distribution. Some simulations were run with a modification where the contribution from small angles is diminished. The modification was to make  $\sigma_{el}(E_e, \theta)$  constant for  $\theta < 3$  deg. The simulations reported here take the angular distribution to be the same for all electron energies below 17 eV, and they use the distribution calculated for 17 eV. The energy dependence of the angular distribution is considered for electron energies greater than 17 eV. The neglect of the energy dependence below 17 eV will reduce the effects of elastic collisions, as the true angular distribution will have a smaller contribution from the forward peak.

3.5.4.4 Inelastic Scattering Angular Distribution. The inelastic scattering can also be simulated by knowing the absolute total cross section and the relative angular distribution. Here we focus on the relative values for  $\sigma_{inelj}(E_e, E_j, \theta)$ . The inelastic scattering of electrons can be described by

using the generalized oscillator strength (GOS) (Inokuti, 1971). A complete knowledge of the GOS provides a method of defining the absolute angular scattering cross section. The GOS has useful properties, such as going to the optical oscillator strength in the limit of zero momentum transfer, and there are general sum rules for various moments (Inokuti, 1971). Porter, Jackman, and Green (PJG) considered these properties in order to fit a parameterized form of the Massey-Mohr-Bethe surface (which is based on the theoretical form of GOS that is known to be correct for H atoms). The fit is given in their equation (14) and in their Table II, with the following corrections (Green, personal communication, 1985): a constant of 0.654 is added to  $\beta_2$  and a constant of 1.0 is added to  $\gamma$ . Our simulations use the total inelastic  $\sigma(E, E_e)$  given by PJG together with the relative angular distributions using  $\sigma(E, E_e)$  derived from their GOS surface.

3.5.4.5 Method of Simulating Ion-Neutral Collisions. The ion-neutral collisions are simulated in a similar manner to the electron-neutral collisions. In both cases, we assume that the neutral number density is uniform, constant, and much larger than the density of ambient species. For this case the subroutine call determines if an ion collision has occurred. This is done by using the total cross section for ion-neutral collisions,

$$\sigma_{ti} = \sigma_{ce} + \sigma_{eli},$$

which is the sum of the charge exchange and elastic cross sections calculated for an ion with an energy  $E_i$ . The cross section for charge exchange with ambient  $O^+$  ions is estimated from the rate for this reaction for a relative velocity of 8 km/s (Albritton, 1978) as  $5 \times 10^{-16} \text{ cm}^2$ . The cross section for resonant charge transfer is needed as a function of relative velocity; we approximated the cross sections from Stebbings and coworkers (1963) as a linear function of the velocity, with  $\sigma_{cer} = 33 \times 10^{-16} \text{ cm}^2$  at  $v_r = 8 \text{ km/s}$  and the slope =  $-2.4 \times 10^{-22} \text{ cm}^2/(\text{cm/s})$ . The elastic cross sections were calculated from an evaluation (Mahan and Person, 1964) corresponding to

scattering from collisions where the potential energy  $P$  is represented as the sum of an ion-induced dipole attraction and a hard-sphere core

$$\begin{aligned} P &= \alpha_p e^2 / (2 R^4) & R > s \\ P &= \infty & R \leq s \end{aligned}$$

The hard sphere radius  $s$  was estimated to be  $2.55 \times 10^{-8}$  and  $3.0 \times 10^{-8}$  cm for  $O^+$  and  $N_2^+$ , respectively, by analogy with Goldschmidt's values (Loeb, 1960). The polarizability  $\alpha_p$  of the neutral is approximated as  $1.76 \times 10^{-24}$  cm<sup>3</sup>, the value for  $N_2$ .

The total cross section is used with the ion velocity  $v_i$  (which was scaled to the velocity of an actual  $O^+$  or  $N_2^+$  ion), and the number density of the fast neutral beam  $n_N$  to compute the distribution of times between collisions. As for the electrons, we use a random number to determine whether the ion in question had a collision. At each collision, another random number is selected to determine the nature of the collision. If this number is less than the fraction of collisions that give elastic collisions (which is equal to  $\sigma_{eli}/\sigma_{ti}$ ), then the collision is elastic. If the number is larger, then the collision gives charge exchange, which is either from the ambient ion or resonant, depending on which type of ion we are following.

If the collision is elastic, the effect of the elastic collision is to rotate the relative velocity vector through some angle  $\chi$  in the center of mass system. The distribution of  $\chi$  favors small values of  $\chi$ , and random choices of  $\chi$  used the angular distribution calculated from the tabulated results for the Langevin potential given above (Mahan and Person, 1964). The choice of  $\chi$  determines the kinetic energy transferred in the collision. In addition we take another random number to give the azimuthal scattering angle  $\phi$ , which then determines the direction cosines of the new ion. Additional details on the elastic scattering calculation can be found in the report by Caledonia, Person, and Hastings (1986). If the collision is charge-exchange, we find the

new direction cosines by assuming that the new fast ion has the same velocity as that of the fast neutral beam.

### 3.5.5 Results of Computer Simulations

The simulation uses enough molecular physics to allow study of several of the competing effects that are related to the CIV process. The number density (pressure) of the neutral beam and the kinetic energy of the fast ions were the major parameters that we varied. There are competing effects that result from increasing the pressure of the neutrals. One effect is to increase the number of elastic collisions between electrons and neutrals. These collisions scatter the electrons, which reorient their velocity vectors. The effect of these collisions is to reduce the electron heating via the interaction with the electric field. In these simulations the effect of the elastic scattering of the electrons is reduced because the low energy electrons have an angular distribution with too large a peak in the forward direction. Approximately 40 percent of the elastic collisions result in deflections that are less than 30 deg. In addition, the neglect of vibrational and rotational excitation collisions will also increase the electron heating in these simulations.

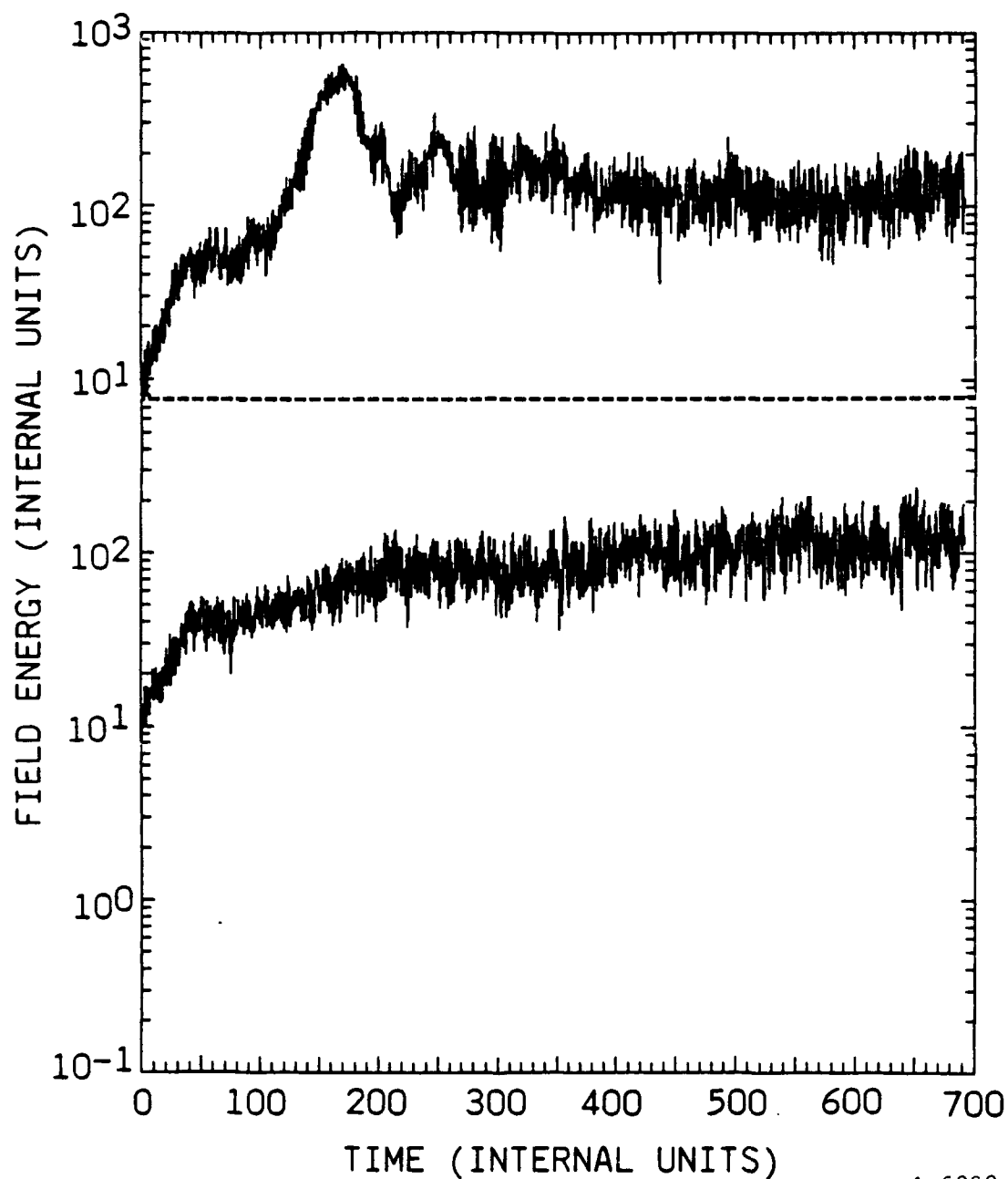
Another effect of increasing the neutral number density is to increase the rate of charge exchange, both with the ambient ions and with the ions in the beam. The resonant charge exchange with ions in the beam has a larger cross section in the simulation ( $\sim 33 \times 10^{-16}$  versus  $5 \times 10^{-16}$  for ambient ions), but the relative velocity for this process is essentially zero unless the beam ion has been slowed somewhat. Thus the resonant charge exchange process is more likely to occur after the electric field has built up and some of the fast beam ions have lost kinetic energy. The resonant charge-exchange process will increase the energy of the beam ions. Charge exchange with the ambient ions will increase the fraction of the ions that are in the fast ion beam. Increasing this fraction increases the electron heating via plasma effects, which increases the ionization via hot electron collisions. The change of this fraction will change the  $k_{\max}$  value for the fastest growing



waves of the instability. Changing  $k_{\max}$  reduces the rate of growth of the electric field energy in comparison to when the fraction of fast ions is constant. On the other hand, when the fraction of beam ions is constant there are other resonance effects that cause the electric field energy to go through a maximum. This is shown by the upper curve in Fig. 16, which is for a run where the neutral density is 1000 times smaller than the lower curve. The lower curve shows the electric field energy for a case where charge exchange occurs, which keeps changing the fraction of beam ions. Here we see that the maximum field energy is less. However, the field energy does not have a maximum. The typical behavior is for the field energy to reach a plateau value (which sometimes occurs rather early), or else the field continues to slowly increase after an initially fast build-up.

Table 1 gives a summary of results from the simulations. The notes to the table contain details about the simulations. In particular note that the times are given in an internal time unit. For a magnetic field of 0.45 Gauss, one unit is 2.16  $\mu\text{s}$  for  $\text{O}^+$ , 2.85  $\mu\text{s}$  for  $\text{N}_2^+$ , 2.95  $\mu\text{s}$  for  $\text{NO}^+$ , 3.58  $\mu\text{s}$  for  $\text{CO}_2^+$ , and 6.17  $\mu\text{s}$  for  $\text{Xe}^+$ . As a result of this time unit, the number densities ( $1/\text{cm}^3$ ) of beam neutral molecules are multiplied by a mass-dependent factor  $F_p$ . The value of  $F_p$  is 84.3 for  $\text{O}^+$ , 112 for  $\text{N}_2^+$ , 116 for  $\text{NO}^+$ , 140 for  $\text{CO}_2^+$ , and 241 for  $\text{Xe}^+$ . In this discussion we shall consider that  $F_p$  is approximately 100, as the value of  $F_p$  is 84 to 113 for ions around the masses used in the simulation, and we take the time unit as approximately 2.5  $\mu\text{s}$  so that the times of 461 and 692 correspond to 1.2 and 1.7 ms, respectively. Note also that the runs initially have 1024 electrons and 1024 positive ions. The table is sorted by  $E_{kb}/I$ ,  $n_N$ , and  $f_b(t=0)$ . The simulations all assume  $V_b = 8 \text{ km/s}$ , so the change in  $E_{kb}/I$  is the result of changing the ionization potential and mass of the beam ion. The column headings are explained at the end of the table.

3.5.5.1 Fraction of Electrons Heated. Table 1 shows that the maximum fraction of electrons heated to an energy greater than  $I/2$ ,  $f_{e1}$ , and the maximum fraction with an energy greater than  $I$ ,  $f_{e2}$ , are both functions of the



A-6929

Figure 16. Field energy for two runs where  $f_{b0}$  is 0.5 and  $E_{kb}$  is I. The upper curve is for run 132 where  $n_N F_p$  is  $3 \times 10^{11}$ , corresponding to  $n_N$  around  $3 \times 10^9/\text{cm}^3$ . The lower curve, run 130, has  $n_N F_p = 3 \times 10^{14}$ . Each internal time unit is approximately  $2.5 \mu\text{s}$ . The initial energy of the beam is  $2.84 \times 10^4$  energy units.

TABLE 1. Summary of simulations for fast ion beam traversing background plasma.

Run	E <sub>kb</sub> /I	nN*Pp	fb0	tli-tlf	t2i-t2f	tion	felmx	fe2mx	t	Nex	Nion	Nele	Nelia	Nelib	Ncea	Ncer	fEf	fEke	fEkb	fEka
117	0.6	1.0E+12	0.5	152-152	169-174	333	0.114	0.056	461	2	1	0.9	0.02	0.02	4	3	0.0038	0.57	0.31	0.114
							0.103	0.026	692	3	2	1.7	0.03	0.03	4	9	0.0027	0.60	0.28	0.117
80	0.6	1.0E+13	0.5	151-151	176-176	421	0.109	0.013	461	2	2	10.7	0.24	0.17	25	79	0.0025	0.57	0.33	0.098
							0.104	0.010	692	3	5	18.0	0.34	0.28	38	126	0.0025	0.55	0.34	0.111
116	0.6	2.3E+13	0.5	187-187	255-300	368	0.117	0.010	461	3	1	20.1	0.47	0.41	51	121	0.0030	0.54	0.34	0.119
							0.154	0.013	692	6	6	35.9	0.65	0.67	74	195	0.0018	0.52	0.36	0.122
87	0.6	1.0E+14	0.5	185-194	303-658	431	0.039	0.001	461	0	1	56.3	1.61	2.30	189	329	0.0169	0.31	0.58	0.097
							0.066	0.003	692	2	1	94.2	2.11	3.72	241	526	0.0151	0.32	0.58	0.091
122	0.6	3.0E+14	0.5	200-237	332-560	458	0.044	0.002	461	1	1	207.	3.16	7.83	309	752	0.0017	0.27	0.65	0.081
							0.119	0.078	692	7	3	357.	3.74	12.82	369	1184	0.0011	0.32	0.61	0.065
85	0.6	1.0E+15	0.005	196-198	373->461	409	0.055	0.001	461	0	2	389.	9.25	24.6	910	1914	0.0022	0.26	0.68	0.058
118	0.6	1.0E+15	0.5	166-247	338-376	>461	0.078	0.005	461	3	0	392.	4.54	30.4	460	2446	0.0014	0.29	0.69	0.027
79	0.8	1.0E+13	0.5	146-150	169-169	192	0.205	0.032	461	12	11	12.7	0.22	0.19	32	65	0.0021	0.59	0.31	0.098
							0.249	0.047	692	19	17	22.0	0.30	0.30	38	115	0.0021	0.58	0.32	0.107
121	0.8	3.0E+13	0.005	576->692	>692	>692	0.	0.	461	0	0	11.	1.22	0.08	129	15	0.0041	0.25	0.35	0.391
							0.002	0.	692	0	0	22	1.77	0.17	182	32	0.0033	0.27	0.34	0.382
82	0.8	1.0E+14	0.005	379-443	682-	>692	0.003	0.	461	0	0	53.9	3.31	0.72	355	72	0.0024	0.21	0.50	0.288
							0.018	0.001	692	0	0	109.	4.38	1.45	465	159	0.0022	0.24	0.52	0.242
84	0.8	1.0E+15	0.005	136-136	230-345	245	0.132	0.007	461	8	11	418.	8.89	25.0	927	1938	0.0022	0.27	0.68	0.049
132	1.0	3.0E+11	0.5	137-137	152-152	248	0.131	0.034	461	3	4	0.4	0.01	0.01	2	1	0.0044	0.50	0.38	0.115
							0.152	0.131	692	5	5	0.6	0.01	0.01	2	2	0.0035	0.53	0.33	0.138
128	1.0	1.0E+12	0.5	145-169	179-184	231	0.153	0.098	461	8	10	1.2	0.03	0.02	3	7	0.0047	0.52	0.35	0.121
							0.195	0.058	692	11	14	2.1	0.04	0.03	3	13	0.0045	0.55	0.33	0.118
133	1.0	3.0E+12	0.5	145-145	158-160	184	0.216	0.099	461	21	30	4.1	0.07	0.06	8	23	0.0034	0.60	0.30	0.097
							0.278	0.070	692	30	39	7.0	0.10	0.09	12	33	0.0031	0.62	0.29	0.088
76	1.0	1.0E+13	0.25	141-141	171-171	365	0.065	0.005	461	3	1	10.6	0.34	0.09	37	39	0.0030	0.51	0.32	0.175
75	1.0	1.0E+13	0.5	119-137	153-153	187	0.289	0.058	461	20	31	13.6	0.22	0.18	29	68	0.0024	0.60	0.32	0.078
							0.315	0.074	692	45	58	22.8	0.30	0.31	39	120	0.0020	0.56	0.35	0.090
119	1.0	3.0E+13	0.005	431-603	>692	>692	0.001	0.	461	0	0	14.6	1.26	0.09	139	16	0.0038	0.30	0.33	0.367
							0.005	0.	692	0	0	28.4	1.76	0.18	187	36	0.0036	0.31	0.35	0.339
134	1.0	3.0E+13	0.5	104-138	168-172	255	0.278	0.040	461	27	19	35.4	0.61	0.57	61	162	0.0026	0.47	0.42	0.109
							0.281	0.049	692	49	47	59.0	0.83	0.93	86	258	0.0017	0.43	0.45	0.120
90	1.0	1.0E+14	0.005	282-329	>461	>461	0.009	0.	461	0	0	65.8	3.28	0.69	360	72	0.0026	0.23	0.50	0.275
129	1.0	1.0E+14	0.5	137-137	217-242	282	0.172	0.016	461	12	13	94.8	1.59	2.22	186	303	0.0014	0.31	0.58	0.101
							0.239	0.028	692	36	30	161.	2.10	3.68	228	513	0.0018	0.32	0.57	0.106

TABLE 1. Summary of simulations for fast ion beam traversing background plasma (Continued).

Run	Ekb/I	nN*fp	fb0	t11-t1f	t21-t2f	t10-t2f	tion	felmx	fe2mx	t	Nex	Nion	Nele	Nelia	Nelib	Ncea	Ncer	feE	feEkb	feEka
120	1.0	3.0E+14	0.005	218-223	417-474	465	0.063	0.002	461	1	0	215	6.29	4.60	652	391	0.0024	0.22	0.60	0.178
130	1.0	3.0E+14	0.5	184-194	288-415	322	0.102	0.003	461	3	2	233	3.16	7.33	345	590	0.0011	0.22	0.70	0.072
88	1.0	1.0E+15	0.005	67-83	159-231	208	0.277	0.029	461	73	56	455	8.95	0.0	927	0	0.0031	0.35	0.59	0.060
91	1.0	1.0E+15	0.005	106-133	245-293	317	0.139	0.008	461	11	8	430	8.89	27.1	924	0	0.0020	0.31	0.62	0.070
86	1.0	1.0E+15	0.005	106-106	211-279	368	0.182	0.011	461	17	10	428	9.09	24.2	908	1793	0.0015	0.25	0.69	0.058
131	1.0	1.0E+15	0.5	129-147	217-284	330	0.263	0.027	461	35	29	431	4.05	30.7	465	2454	0.0022	0.28	0.69	0.023
83	1.5	3.0E+13	0.005	285-457	>692	>692	0.003	0.	461	0	0	18.0	1.24	0.08	137	12	0.0032	0.27	0.36	0.364
78	1.5	1.0E+14	0.005	233-238	290-455	>461	0.052	0.003	461	0	0	34.9	1.75	0.19	192	20	0.0032	0.28	0.35	0.365
77	1.5	1.0E+15	0.005	77-81	163-184	194	0.310	0.039	461	83	62	461	9.08	25.7	921	2010	0.0021	0.23	0.72	0.051
42	2.0	1.0E+12	0.50	74-91	132-136	169	0.383	0.160	461	30	38	1.7	0.	0.	4	8	0.0035	0.53	0.36	0.099
127	2.0	1.0E+12	0.50	81-106	129-141	169	0.359	0.147	461	34	51	2.9	0.	0.	5	14	0.0035	0.55	0.36	0.090
14	2.0	3.0E+12	0.10	271-278	325-325	>458	0.030	0.005	458	0	0	2.2	0.	0.	0	0	0.0095	0.57	0.39	0.036
15	2.0	3.0E+12	0.25	135-141	170-176	250	0.206	0.044	500	5	10	4.3	0.	0.	0	0	0.0055	0.58	0.36	0.055
22	2.0	3.0E+12	0.25	145-149	167-171	224	0.204	0.043	500	9	11	4.3	0.	0.	0	0	0.0058	0.59	0.28	0.118
33	2.0	3.0E+12	0.50	85-98	136-148	160	0.447	0.173	461	84	96	5.4	0.	0.	10	19	0.0029	0.53	0.40	0.074
123	2.0	3.0E+12	0.50	72-79	129-129	142	0.479	0.171	692	123	148	9.1	0.	0.	14	43	0.0034	0.49	0.43	0.068
68	2.0	1.0E+13	0.005	>461	>461	>461	0.	0.	461	0	0	5.3	0.07	0.06	8	21	0.0030	0.52	0.38	0.098
20	2.0	1.0E+13	0.25	152-168	199-206	251	0.254	0.050	500	20	20	8.9	0.10	0.11	12	34	0.0026	0.49	0.41	0.098
34	2.0	1.0E+13	0.50	96-100	145-149	187	0.520	0.228	461	152	180	4.2	0.43	0.01	53	1	0.0055	0.26	0.37	0.362
37	2.0	1.0E+13	0.50	87-87	150-160	178	0.481	0.178	461	141	192	18.6	0.	0.	26	61	0.0033	0.50	0.45	0.042
51	2.0	1.0E+13	0.50	75-75	123-136	163	0.483	0.198	461	130	149	18.4	0.23	0.20	27	82	0.0031	0.45	0.44	0.116
70	2.0	3.0E+13	0.005	257-399	>461	>461	0.008	0.	461	0	0	21.6	1.26	0.08	134	11	0.0041	0.25	0.39	0.361
28	2.0	3.0E+13	0.10	161-224	293-346	>461	0.090	0.009	461	1	0	27.8	0.	0.	117	35	0.0041	0.45	0.52	0.026
18	2.0	3.0E+13	0.25	162-199	230-286	330	0.208	0.029	500	8	7	31.4	0.	0.	0	0	0.0048	0.61	0.36	0.033
26	2.0	3.0E+13	0.25	138-143	162-184	229	0.355	0.075	500	66	49	37.1	0.	0.	122	107	0.0033	0.46	0.51	0.028
32	2.0	3.0E+13	0.50	100-122	192-196	231	0.495	0.153	461	169	203	47.8	0.	0.	78	129	0.0035	0.40	0.57	0.027
							0.443	0.115	692	284	332	83.9	0.	0.	106	268	0.0027	0.27	0.64	0.038

TABLE 1. Summary of simulations for fast ion beam traversing background plasma (Continued).

Run	Ekb/I	nN*fp	fb0	t1i-t1f	t2i-t2f	t1on	felmx	fe2mx	t	Nex	Nion	Nele	Nelia	Nelib	Ncea	Ncer	fEf	fEke	fEkb	fEka
124	2.0	3.0E+13	0.50	81- 110	118- 118	192	0.474	0.150	461	121	151	43.8	0.59	0.63	63	166	0.0019	0.35	0.55	0.099
							0.427	0.106	692	202	254	73.5	0.82	1.06	88	264	0.0014	0.28	0.62	0.099
67	2.0	1.0E+14	0.005	165- 204	291- 327	451	0.076	0.008	461	0	1	95.2	3.26	0.70	358	60	0.0049	0.20	0.53	0.269
58	2.0	1.0E+14	0.25	148- 162	225- 239	324	0.196	0.002	461	18	15	110.	2.47	1.42	262	140	0.0022	0.23	0.58	0.192
35	2.0	1.0E+14	0.50	94- 98	156- 204	249	0.328	0.058	461	73	67	133.	0.	0.	186	250	0.0025	0.26	0.73	0.007
							0.384	0.079	692	225	242	230.	0.	0.	258	511	0.0020	0.28	0.74	0.013
36	2.0	1.0E+14	0.50	101- 118	175- 180	225	0.356	0.069	461	115	109	138.	0.	0.	188	285	0.0023	0.28	0.71	0.008
							0.369	0.066	692	257	237	236.	0.	0.	256	541	0.0013	0.22	0.76	0.011
52	2.0	1.0E+14	0.50	102- 112	176- 186	189	0.385	0.080	461	63	72	97.7	1.64	2.30	177	311	0.0022	0.26	0.65	0.095
							0.258	0.033	692	73	72	192.	3.27	2.52	351	269	0.0013	0.21	0.63	0.160
61	2.0	3.0E+14	0.25	106- 106	169- 176	213	0.281	0.028	461	98	106	375.	4.82	6.62	508	611	0.0011	0.19	0.71	0.097
							0.321	0.039	692	303	299	657.	5.65	12.51	594	1178	0.0017	0.19	0.74	0.065
41	2.0	3.0E+14	0.50	80- 84	146- 152	200	0.383	0.060	461	213	155	310.	0.	0.	403	808	0.0020	0.21	0.78	0.001
							0.375	0.059	692	414	357	528.	0.	0.	454	1408	0.0012	0.18	0.82	0.001
125	2.0	3.0E+14	0.50	93- 93	133- 170	204	0.305	0.046	461	79	76	202.	3.00	7.84	341	686	0.0013	0.18	0.75	0.067
							0.305	0.060	692	219	182	328.	3.48	13.69	389	1162	0.0022	0.19	0.75	0.054
69	2.0	1.0E+15	0.005	46- 46	143- 143	169	0.337	0.046	461	96	99	471.	8.92	24.0	913	1695	0.0017	0.18	0.76	0.059
9	2.0	1.0E+15	0.25	77- 79	116- 133	145	0.378	0.062	461	488	366	976.	6.87	32.4	703	3019	0.0019	0.20	0.78	0.024
							0.418	0.077	612	1244	1025	1525.	7.19	53.0	736	5748	0.0013	0.21	0.78	0.009
126	2.0	1.0E+15	0.50	69- 78	117- 124	158	0.368	0.058	461	235	225	496.	4.67	31.88	453	2597	0.0014	0.18	0.79	0.029
72	3.0	1.0E+13	0.005	448->461	>461	>461	0.001	0.	461	0	0	5.2	0.45	0.01	55	3	0.0052	0.25	0.38	0.359
30	3.0	1.0E+13	0.10	147- 178	239- 239	298	0.240	0.037	461	5	4	11.9	0.	0.	49	13	0.0082	0.62	0.35	0.028
							0.321	0.082	692	27	32	21.6	0.	0.	70	29	0.0054	0.57	0.38	0.036
73	3.0	3.0E+13	0.005	270- 270	451- 459	>461	0.045	0.001	461	1	0	23.9	1.21	0.09	131	6	0.0035	0.26	0.35	0.382
29	3.0	3.0E+13	0.10	164- 194	222- 239	273	0.275	0.057	461	18	23	34.6	0.	0.	117	35	0.0041	0.45	0.52	0.019
74	3.0	5.0E+13	0.005	172- 172	260- 360	331	0.13	0.015	461	4	1	49.2	1.91	0.19	198	26	0.0040	0.24	0.41	0.347
71	3.0	1.0E+14	0.005	132- 168	218- 276	305	0.245	0.032	461	21	27	113.	3.32	0.72	342	102	0.0022	0.21	0.51	0.278
31	3.0	1.0E+14	0.10	96- 102	130- 147	188	0.387	0.078	461	138	138	113.	0.	0.	346	176	0.0021	0.27	0.72	0.008
							0.430	0.108	692	376	390	202.	0.	0.	445	369	0.0016	0.20	0.79	0.007
89	3.0	1.0E+15	0.005	18- 20	59- 62	80	0.446	0.100	461	691	659	574.	9.1u	31.8	923	2871	0.0015	0.15	0.81	0.035

TABLE 1. Summary of simulations for fast ion beam traversing background plasma (Continued).

Notes:

1. All runs used a mass ratio of the positive ion to electron of 100.
2. The plasma simulation considers the beam ions and the ambient ions to have the same mass, but the ion-neutral collisions use a mass corresponding to  $O^+$  for the ambient ions and  $N_2^+$  for the beam ions.
3. The beam molecules all have a velocity of 8 km/s.
4. The initial thermal energy of electrons, ambient ions, and beam ions is 0.1, 0.1, and 0.01 eV, respectively.
5. If there is a zero entry in the column for ion-elastic collisions, or for charge exchange, that is an indication that the corresponding cross section has been set to zero.
6. All runs used 256 grid cells with a length chosen to maximize growth for mode one in the linear dispersion analysis. For the runs where fb0 is 0.005 and where there is charge exchange with ambient ions, the linear analysis used  $f = 0.05$  to allow for the growth of fb. Run 60 is a repeat of run 58 using the length calculated from fb0 = 0.5; this shows effects of different lengths.
7. All runs have the electron plasma frequency 2.26 times the electron gyrofrequency, which corresponds to an electron number density of  $10^5$  electrons/cm<sup>3</sup> and a magnetic field of 0.45 Gauss.
8. All times are given in an internal time unit. For a magnetic field of 0.45 Gauss, one unit is 2.16  $\mu$ s for  $O^+$ , 2.85  $\mu$ s for  $N_2^+$ , 2.95  $\mu$ s for  $NO^+$ , 3.58  $\mu$ s for  $CO_2^+$ , and 6.17  $\mu$ s for  $Xe^+$ . As a result of this time unit, the number densities (cm<sup>-3</sup>) of beam neutral molecules are multiplied by a mass-dependent factor  $F_p$ . The value of  $F_p$  is 84.3 for  $O^+$ , 112 for  $N_2^+$ , 116 for  $NO^+$ , 140 for  $CO_2^+$ , and 241 for  $Xe^+$ .
9. All runs initially have 1024 electrons and 1024 positive ions, with the positive ions distributed between beam ions and ambient ions.
10. Runs numbered 35 and smaller used a flattened angular distribution for electron-neutral elastic collisions. Runs 36 and 37 are repeats of runs 35 and 34.

TABLE 1. Summary of simulations for fast ion beam traversing background plasma (Concluded).

11. Runs numbered 20 and smaller used seven energy bins for the electron energies, rather than 11 bins as used for later runs. Run 22 is a repeat of run 15 to show the minor effects of this change.

Explanation of columns:

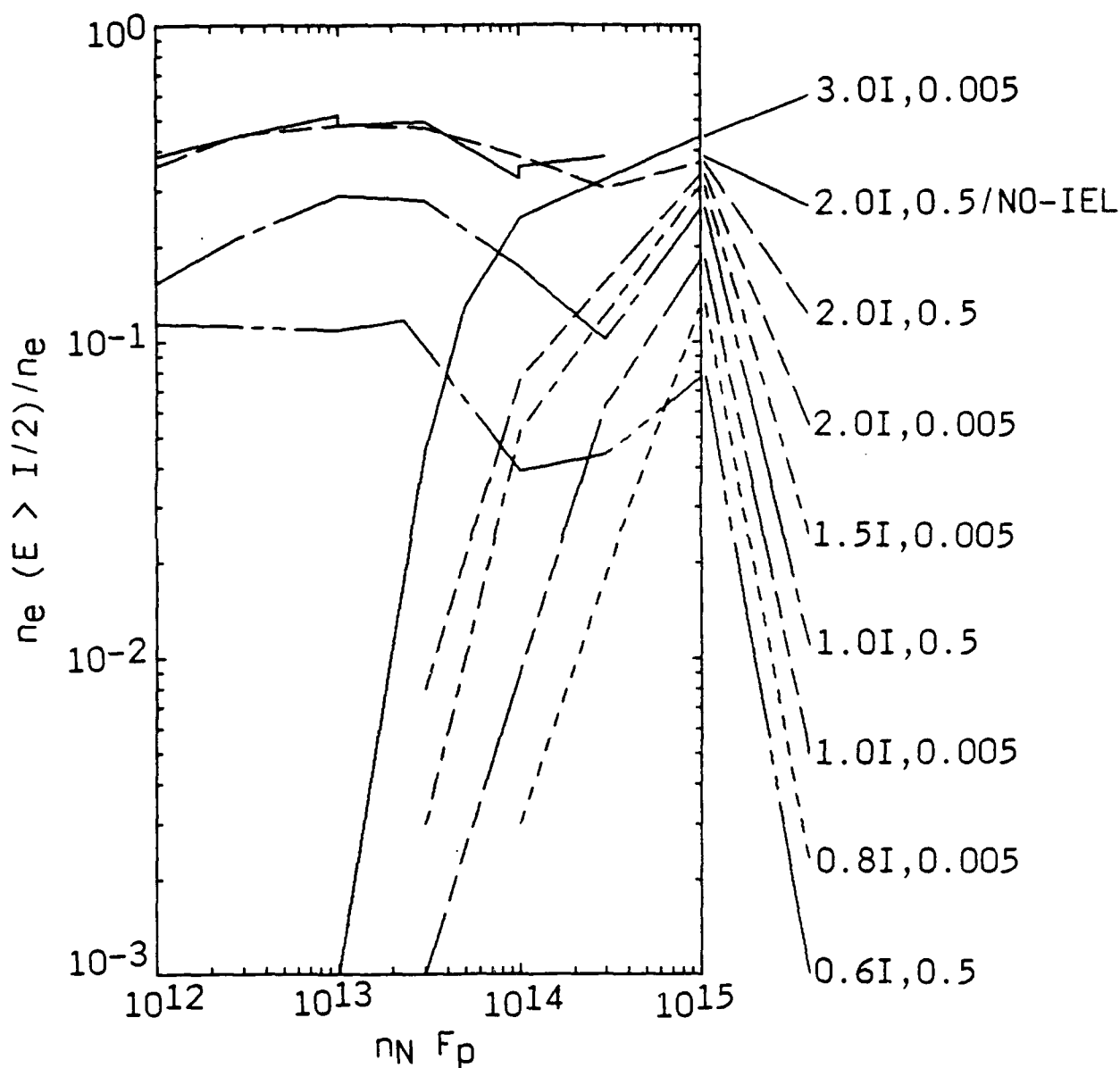
- Run - Run number.
- Ekb/I - Kinetic energy of beam ion divided by ionization potential I of beam molecule.
- nN\*Fp - Number density ( $\text{cm}^{-3}$ ) of beam neutral molecules multiplied by a mass-dependent factor Fp. At 0.45 Gauss, the value of Fp is 84.3 for  $\text{O}^+$ , 112 for  $\text{N}_2^+$ , 116 for  $\text{NO}^+$ , 140 for  $\text{CO}_2^+$ , and 241 for  $\text{Xe}^+$ .
- fb0 - Fraction of ions that are initially in the beam,  $\text{fb0} = n_b/n_e$ .
- t1i - Time before first one of electrons has more than I/2 of kinetic energy. See note 8.
- t1f - Time before at least one of electrons always has more than I/2 of kinetic energy. See note 8.
- t2i - Time before first one of electrons has more than I of kinetic energy. See note 8.
- t2f - Time before at least one of electrons always has more than I of kinetic energy. See note 8.
- tion - Time before first electron ionization. See note 8.
- felmx - Maximum fraction (in this time interval) of electrons with more than I/2 of kinetic energy.
- fe2mx - Maximum fraction (in this time interval) of electrons with more than I of kinetic energy.
- t - Time, for results. See note 8.
- Nex - Number of electronic excitation events. See note 9.
- Nion - Number of ionization events by electron collision. See note 9.
- Nele - (1/1000) times number of elastic electron-neutral collisions. See note 9.
- Nelia - (1/1000) times number of elastic ambient ion-neutral collisions. See note 9.
- Nelib - (1/1000) times number of elastic beam ion-neutral collisions. See note 9.
- Ncea - Number of charge exchange events with ambient ions. See note 9.
- Ncer - Number of resonant charge exchange events (with slow beam ions). See note 9.
- fEf - Fraction of total energy in the electric field.
- fEke - Fraction of total energy in the kinetic energy of the electrons.
- fEkb - Fraction of total energy in the kinetic energy of the beam ions.
- fEka - Fraction of total energy in the kinetic energy of the ambient ions.

neutral number density  $n_N$ , the initial kinetic energy of a beam ion  $E_{kb}$ , and the initial fraction of ions in the beam  $f_{b0}$ . Figures 17 and 18 are plots of  $f_{e1}$  and  $f_{e2}$  versus  $n_N$  for times around 1.2 ms. The plots are line segments connecting the points for the same  $E_{kb}$  and  $f_{b0}$  values. The lines for  $f_{b0} = 0.5$  show that more electrons are heated when  $E_{kb}$  is twice  $I$  than when  $E_{kb}/I$  is 0.6 or 1. Also, increasing  $n_N$  reduces the fraction heated, especially for Fig. 18, and there seems to be a minimum around  $1$  to  $3 \times 10^{12} \text{ cm}^{-3}$ . For the  $E_{kb}/I = 2$  case,  $n_N$  has less effect, but there still is a falloff of the hotter electrons in Fig. 18 as  $n_N$  increases. When we start with a weakly ionized beam with  $f_{b0} = 0.005$ , we find no heating until there are enough charge exchange collisions to increase the number of beam ions and to pump energy into the beam via resonant charge exchange collisions. Thus Figs. 17 and 18 show these cases to rise steeply with increasing  $n_N$ . They also show that the fraction of electrons heated increases as  $E_{kb}$  increases.

3.5.5.2 Rate of Electron Heating. The results on the fraction of electrons heated can be understood as the result of the different rates of heating the electrons for different neutral number density  $n_N$ , kinetic energy of the beam  $E_{kb}$ , and initial fraction of ions in the beam  $f_{b0}$ . Figures 19 and 20 are plots of the reciprocal of the time (in internal units) to heat the first 0.001 of the electrons to a kinetic energy of  $I/2$  or  $I$ , respectively. The plots are line segments connecting the points for the same  $E_{kb}$  and  $f_{b0}$  values. The lines for  $f_{b0} = 0.5$  show that more electrons are heated faster when  $E_{kb}/I$  is two than when  $E_{kb}/I$  is 0.6. Also, increasing  $n_N$  has only a modest effect when  $f_{b0}$  is 0.5; it decreases the heating rate to reach an energy of  $I$  for the  $E_{kb}/I = 0.6$  case. When we start with a weakly ionized beam with  $f_{b0} = 0.005$ , we find that the heating rate increases with  $n_N$ , which increases the rate of charge exchange reactions. Figures 19 and 20 show also that the heating rate increases as  $E_{kb}$  increases. Note that the values at 0.00204 and 0.00145 represent upper limits.

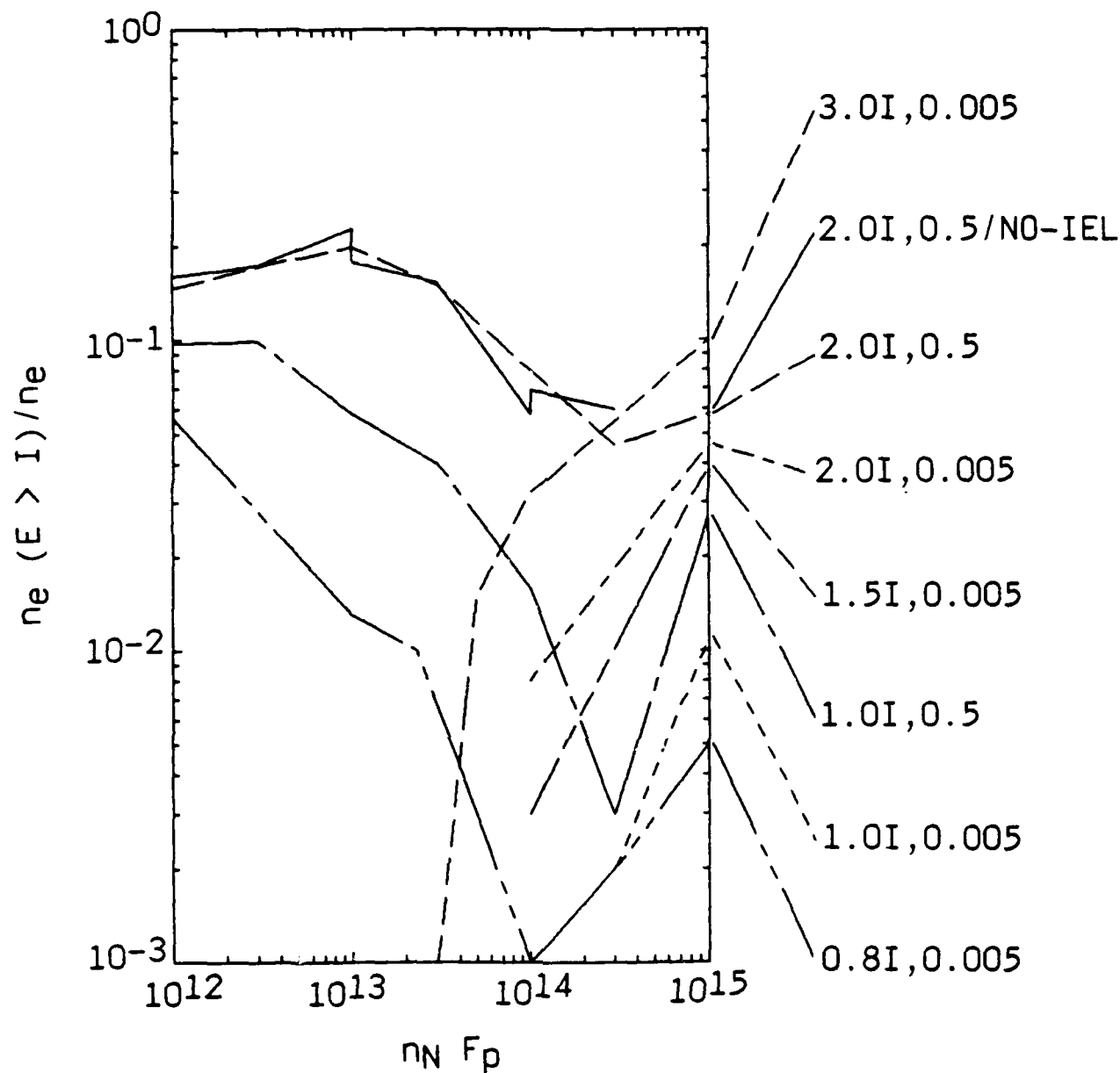
3.5.5.3 Disposition of the Energy of the Fast Ion Beam. If we consider the case where we have an initial fraction of ions in the fast ion beam and we do





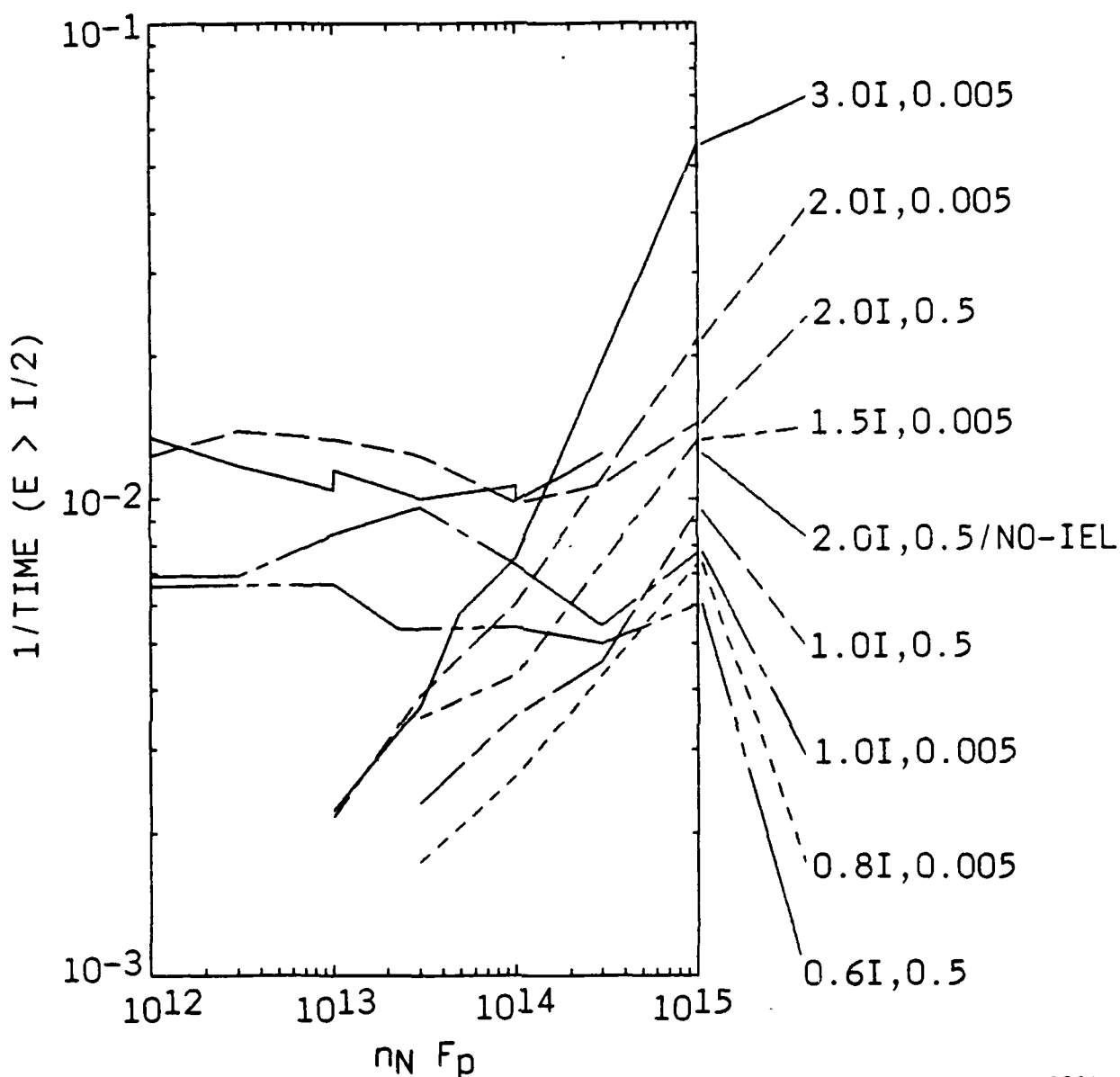
A-6933

Figure 17. Maximum fraction of electrons heated to an energy of  $I/2$  during the first 461 time units as a function of the number density of neutral molecules. The lines are labeled with the energy of the beam ions  $E_{kb}$  and with the initial fraction of ions in the beam  $f_{b0}$ . The solid line labeled NO-IEL represents runs where there are no elastic collisions of the ions and neutrals. Note 8 to Table 1 explains the mass-dependent values of the time unit, which is  $2.85 \mu s$  for  $N_2^+$ , and  $F_p$ , which is 112 for  $N_2^+$  when  $n_N$  is in  $cm^{-3}$ .



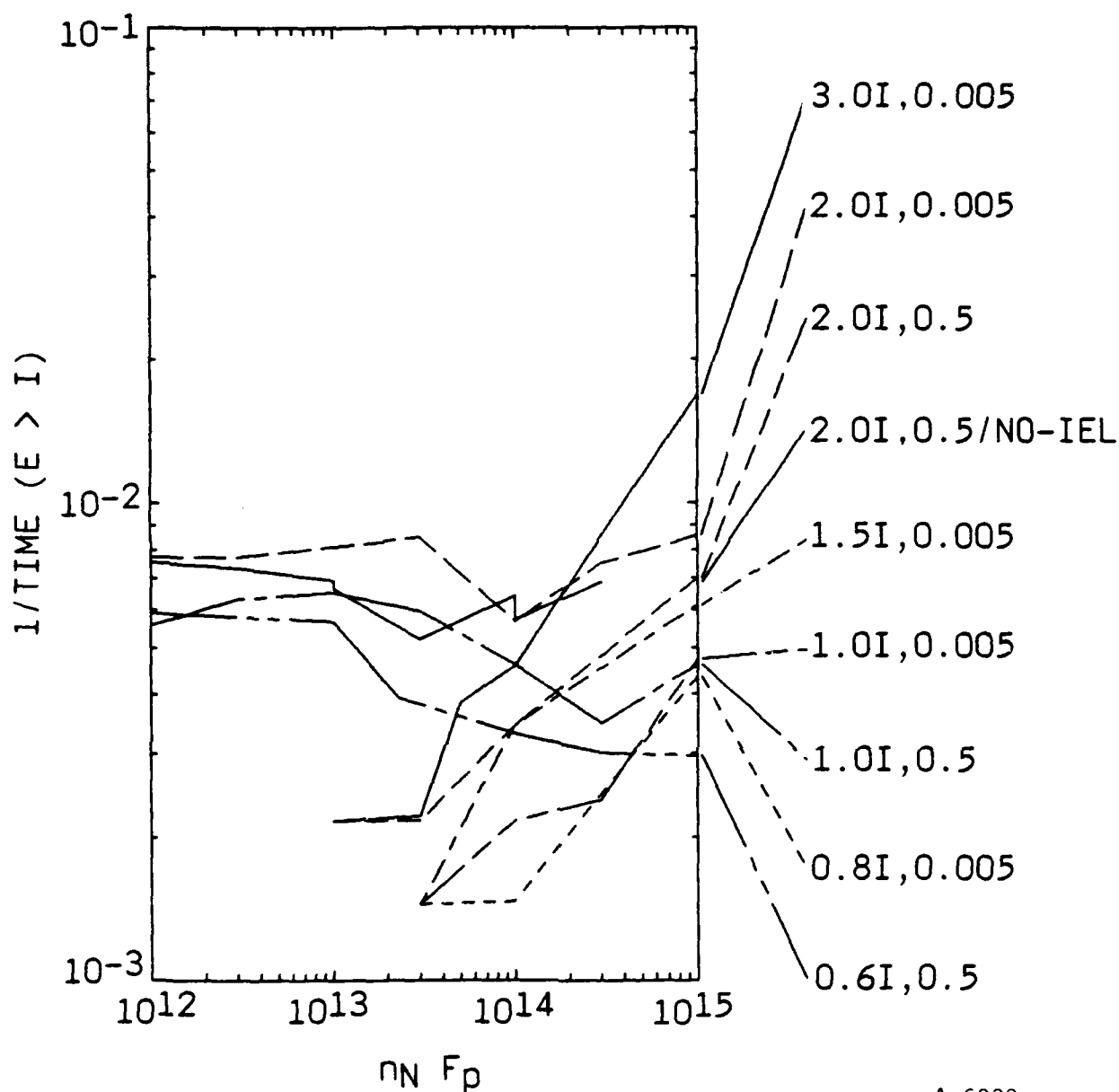
A-5932

Figure 18. Maximum fraction of electrons heated to an energy of  $I$  during the the first 461 time units as a function of the number density of neutral molecules. The lines are labeled with the energy of the beam ions  $E_{kb}$  and with the initial fraction of ions in the beam  $f_{b0}$ . The solid line labeled  $NO-IEL$  represents runs where there are no elastic collisions of the ions and neutrals. Note 8 to Table 1 explains the mass-dependent values of the time unit, which is  $2.85 \mu s$  for  $N_2^+$ , and  $F_p$ , which is 112 for  $N_2^+$  when  $n_N$  is in  $cm^{-3}$ .



A-6931

Figure 19. Rate of heating 0.001 of the electrons to an energy of  $I/2$  as a function of the number density of neutral molecules. The lines are labeled with the energy of the beam ions  $E_{kb}$  and with the initial fraction of ions and neutrals. Note 8 to Table 1 explains in the beam  $f_{b0}$ . The solid line labeled NO-IEL represents runs where there are no elastic collisions of the ions and neutrals. Note 8 to Table 1 explains the time unit, which is  $2.85 \mu s$  for  $N_2^+$ , and  $F_p$ , which is 112 for  $N_2^+$  when  $n_N$  is in  $cm^{-3}$ .

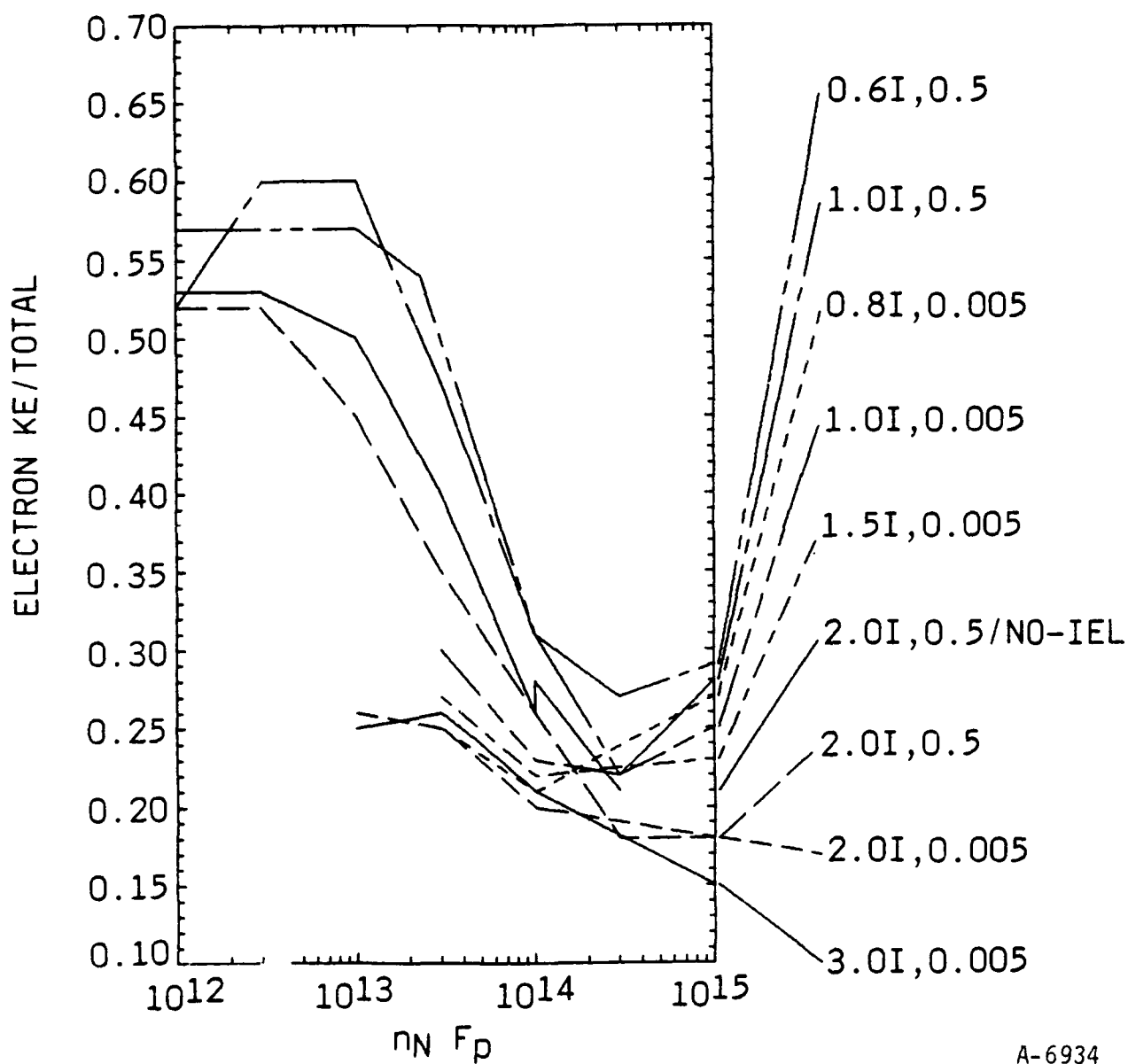


A-6930

Figure 20. Rate of heating 0.001 of the electrons to an energy of  $I$  as a function of the number density of neutral molecules. The lines are labeled with the energy of the beam ions  $E_{kb}$  and with the initial fraction of ions in the beam  $f_{b0}$ . The solid line labeled NO-IEL represents runs where there are no elastic collisions of the ions and neutrals. Note 8 to Table 1 explains the mass-dependent values of the time unit, which is  $2.85 \mu s$  for  $N_2^+$ , and  $F_p$ , which is 112 for  $N_2^+$  when  $n_N$  is in  $cm^{-3}$ .

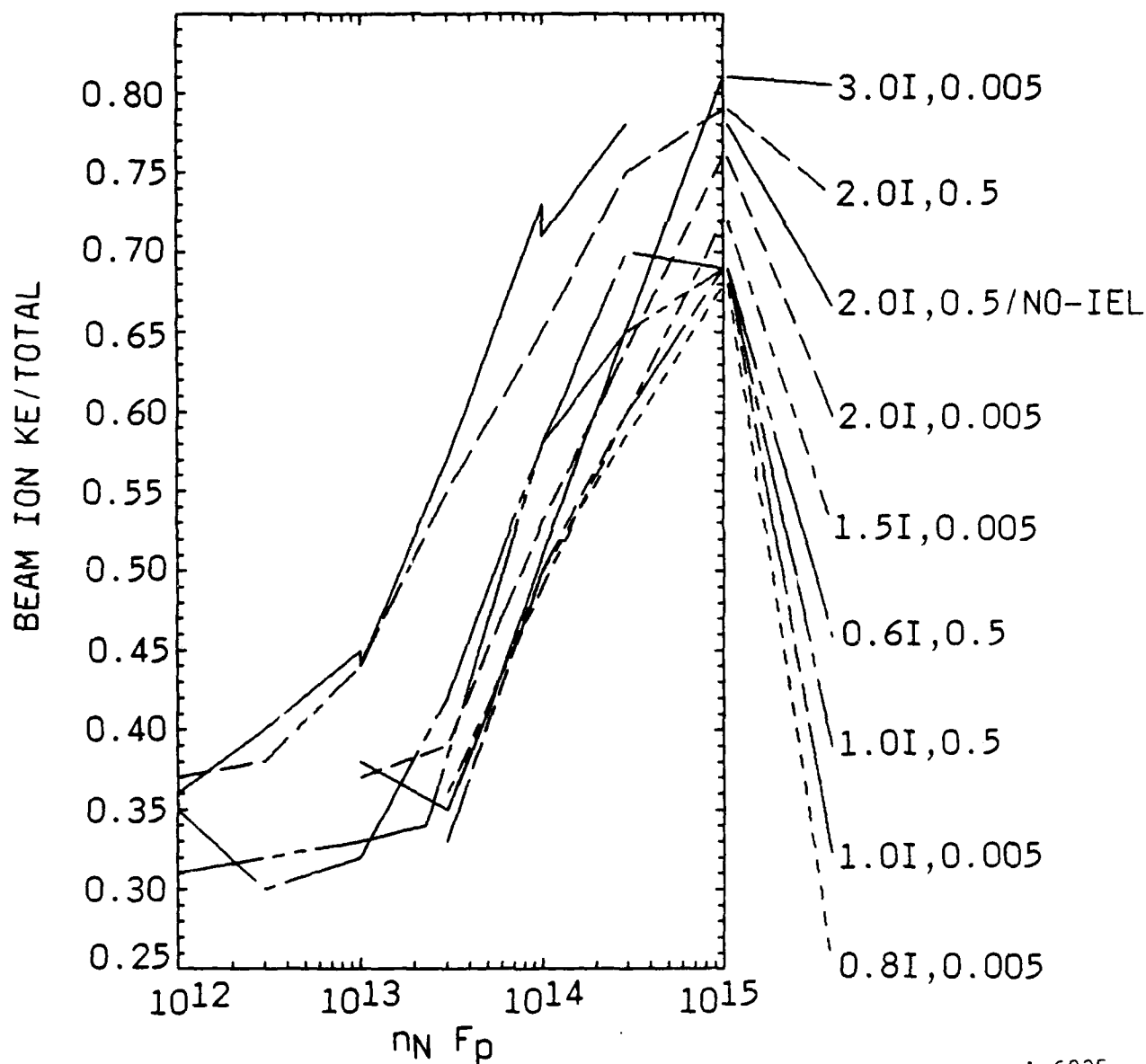
not allow charge exchange or ion-neutral elastic collisions, then we can determine the disposition of the energy that was initially present as kinetic energy of the fast ion beam. This energy is divided between the field energy and the kinetic energy of (1) the electrons  $E_e$ , (2) the ambient ions  $E_{Ka}$ , and (3) the beam ions  $E_{Kb}$ . We choose the angle between the magnetic field and the velocity vector of the beam ions to maximize the electron heating in the linear dispersion analysis. At this angle approximately 52 to 60 percent of the initial kinetic energy of the beam ions is transferred to  $E_e$  and 4 to 12 percent to  $E_a$ . Thus  $\eta$  is 0.52 to 0.6 in this simulation, lower than the 0.8 estimated by Mobius and coworkers (1987), but consistent with the limit of  $2/3$  given by Galeev (1981) and with the results of other simulations (e.g., McBride, et al, 1972; Machida and Goertz, 1986).

Figures 21 through 23 shows the fraction of the total energy in the kinetic energy of the electrons, the beam ions, and the ambient ions, respectively, all evaluated at a time near 1.2 ms (461 internal units). At low pressures the fraction in electron kinetic energy is approximately independent of  $n_N$ . Here it is given by  $\eta$ . At higher pressures energy is transferred to the beam ions faster than the ions transfer energy to the electrons. Here, the fraction of energy in the beam ions increases and the fraction in the electrons decreases, as shown in Figs. 21 and 22. Note that the larger values of  $E_{Kb}/I$  give a larger fraction in the energy of the beam. This is the result of the resonant charge exchange energy feeding energy into the beam faster than the energy is transferred to the electrons. That is, the larger  $E_{Kb}/I$  beams heat electrons faster (as shown in Figs. 19 and 20). As a result the beam ions are slowed faster, which gives more resonant charge exchange collisions. The figures are not adjusted for the changing proportion of the ions that are in the beam. This explains why the  $f_{b0} = 0.5$  cases are high for their value of  $E_{Kb}/I$ . Also, this explains the decrease in the ambient ion energy fraction as the number of ambient ions decreases for  $n_N$  greater than  $3 \times 10^{11} \text{ cm}^{-3}$ .



A-6934

Figure 21. Fraction of the total energy in the electron kinetic energy after 461 time units as a function of the number density of neutral molecules. The lines are labeled with the initial energy of the beam ions  $E_{kb}$  and with the initial fraction of ions in the beam  $f_{b0}$ . The solid line labeled NO-IEL represents runs where there are no elastic collisions of the ions and neutrals. Note 8 to Table 1 explains the mass-dependent values of the time unit, which is  $2.85 \mu s$  for  $N_2^+$ , and  $F_p$ , which is 112 for  $N_2^+$  when  $n_N$  is in  $cm^{-3}$ .



A-6935

Figure 22. Fraction of the total energy in the beam ion kinetic energy after 461 time units as a function of the number density of neutral molecules. The lines are labeled with the initial energy of the beam ions  $E_{kb}$  and with the initial fraction of ions in the beam  $f_{b0}$ . The solid line labeled NO-IEL represents runs where there are no elastic collisions of the ions and neutrals. Note 8 to Table 1 explains the mass-dependent values of the time unit, which is  $2.85 \mu\text{s}$  for  $\text{N}_2^+$ , and  $F_p$ , which is 112 for  $\text{N}_2^+$  when  $n_N$  is in  $\text{cm}^{-3}$ .

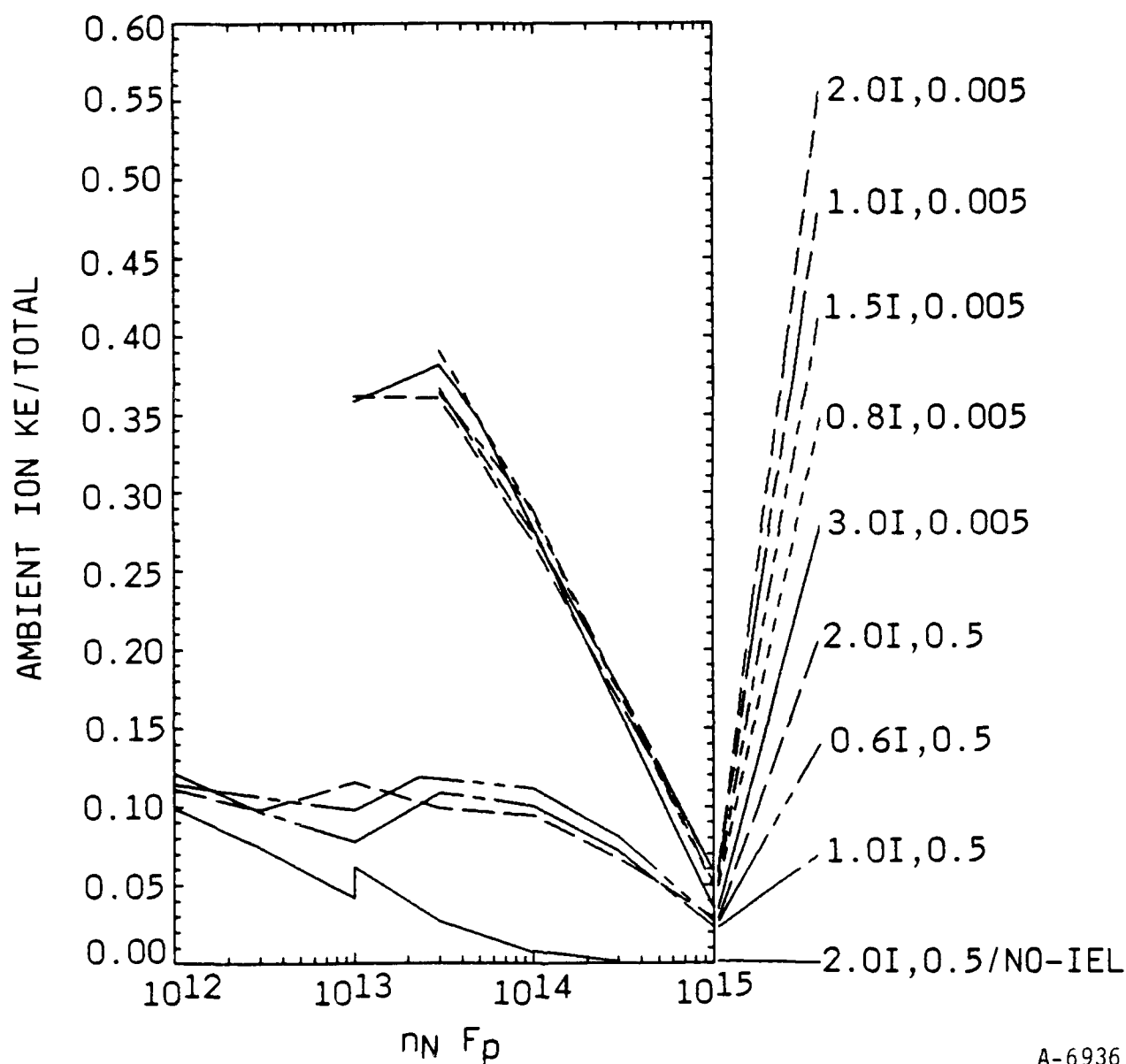


Figure 23. Fraction of the total energy in the ambient ion kinetic energy after 461 time units as a function of the number density of neutral molecules. The lines are labeled with the energy of the beam ions  $E_{kb}$  and with the initial fraction of ions in the beam  $f_{b0}$ . The solid line labeled NO-IEL represents runs where there are no elastic collisions of the ions and neutrals. Note 8 to Table 1 explains the mass-dependent values of the time unit, which is  $2.85 \mu\text{s}$  for  $\text{N}_2^+$ , and  $F_p$ , which is 112 for  $\text{N}_2^+$  when  $n_N$  is in  $\text{cm}^{-3}$ .



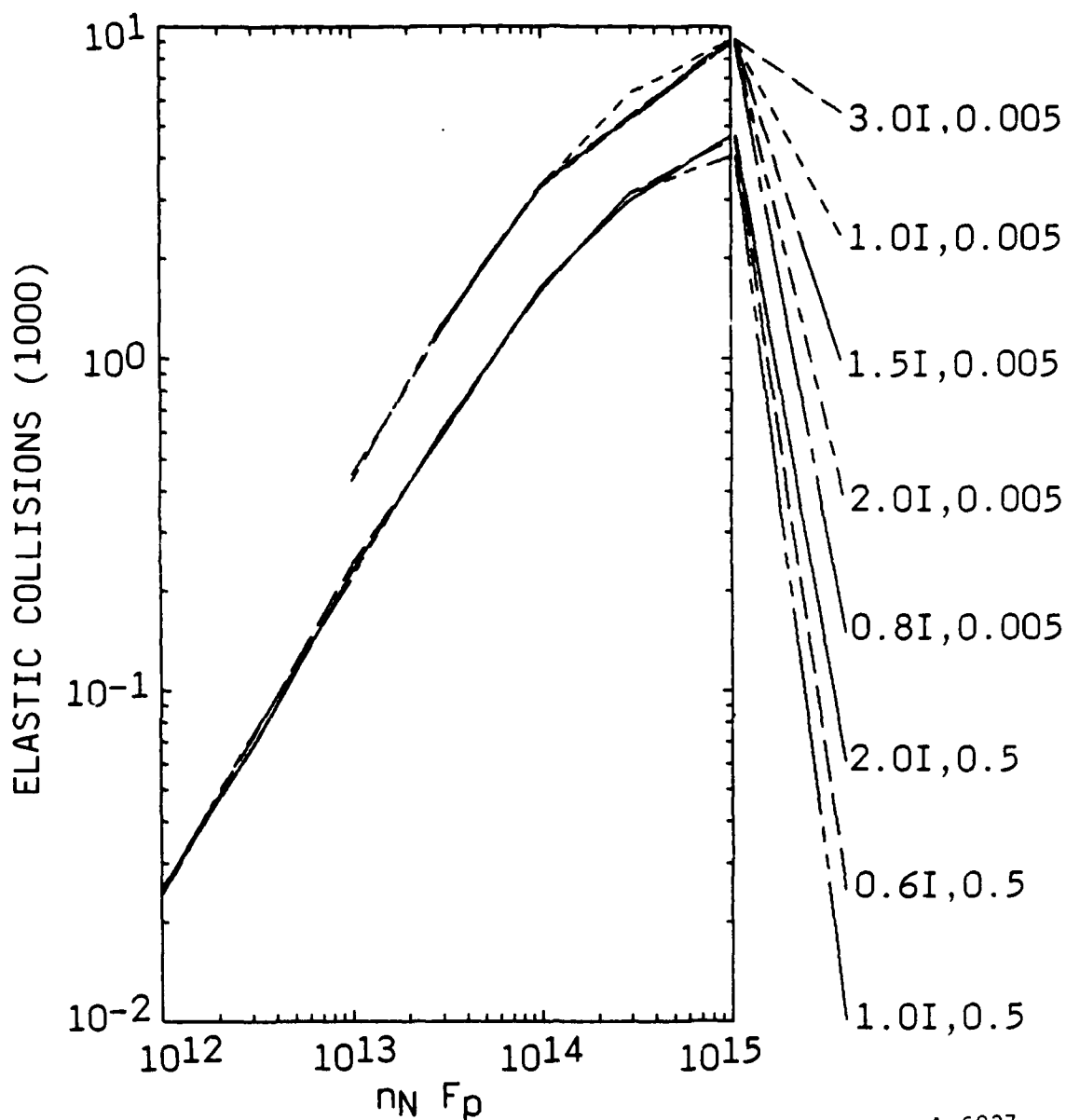
For the case where  $E_{kb}/I$  is two, the fraction of energy going into the field energy decreased from 0.029 to 0.011 as the number density increased from about  $3 \times 10^{10}$  to  $3 \times 10^{11}/\text{cm}^3$ , when the fraction of ions that are in the beam is 0.25. Presumably this decrease in the fraction of the energy that goes into the electric field is the result of elastic collisions of the ions and the electrons with the neutral molecules, which scatter the charged species and reduce the field build-up. However, the field energy is rather noisy, and the pressure dependence is not always so noticeable. However, the trend is for the fraction of the energy in the field to decrease as the pressure increases.

3.5.5.4 Effects of Ion-Neutral Elastic Collisions. Some simulations did not include the effects of ion-neutral elastic collisions. The main effects of these collisions is to increase the thermal energy of the ambient ions and to reduce the amount of CIV ionization. The curves labeled NO-IEL show the results when no ion-neutral elastic collisions are included. Figure 23 shows the greatest change as the fraction of energy in the ambient ions is much greater when the ion elastic collisions are included. The increase in ambient ion thermal energy is to be expected, as we are colliding fast neutral molecules with slow ambient ions. Eventually the increase in the thermal velocity of the ambient ions  $v_{aith}$  could reduce the electron heating, as the velocity of the beam ions  $v_{bi} > v_{aith}$  is the criterion for the modified two-stream instability (McBride, et al., 1972). However, our simulations did not heat the ambient ions this much. We did observe that the electron ionization was some 30 percent less when the elastic collisions were included, while the field energy was nearly the same, but Table 1 shows that this effect varies with  $n_N$ .

3.5.5.5 Molecular Effects of Increased Neutral Density. In this section we discuss the effects of increased  $n_N$  on the number of electron ionization collisions and electron excitation collisions, as well as the effects on the various types of elastic collisions and charge exchange collisions. These effects can be understood by using the definitions of the various collision

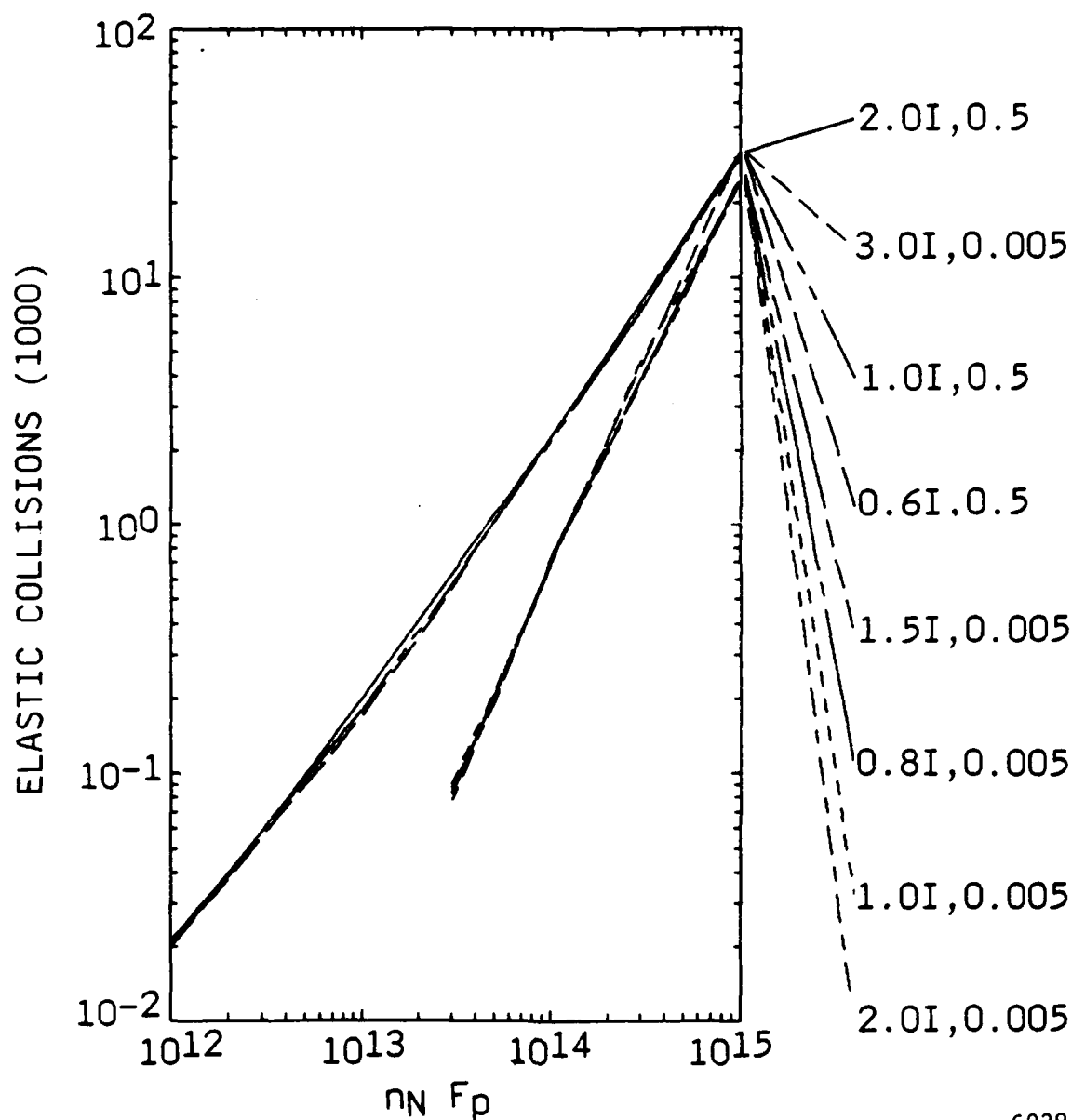
frequencies given in Eq. (102). Figures 24 through 28 show plots of the results for the first 1.2 ms. Recall that there initially are 1024 electrons and that the ions are distributed initially with a fraction  $f_{b0}$  in the beam. Thus the number of ion-neutral elastic collisions of ambient ions, plotted in Fig. 24, gives two curves, one for each  $f_{b0}$ . Also note that the curvature in this plot and in Fig. 27 results from the depletion of the ambient ions. In Fig. 27 there are fewer charge exchange collisions of the ambient ions after the number of such collisions begins to approach the initial number of ambient ions, which is 512 when  $f_{b0}$  is 0.5 and 1019 when  $f_{b0}$  is 0.005. At lower values of  $n_N$ , the number of ambient ion collisions in Figs. 24 and 27 is approximately twice as great for  $f_{b0} = 0.005$ , as there are approximately twice as many ambient ions as for  $f_{b0} = 0.5$ . In Fig. 25, the elastic collisions of the beam ions continue to grow; the slope of the  $f_{b0} = 0.5$  data is less than that for the  $f_{b0} = 0.005$  data because the relative change in the number of beam ions is less. There are some effects of changing  $E_{kb}/I$ . Figure 28 shows that the  $E_{kb}/I = 3$  data are better at slowing the ions so that there are more resonant charge exchange collisions, and even a few more ion-elastic collisions as shown in Fig. 25. Figure 26 shows that the number of electron elastic collisions does depend on the electron heating. Thus at larger values of  $f_{b0}$  or  $E_{kb}/I$ , the electrons are more energetic, so that a larger fraction of them have energies near the maximum in the elastic cross section near 2 eV.

**3.5.5.6 Requirement for a Minimum Density of Beam Ions.** The discussion of the CIV process often assumes that the process can develop from a few initial seed ions, with no mention of any requirement of a minimum number of seed ions. Further consideration shows that CIV ionization will not occur at a reasonable rate unless there is a sufficient number density of beam ions so that the electrons are heated enough to produce a reasonable fraction with an energy exceeding the ionization potential. That is, electron heating can occur without a threshold, but, if there is only a small number of beam ions, then the energy supplied to the electrons by the slowing of the fast ions will be too small to raise the energy of a sufficient number of electrons to produce any ionization events. We can understand this minimum fraction of



A-6937

Figure 24. Number of elastic collisions of the ambient ions with neutrals during 461 time units as a function of the number density of neutral molecules. The lines are labeled with the energy of the beam ions  $E_{kb}$  and with the initial fraction of ions in the beam  $f_{b0}$ . The solid line labeled NO-IEL represents runs where there are no elastic collisions of the ions and neutrals. Note 8 to Table 1 explains the mass-dependent values of the time unit, which is  $2.85 \mu s$  for  $N_2^+$ , and  $F_p$ , which is 112 for  $N_2^+$  when  $n_N$  is in  $cm^{-3}$ . The initial number of ambient ions is  $1024(1-f_{b0})$ .



a-6938

Figure 25. Number of elastic collisions of the beam ions with neutrals during 461 time units as a function of the number density of neutral molecules. The lines are labeled with the energy of the beam ions  $E_{kb}$  and with the initial fraction of ions in the beam  $f_{b0}$ . The solid line labeled NO-IEL represents runs where there are no elastic collisions of the ions and neutrals. Note 8 to Table 1 explains the mass-dependent values of the time unit, which is  $2.85 \mu\text{s}$  for  $\text{N}_2^+$ , and  $F_p$ , which is 112 for  $\text{N}_2^+$  when  $n_N$  is in  $\text{cm}^{-3}$ . The initial number of ambient ions is 1024 ( $f_{b0}$ ).

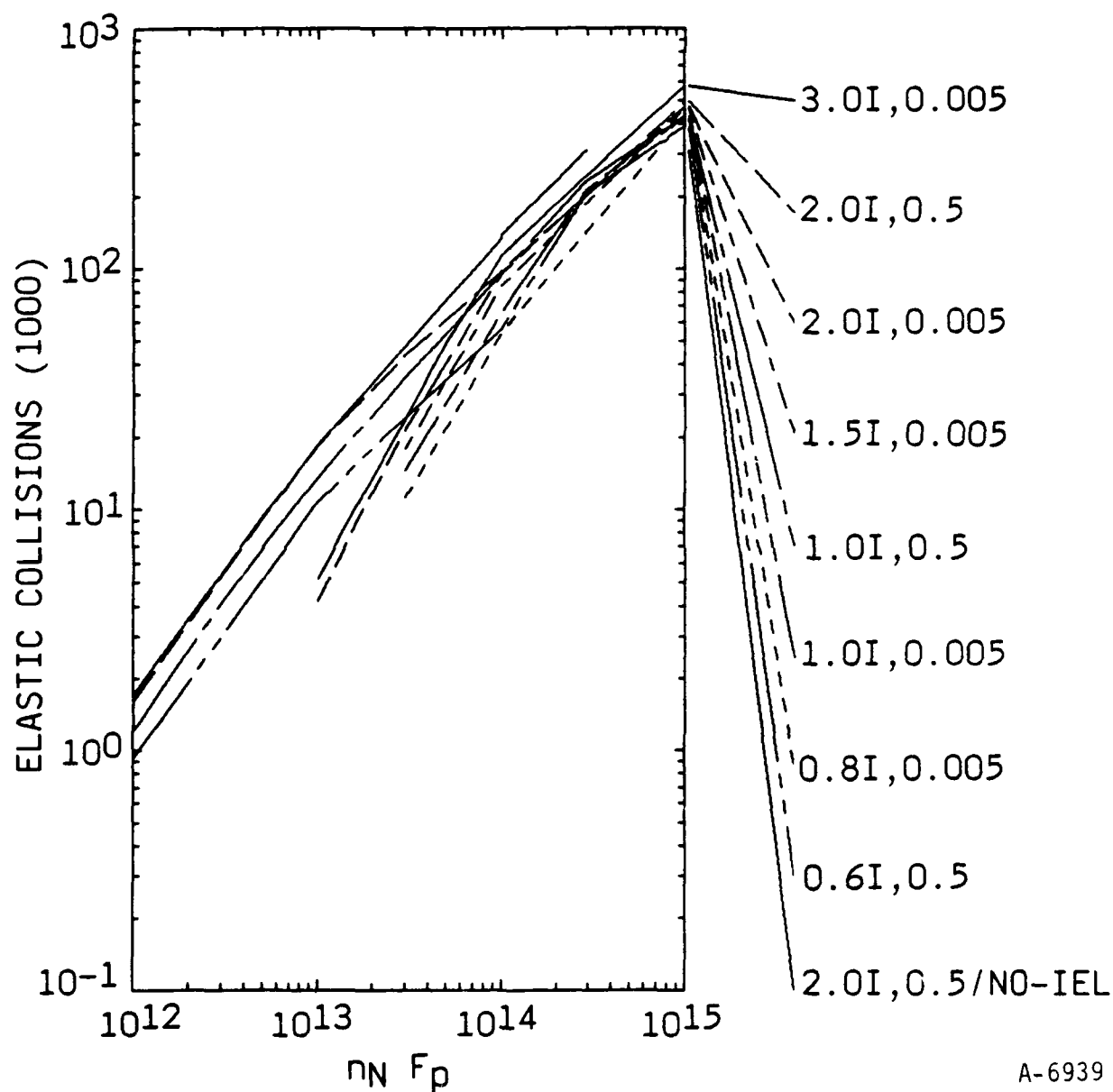
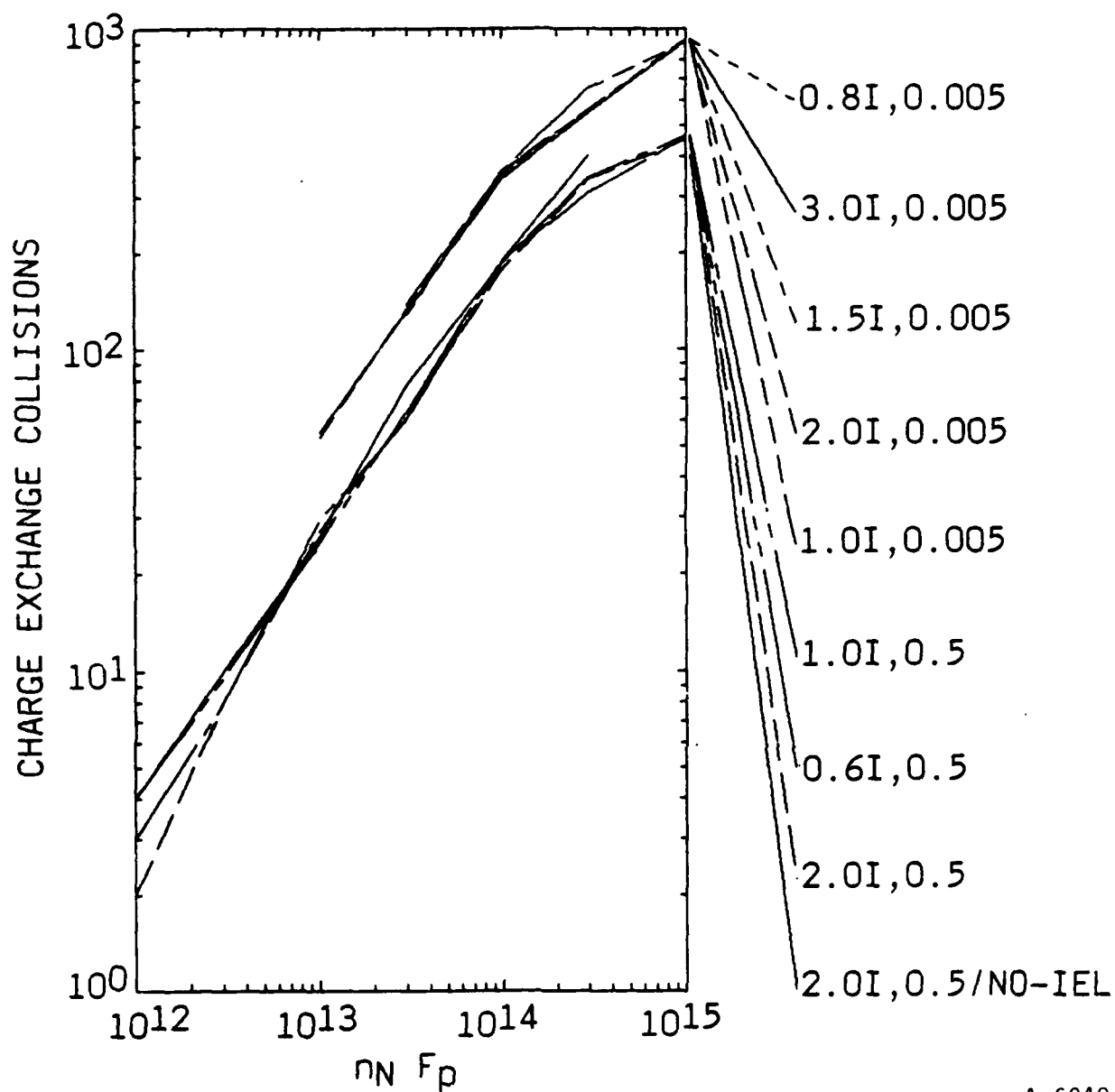
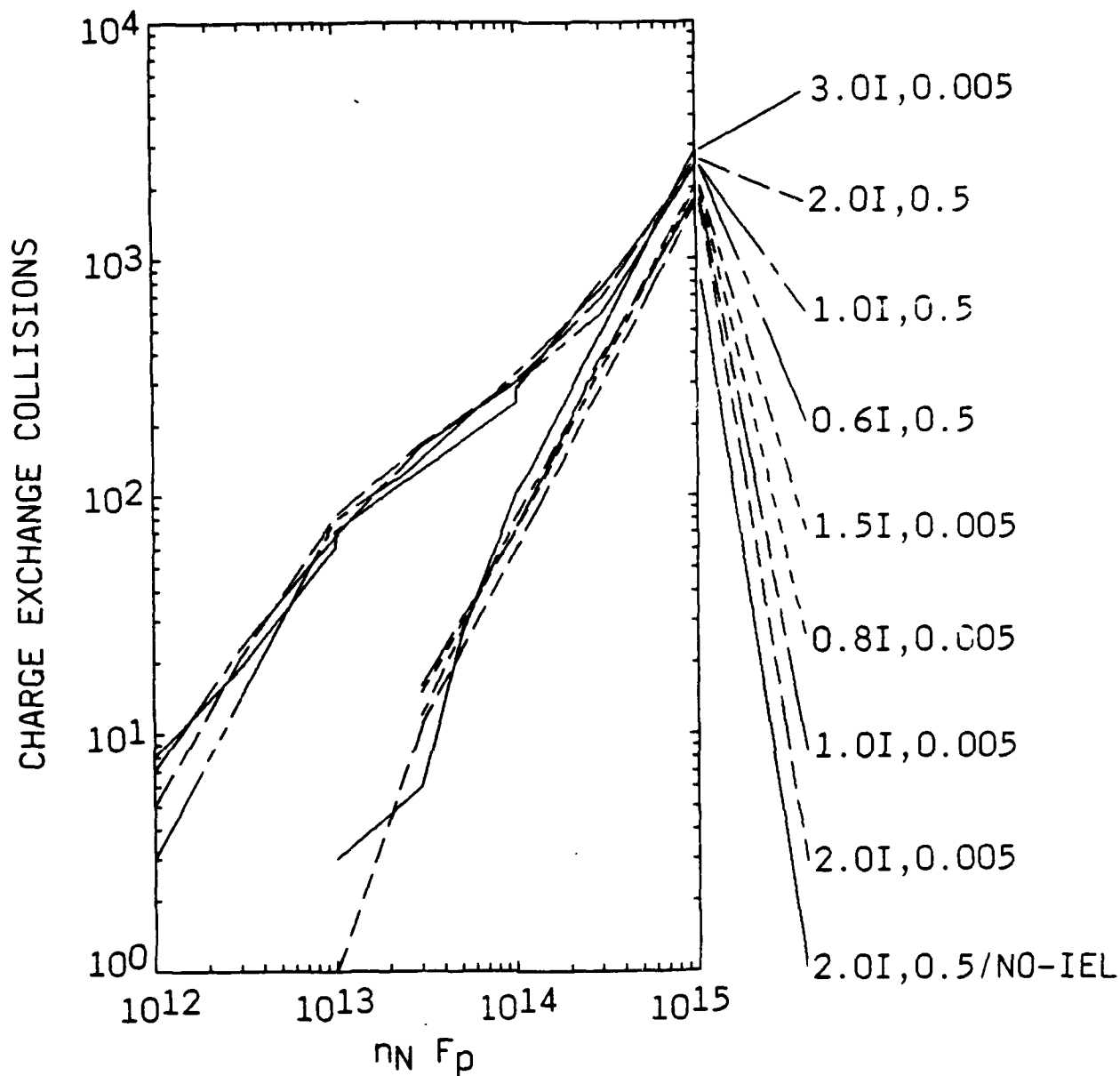


Figure 26. Number of elastic collisions of the electrons with neutrals during 461 time units as a function of the number density of neutral molecules. The lines are labeled with the energy of the beam ions  $E_{kb}$  and with the initial fraction of ions in the beam  $f_{b0}$ . The solid line labeled NO-IEL represents runs where there are no elastic collisions of the ions and neutrals. Note 8 to Table 1 explains the mass-dependent values of the time unit, which is 2.85  $\mu s$  for  $N_2^+$ , and  $F_p$ , which is 112 for  $N_2^+$  when  $n_N$  is in  $cm^{-3}$ . The initial number of electrons is 1024.



A-6940

Figure 27. Number of charge exchange collisions of ambient ions with neutrals during 461 time units as a function of the number density of neutral molecules. The lines are labeled with the energy of the beam ions  $E_{kb}$  and with the initial fraction of ions in the beam  $f_{b0}$ . The solid line labeled NO-IEL represents runs where there are no elastic collisions of the ions and neutrals. Note 8 to Table 1 explains the mass-dependent values of the time unit, which is 2.85  $\mu\text{s}$  for  $\text{N}_2^+$ , and  $F_p$ , which is 112 for  $\text{N}_2^+$  when  $n_N$  is in  $\text{cm}^{-3}$ . The initial number of ambient ions is 1024  $(1-f_{b0})$ .



A-6941

Figure 28. Number of charge exchange collisions of beam ions with neutrals during 461 time units as a function of the number density of neutral molecules. The lines are labeled with the energy of the beam ions  $E_{kb}$  and with the initial fraction of ions in the beam  $f_{b0}$ . The solid line labeled NO-IEL represents runs where there are no elastic collisions of the ions and neutrals. Note 8 to Table 1 explains the mass-dependent values of the time unit, which is  $2.85 \mu s$  for  $N_2^+$ , and  $F_p$ , which is 112 for  $N_2^+$  when  $n_N$  is in  $cm^{-3}$ . The initial number of beam ions is 1024 ( $f_{b0}$ ).

the ions that are beam ions, by considering that the electron heating from  $n_b$  fast ions that initially have a kinetic energy of  $E_{Kb}$  ( $= m_b v_b^2/2$ ) will be

$$\Delta E_e = \eta n_b E_{Kb} \quad . \quad (105)$$

Thus the average increase in energy is  $\eta n_b E_{Kb}/(n_e)_{\text{final}}$ . Electrons must be energized to values above  $I$  before ionization can occur. Thus we can assume that the average increase in energy must exceed some fraction  $h$  of  $I$ , and when the CIV process is in the early stages with  $(n_e)_{\text{final}} \approx n_e$  then

$$\eta n_b E_{Kb}/n_e > hI \quad , \quad (106)$$

or

$$f = n_b/n_e > hI/(\eta E_{Kb}) \quad . \quad (107)$$

This minimum fraction is thus a function of  $h$ , and the value of  $h$  will depend on the velocity distribution of the electrons. If this distribution is Maxwellian, then  $h \sim 0.20$  is a reasonable estimate. The electron distribution is expected to have a pronounced tail (Papadopoulos, 1984). When the drift velocity of the beam ions is small ( $v_b < 3 v_{ia}$ ), then the electrons will form a tail (Tanaka and Papadopoulos, 1983). However our beam ions are faster than this so our electron distribution may not have as pronounced a tail. If there is a significant tail in our simulations, then  $h$  will be smaller.

We see that either making the kinetic energy of the beam greater or increasing the efficiency  $\eta$ , gives the condition that the  $n_b / n_e$  ratio can be smaller. In our simulations with no charge exchange collisions (and also with no ion-neutral elastic collisions), then  $f_{\text{min}} \approx 0.1$  when  $E_{Kb}$  was  $2I$  and  $\eta \approx 0.6$ . This implies that  $h \approx 0.12$  for our simulation for a low gas density around  $10^{10}/\text{cm}^3$ .

The importance of this effect is that there can be growth of a plasma instability, which is energizing electrons, but the tail of the distribution must have electrons with energies above  $I$  before additional ionization can



occur. Furthermore, the increase of electron energy will be at least partially distributed among the bulk of the electron distribution, which leads to a requirement of  $f_{\min}$  for CIV ionization.

3.5.5.7 Effects of Kinetic Energy of Fast Beam Ions. When the kinetic energy of the fast beam ions is increased, the electron heating increases. As discussed above, the increased  $E_{kb}$  of the fast ions allows the electrons to be heated enough to produce further ionization with a smaller fraction of beam ions than would be required if the  $E_{kb}$  were smaller. Basically the increased energy in the fast ion beam produced from the fast neutrals transfers more energy to the electrons, which makes a larger fraction of the electrons have energies above  $I$ . Figures 17 and 18 give results from a series of runs where  $f_{b0}$ , the fraction of ions in the beam initially, was either 0.005 or 0.5, the ratio of the initial kinetic energy of the beam ions to the ionization potential varied from 0.6 to 3, and the number density varied from  $10^{10}$  to  $10^{13}$  per  $\text{cm}^3$ . Figures 19 and 20 show the rates to heat 0.001 of the electrons to an energy of  $I/2$  or  $I$ , respectively. Table 1 has the time to increase the electron density by a fraction of 0.001.

3.5.5.8 Importance of Charge Exchange as an Energy Source for CIV. Note that Table 1 and Figs. 17 through 20 show that it is possible to heat electrons to the ionization energy even when the kinetic energy of the beam molecules is less than the ionization energy. Furthermore, it is even possible to produce an increase in the electron density when this is true. The present simulations have not followed the increase over a long period, but we can anticipate that there is a greater increase than would be allowed if the only energy source is the kinetic energy of the beam ions that are present initially or formed from ionization by fast electrons. The reason for this greater increase is that the resonant charge exchange collisions are an additional source of energy. That is, if each beam ion transfers about  $3/5$  of its kinetic energy to the electrons we might expect that there would be an energy threshold of  $(5/3) I$  (not to mention the fact that there are also losses from energy transferred to excited states that decay before they were

ionized). However, there are two sources of additional energy: charge exchange with ambient ions and resonant charge exchange of slower beam ions with faster beam molecules.

Each time there is charge exchange with an ambient ion, there is an increase in the kinetic energy in the ion beam. The energy increase is given by

$$\Delta E_{cea} = (m_b v_b^2 - m_{ia} v_{ith}^2)/2 , \quad (108)$$

and the beam velocity is faster than the thermal velocity of the ambient ions  $v_{ith}$ . In fact, McBride and coworkers (1972) show that  $v_b \gg v_{ith}$  is the condition for the modified two-stream instability that is primarily responsible for heating the electrons and slowing the beam ions. Thus the energy available to heat electrons from this source is approximately  $n_a \eta E_{kb}$ , where we have neglected the ambient ion thermal energy. Therefore the energy increase per electron from charge exchange with ambient ions followed by slowing the fast ions is  $f_{ace} \eta E_{kb}$ , where  $f_{ace}$  is the fraction of ambient ions that have charge-exchange collisions with the fast neutrals. This can be calculated at any time  $t$  from the rate constant for charge exchange  $k_{cea}$  as

$$f_{ace} = 1 - \exp(-k_{cea} n_N t) . \quad (109)$$

Thus from Eqs. (107) and (109), when charge exchange with ambient ions is the dominant means of forming beam ions, CIV ionization will occur for

$$E_{kb}/I > h/(\eta f_{ace}) . \quad (110)$$

If we also consider that we have energy losses for excitation, then we expend an average energy of  $W$  each time we create a new ion pair, where  $W \approx \langle I \rangle + \kappa \langle X \rangle$ . Here  $\langle I \rangle$  and  $\langle X \rangle$  represent the average ionization and excitation energy, respectively. If we let

$$w = W / I , \quad (111)$$

we can take advantage of the correlation that  $w$  is about 1.7 for rare gases and 2.1 to 2.5 for molecular gases for fast electrons (Platzman, 1961). Our tail electrons are only moderately fast, so we expect our  $w$  values to be somewhat higher. However, in the Platzman analysis there is a contribution of 0.2 to 0.3 to  $w$  from energy that goes into the secondary electrons, and this term will also contribute to our electron heating. Thus we may expect to have  $w$  values around 1.5 to 3. After including the energy loss to excitation, the condition for CIV is

$$E_{kb}/I > h w / (\eta f_{ace}) \quad . \quad (112)$$

For example if  $h = 0.12$ ,  $w = 2.2$ , and  $\eta = 0.6$ , then  $E_{kb}/I > 0.44/f_{ace}$ . Thus,  $E_{kb}/I$  values as low as 0.44 could have some CIV ionization.

In order to increase the electron density, an energy of  $\Delta n_e w I$  must be transferred to the tail electrons. However we get an increase in the kinetic energy of the beam ions from each new ion formed, and  $\eta E_{kb}$  energy will eventually be transferred to the electrons. Thus the energy balance gives the condition for CIV to grow as

$$E_{kb}/I > w (h + \delta) / [\eta (f_{ace} + \delta)] \quad , \quad (113)$$

where  $\delta = \Delta n_e / (n_e)_0$  is the ratio of the increase in electron density to the initial electron density. Using the same values in this equation gives  $E_{kb}/I > 3.7 (0.12 + \delta) / (f_{ace} + \delta)$ , or  $2.3 / (0.5 + f_{ace})$  for  $\delta = 0.5$ . Thus  $E_{kb}/I > 1.5$  for this example. Even if  $h$  is as low as 0.01,  $w$  is as low as 1.5,  $\eta$  is as large as 0.8, then  $E_{kb}/I > 0.96 / (f_{ace} + 0.5)$  when  $\delta = 0.5$ . Thus  $E_{kb}/I < 1$  even for this example when  $f_{ace} > 0.46$ . Thus it is possible to meet the Alfven criterion of  $E_{kb}/I = 1$  for this example. Moreover we still have an additional energy source available when resonant charge exchange is rapid.

The energy gain from each resonant charge exchange is

$$(\Delta E_{kb})_{cer} = m_b (v_b^2 - v_{bs}^2) / 2 \quad , \quad (114)$$

where  $v_{bs}$  is the velocity of the beam ion that has been slowed. If we take  $v_{bs} = v_b/2$ , then

$$(\Delta E_{kb})_{cer} = 0.75(m_b v_b^2/2) \quad . \quad (115)$$

Note that there can be many resonant charge transfer collisions. Thus the total kinetic energy in the directed beam can actually increase if the resonant charge exchange frequency  $\nu_{cer} \gg \omega_{LH}$ , so that the resonant charge exchange feeds energy into the beam faster than the plasma instabilities can remove it. The equilibrium condition would be when the charge exchange rate is equal to the ion-slowing rate, which is the electron heating rate. This rate will be related to the modified two-stream instability growth rate  $\gamma$ , which is estimated as

$$\gamma \sim 0.6 f^{0.4} \omega_{LH} \quad , \quad (116)$$

where  $\omega_{LH}$  is the lower hybrid frequency (Akimoto, et al., 1985). If we assume that the resonant charge exchange frequency is equal to  $\gamma$ , then

$$\nu_{cer} = \langle \sigma_{cer} v_r \rangle n_N \sim 0.6 f^{0.4} \omega_{LH} \quad ,$$

where the relative velocity of the ion-neutral collision  $v_r \sim v_b / 2$ . For example, for  $N_2$ ,  $\sigma_{cer} \sim 3.3 \times 10^{-15}$  (Stebbing, et al., 1963), so for  $v_r = 4 \times 10^5$  cm/s and  $\omega_{LH} = \omega_i / (1 + (\omega_e / \Omega_e)^2)^{0.5} = 2 \times 10^4$  s $^{-1}$  when the ratio of the electron plasma frequency to the electron cyclotron frequency  $\Omega_e$  is 2.26, which is the value corresponding to  $n_e = 10^5$ /cm $^3$  and a magnetic field of 0.45 Gauss,  $n_N = 0.9 \times 10^{13} f^{-0.4} = (0.9 \text{ to } 2) \times 10^{13}$  cm $^{-3}$  for  $f$  values from 0.1 to 1. Thus at gas densities above this it should be possible to maintain the full energy of the fast ion beam through resonant charge transfer.

Figure 22 shows that our simulations meet this density condition for  $n_N$  around  $10^{12}$  cm $^{-3}$ . Actually there will also be elastic ion-neutral collisions, and these will change the requirement. However there should be many gases that have  $\sigma_{cer}$  values large enough that the kinetic energy of the beam ion is

replenished by resonant charge exchange faster than it is transferred to heat the plasma electrons.

In one series of runs we compared the effects of including resonant charge exchange and elastic collisions of the beam ions with the neutral beam molecules. We compared three runs: with both effects (run 86), with neither effect (88), and with only the ion-neutral collisions (91). At a neutral density around  $10^{13}/\text{cm}^3$  and  $E_{kb} = I$ , we find that the resonant charge exchange enhancement is less than the ion-neutral reduction. Thus there is more CIV ionization for the case with neither effect. This seems to result from the greater build-up of the electric field energy when there are no ion-neutral collisions. As a result of the lower field, the kinetic energy of the fast beam builds up more and a smaller fraction of this energy is transferred to electron kinetic energy. When both processes are present there is an increase in the drift energy of the beam ions by over 40 percent, but the electron kinetic energy is almost 30 percent smaller.

### 3.5.6 Summary of Simulation Results

We have shown that for conditions present in the high-density region of a beam of fast gas molecules that charge exchange and elastic collisions are important physical phenomena. It is likely that the experimentally observed onset of CIV effects at  $v_c$  calculated from the ionization energy is the result of charge exchange effects that feed additional energy into the process to compensate for the losses from the failure of the fast ions to feed 100 percent of their energy to the plasma electrons (i.e.,  $\eta < 1$ ) and from the losses to form excited states rather than ions ( $w > 1$ ). When the fraction of beam ions is low, the electrons will heat, but not enough to produce further ionization. Charge exchange with ambient (background) ions will produce the initial fast ions when the beam number density is large enough and the beam molecules have an ionization potential low enough that this process is exothermic. Some charge exchange has to take place before the electrons will heat effectively. This imposes low pressure limits on the gas beam. At

higher beam gas densities, the drift energy of the beam ions will increase until the electric field energy is maintained high enough to heat electrons in spite of the disrupting effects of elastic collisions. Resonant charge exchange will be less important in increasing the energy of the beam ions when dimer ions are present, unless the dimer concentration is a large fraction of the molecules in the beam. This may reduce the importance of dimer (and higher n-mer) formation in the CIV process. However, the effect of resonant charge exchange is to lower the energy requirement for the fast ion beam, so any contribution to the beam from dimers will be an additional way to produce CIV ionization with a low energy beam.

#### ACKNOWLEDGMENTS

Dr. H. Petscheck has contributed to the interpretation of code predictions.  
Dr. C. Rollins has acted as technical reviewer on the program, with particular emphasis on experiment design. Dr. B. David Green has provided contributions to all aspects of the program.

## REFERENCES

- Abe, T. and Machida, S. (1965), "Production of High-Energy Electrons Caused by Counterstreaming Ion Beams in an External Magnetic Field," *Phys. Fluids* 28, 1178-85.
- Albritton, D.L. (1978), "Ion Neutral Reaction Rate Constants Measured in Flow Reactors Through 1977," *At. Data Nucl. Data Tables* 22, 1-101.
- Alfven, H. (1954), On the Origin of the Solar System, Oxford University Press, Oxford, U.K.
- Akimoto, K., Papadopoulos, K., and Winske, D. (1985), "Lower Hybrid Instabilities Driven by an Ion Velocity Ring", *J. Plasma Phys.* 34, 445-65.
- Axnas, I. (1980), "Some Necessary Conditions for a Critical Velocity Interaction Between the Ionospheric Plasma and a Xenon Cloud," *Geophys. Res. Lett.* 7, 933-36.
- Birdsall, C.K. and Langdon, A.B. (1985), Plasma Physics Via Computer Simulation, McGraw-Hill, New York.
- Caledonia, G.E., Person, J.C., and Hastings, D.E. (1986), "Ionization Phenomena About the Space Shuttle," Report AFGL-TR-86-0045, Air Force Geophysics Laboratory, Hanscom Air Force Base, MA. ADA170542
- Caledonia, G.E., Person, J.C., and Hastings, D.E. (1987), "The Interpretation of Space Shuttle Measurements of Ionic Species," *J. Geophys. Res.* 92, 273.
- Chen, F.F. (1963), "Electric Probes" in Plasma Diagnostic Technologies, Huddleston, ed., Chapter 4, 116-199.
- Cobine, J.D. (1968), Gaseous Conductors, Dover, New York, p. 125.
- Danielsson, L.R. (1973), "Review of the Critical Velocity of Gas-Plasma Interaction, I: Experimental Observations," *Astrophys. and Space Sci.* 24, 459-85.
- Galeev, A.A. (1981), "Weak Turbulence Theory of an Enhanced Gas Ionization by the Plasma Flow," *Proc. of an International School and Workshop on Plasma Astrophysics*, Spec. Publ. 161 European Space Agency, Neuilly, France.
- Haerendel, G. (1982), "Alfven's Critical Velocity Effect Tested in Space," *Z. Naturforsch.* A37, 728-35.
- Hasegawa, A. and Birdsall, C.K. (1964), "Sheet-Current Plasma Model for Ion Cyclotron Waves," *Phys. Fluids* 7, 1590-1600.



- Himmel, G., Mobius, E., and Piel, A. (1976), "Investigation of the Structure and the Plasma Parameters in a 'Critical Velocity' Rotating Plasma," *Z. Naturforsch.* A31, 934-41.
- Inokuti, M. (1971), "Inelastic Collisions of Fast Charged Particles with Atoms and Molecules - The Bethe Theory Revisited," *Rev. Mod. Phys.* 43, 297-347.
- Itikawa, Y., Hayashi, M., Ichimura, A., Onda, K., Sakimoto, K., Takayanagi, K., Nakamura, M., Nishimura, H., and Takayanagi, T. (1986), "Cross Sections for Collisions of Electrons and Photons with Nitrogen Molecules," *J. Phys. Chem. Ref. Data* 15, 985-1010.
- Jackman, C.H. and Green, A.E.S. (1979), "Electron Impact on Atmospheric Gases 3. Spatial Yield Spectra for N<sub>2</sub>," *J. Geophys. Res.* 84, 2715-24.
- Kelley, M.C., Pfaff, R.F., and Haerendel, G. (1986), "Electric Field Measurements During the Condor Critical Velocity Experiment," *J. Geophys. Res.* 91, 9939-46.
- Krall, N.A. and Trivelpiece, A.W. (1986), Principles of Plasma Physics, San Francisco Press, San Francisco, CA.
- Langmuir, I. (1961), Collected Works, Pergamon Press, Vols. 3, 4, and 5.
- Loeb, L.B. (1960), Basic Processes of Gaseous Electronics, (University of California Press, Berkeley), p. 68.
- Machida, S. and Goertz, C.K. (1986), "A Simulation Study of the Critical Ionization Velocity Process," *J. Geophys. Res.* 91, 11965-76.
- Mahan, B.H., and Person, J.C. (1964), "Gaseous Ion Recombination Rates. II," *J. Chem. Phys.* 40, 2851-2859.
- McBride, J.R., Ott, E., Boris, J.P., and Orens, J.H. (1972), "Theory and Simulation of Turbulent Heating by the Modified Two-Stream Instability," *Phys. Fluids* 15, 2367-83.
- McNeil, W.J., Lai, S.T., and Murad, E. (1987), "Effect of Metastable States in Critical Velocity Ionization Processes," Paper SM31B-05 at AGU Spring Meeting, Baltimore, MD, May 19, 1987.
- Mobius, E., Boswell, R.W., Piel, A., and Henry, D. (1979), "A Spacelab Experiment on the Critical Ionization Velocity," *Geophys. Res. Lett.* 6, 29-31.
- Mobius, E., Papadopoulos, K., and Piel, A. (1987), "On the Turbulent Heating and the Threshold Condition in the Critical Ionization Velocity Interaction," *Planet. Space Sci.* 35, 345-52.
- Montgomery, D.C. and Tidman, D.A. (1964), Plasma Kinetic Theory, McGraw-Hill, Inc., New York.

- Murad, E. and Lai, S.T. (1986), "Effect of Dissociative Electron-Ion Recombination on the Propagation of Critical Ionization Discharges," J. Geophys. Res. 91, 13745-49.
- Murad, E., Lai, S.T., and Stair, A.T., Jr. (1986), "A Proposed Experiment to Study the Critical Ionization Velocity Theory in Space," J. Geophys. Res. 91, 10188-92.
- Murphy, G., Pickett, J., D'Angelo, N., and Kurth, W.S. (1986), "Measurements of Plasma Parameters in the Vicinity of the Space Shuttle," Planet. Space Sci. 34, 993-1004.
- Newell, P.T. (1985), "Review of the Critical Ionization Velocity Effect in Space," Rev. Geophys. 23, 93-104.
- Newell, P.T. and Torbert, R.B. (1985), "Competing Atomic Processes in Ba and Sr Injection Critical Velocity Experiments," Geophys. Res. Lett. 12, 835-38.
- Ott, E, McBride, J.B., Orens, J.H., and Boris, J.P. (1972), "Turbulent Heating in Computer Simulations of the Modified Plasma Two-Stream Instability," Phys. Rev. Lett. 28, 88-91.
- Papadopoulos, K. (1984), "On the Shuttle Glow (The Plasma Alternative)," Radio Sci. 19, 571-77.
- Pickett, J.S., Murphy, G.B., Kurth, W.S., Goertz, and Shawhan, S.D. (1985), "Effects of Chemical Releases to the STS-3 Orbiter on the Ionosphere," J. Geophys. Res. 90, 3487.
- Platzman, R.L. (1961), "Total Ionization in Gases by High-Energy Particles: An Appraisal of Our Understanding," Int. J. Appl. Rad. Isotopes 10, 116-27.
- Porter, H.S., Jackman, C.H., and Green, A.E.S. (1976), "Efficiencies for Production of Atomic Nitrogen and Oxygen by Relativistic Proton Impact in Air," J. Chem. Phys. 65, 154-67.
- Raitt, W.J., Eccles, J.V., Thompson, D.C., Banks, P.M., Williamson, P.R., and Bush, R.I. (1987), "Plasma Parameters in the Near Wake of the Space Shuttle," Geophys. Res. Lett. 14, 359-62.
- Raitt, W.J., Siskind, D.E., Banks, P.M., and Williamson, P.R. (1984), "Measurements of the Thermal Plasma Environment of the Space Shuttle," Planet. Space Sci. 32, 457-67.
- Samson, J.A.R. (1967), Techniques of Vacuum Ultraviolet Spectroscopy, J. Wiley and Sons, New York.

Sasaki, S., Kubota, S., Kawashima, N., Kuriki, K., Yanagisawa, M., Obayashi, T., Roberts, W.T., Reasoner, D.L., Taylor, W.W.L., Williamson, P.R., Banks, P.M., and Burch, J.L. (1985), "An Enhancement of Plasma Density by Neutral Gas Injection in SEPAC Spacelab-1 Experiment," J. Geomag. Geoelectr. 37, 883-94.

Sasaki, S., Kawashima, N., Kuriki, K., Yanagisawa, M., Obayashi, T., Roberts, W.T., Reasoner, D.L., Taylor, W.W.L., and Burch, J.L. (1986), "Gas Ionization Induced by a High Speed Plasma Injection in Space," Geophys. Res. Lett. 13, 434-37.

Schott, L. (1968), "Electrical Probes" in Plasma Diagnostics, Lochte-Holtgraven, Chapter 11, 668-731.

Siskind, D.E., Raitt, W.J., Banks, P.M., and Williamson, P.R. (1984), "Interactions Between the Orbiting Space Shuttle and the Ionosphere," Planet. Space Sci. 32, 881-896.

Stebbing, R.F., Turner, B.R., and Smith, A.C.H. (1963), "Charge Transfer in Oxygen, Nitrogen, and Nitric Oxide," J. Chem. Phys. 38, 2277-79.

Tanaka, M., and Papadopoulos, K. (1983), "Creation of High-Energy Electron Tails by Means of the Modified Two-Stream Instability," Phys. Fluids 26, 1697-99.

Torbert, R.B. and Newell, P.T. (1986), "A Magnetospheric Critical Velocity Experiment: Particle Results," J. Geophys. Res. 91, 9947-55.

Watson, G.N. (1966), A Treatise on the Theory of Bessel Functions, Second Edition, Cambridge University Press, Cambridge, U.K.

Wescott, E.M., Stenbaek-Nielsen, H.C., Hallinan, T., Foppl, H., and Valenzuela, A. (1986a), "Star of Lima: Overview and Optical Diagnostics of a Barium Alfvén Critical Velocity Experiment," J. Geophys. Res. 91, 9923-31.

Wescott, E.M., Stenbaek-Nielsen, H.C., Hallinan, T., Foppl, H., and Valenzuela, A. (1986b), "Star of Condor: A Strontium Critical Velocity Experiment, Peru, 1983," J. Geophys. Res. 91, 9933-38.

## APPENDIX

This appendix includes the as delivered Phase 0/1 Accident Risk Assessment Report for the proposed experiment to study the role of the critical ionization velocity effect in producing enhanced plasmas around the Space Shuttle. The experiment design has continued to evolve since this document was delivered and some of the information provided within is no longer appropriate. For example, the test gases are now specified as neon, xenon, nitric oxide and carbon dioxide, and the remote plasma probe is now re-designed as a passive receiver. The present experiment concept is described in Volume II of this report, which includes all viewgraphs presented at the CIV experiment Preliminary Design Review.

The safety issues discussed below remain appropriate in any event.

CRITICAL IONIZATION VELOCITY EXPERIMENT

ACCIDENT RISK ASSESSMENT REPORT

Phase 0/1 Safety Data Package

September 1987

George E. Calabrese CIV Program Manager

Andrew Lile CIV Safety Engineer

CRITICAL IONIZATION EXPERIMENT SAFETY REPORT - PHASE 0/1

TABLE OF CONTENTS

	<u>Page</u>
1. INTRODUCTION	1
2. SAFETY CONSIDERATIONS	3
2.1 Safety Certification	3
2.2 Program Safety Status Summary	3
2.3 Non-Compliant Items	3
2.4 Safety Relevant Accident/Incidents	3
2.5 Hazardous Materials	
3. SYSTEM DESCRIPTION	4
3.1 Critical Ionization Velocity Experiment	4
3.2 Flight Operations	6
4. SYSTEM SAFETY CONSIDERATIONS	10
4.1 Payload Safety Requirements Applicability Matrix	10
4.2 Gas Release Subsystem	10
4.3 Monitor Subsystem	12
4.4 Payload Support Subsystem	13
4.5 Structural Mount Subsystem	14
5. SAFETY DATA	15
5.1 Hazard List (Flight Operation)	15
5.2 Hazard Reports	15
ADDENDUM - Safety Data Package (AFGL)	

## 1. INTRODUCTION

This report provides an Accident Risk Assessment Report (ARAR), equivalent to a Phase I Safety Data Package, for the Critical Ionization Velocity (CIV) Experiment. It identifies and evaluates potential hazards for equipment and operations required for flight operations of the CIV equipment.

This report, in compliance with JSC 13830A, provides information necessary to verify that design procedures and plans comply with NHB 1700.7A. It should be noted that some data concerning the payload are still to be determined (TBD) and this document will be updated as information is available.

The CIV experiment is a part of the Infrared Background Signature Survey (IBSS) mission sponsored by the Strategic Defense Initiative Organization (SDIO). The CIV experiment will be designed, developed, and fabricated by Physical Sciences Inc. (PSI) under contract to the Air Force Geophysical Laboratory (AFGL). AFGL is developing and providing the CIV experiment with the Payload Support Subsystem as described in Subsection 4.4.

The CIV experiment involves the sequential release of four gases from the Orbiter payload bay and the observation of the resulting gas cloud from the IBSS system (IBSS, AIS, and TV cameras mounted on the RMS deployed or free flying SPAS platform) and from a CIV monitor subsystem in the payload bay. The CIV experiment consists of three subsystems: 1) a gas release subsystem with four pressure vessels and pneumatic control hardware; 2) a monitor subsystem with a series of radiometers, a Langmuir capacitance probe, and a remote plasma monitor utilizing a low power radio frequency transmitter/receiver; and 3) a payload support subsystem with a payload controller, data acquisition electronics, data tape recorder, and a battery.

The CIV experiment is mechanically configured to mount on two of Rockwell's Adaptive Payload Carriers (APC) attached to the Orbiter payload bay longeron. The electrical interface with the orbiter is through five switches

of the Payload Standard Switch Panel (PSSP) assigned to the IBSS mission which provide power to activate relays and solenoid valves that control CIV functions. The major power source for CIV equipment is a self-contained battery pack.



## 2. SAFETY CONSIDERATIONS

### 2.1 Safety Certification

AFGL and SDIO management approval and submittal of this ARAR for the safety review process constitutes certification of completeness in accordance with the requirement of JSC 13830 for Phase 0/1 Safety Data Package.

### 2.2 Program Safety Status Summary

Development of this ARAR and hazard analysis is at the Phase I stage. CIV system description, drawings, schematics, and operation have been sufficiently defined to allow assessment of the hazards relating to the payload.

### 2.3 Non-Compliant Items

Neither waivers nor deviations of safety requirements for CIV are anticipated at this time.

### 2.4 Safety Relevant Accident/Incidents

None at this time.

### 2.5 Hazardous Materials

No hazardous materials are used in CIV except for a lithium-iodine power cell utilized in AFGL's Payload Support System (refer to attachment).

### 3. SYSTEM DESCRIPTION

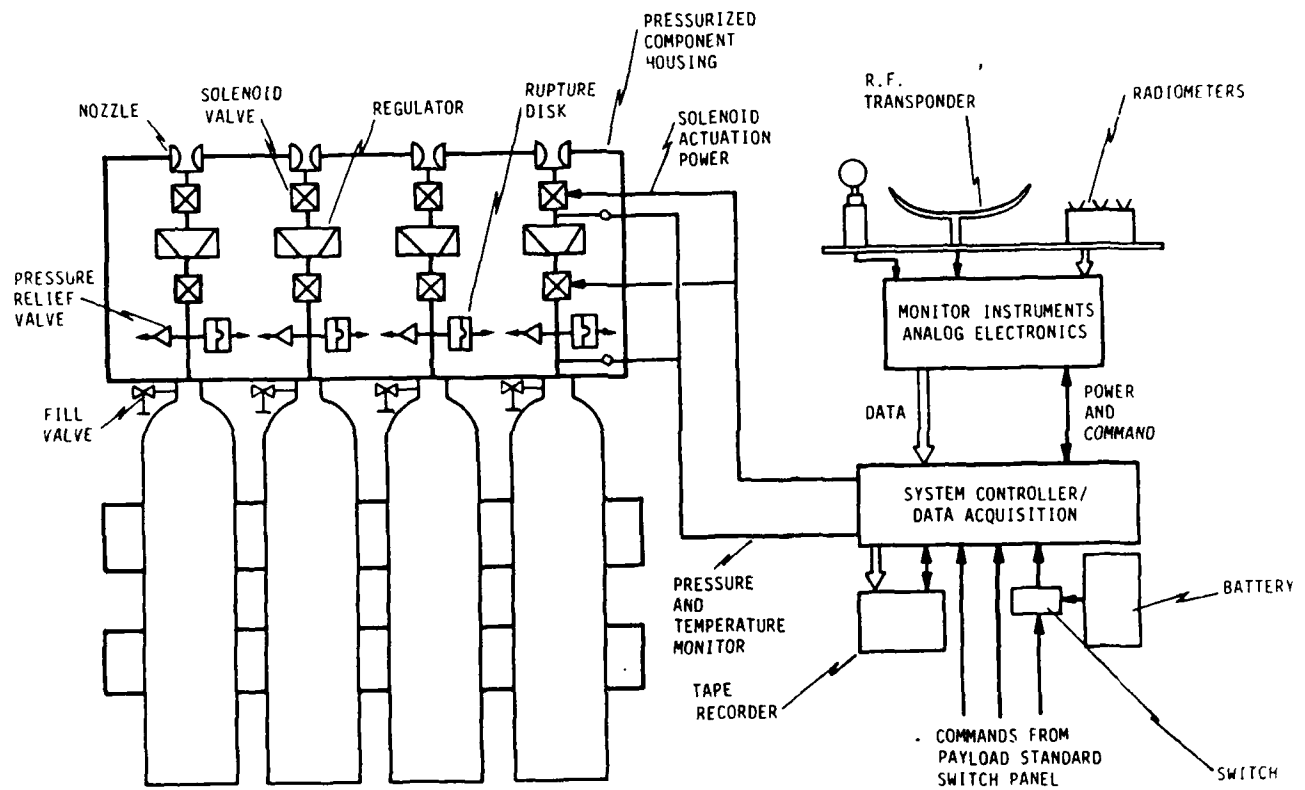
The Critical Ionization Velocity (CIV) Experiment will investigate a physical mechanism for creating ionized species whereby neutral molecules injected into the ambient low-earth atmosphere at sufficient velocity and in the pressure of the earth's magnetic field may ionize. The CIV experiment will test this hypothesis by releasing four different gases from the orbiter payload bay and monitoring the gas cloud from a self-contained CIV diagnostic package and from the free flying (or RMS deployed) IBSS platform.

#### 3.1 Critical Ionization Velocity Experiment

The CIV experiment shown in Figure 1 consists of three subsystems: the gas release subsystem, the monitor subsystem, and the payload support subsystem.

The gas release subsystem consists of a pressure vessel, safety relief valve, a pressure regulator, dual solenoid valves and exit nozzle for each of four test gases. The expansion nozzle will direct released gases parallel to the orbiter +Z axis. Pressure and temperature sensors monitor the gas conditions in each pressure vessel. The four test gases are argon (Ar), carbon dioxide (CO<sub>2</sub>), nitrous oxide (NO), and TBD.

The monitor subsystem contains three diagnostic instruments: a series of bandpass filtered radiometers, a Langmuir capacitance probe and a remote plasma monitor. The radiometers are calibrated silicon or PbS photodiodes with bandpass interference filters and apertures to limit the field of view. The Langmuir probe is a small conducting sphere mounted on a support rod which is used to make a passive measurement of the capacitance of the space around the probe. The remote plasma monitor uses a 10 watt radio frequency transmitter and receiver to measure the reflective properties of the ionized gas cloud as the radio frequency is varied.



A-6137

Figure 1. CIV Experiment Configuration

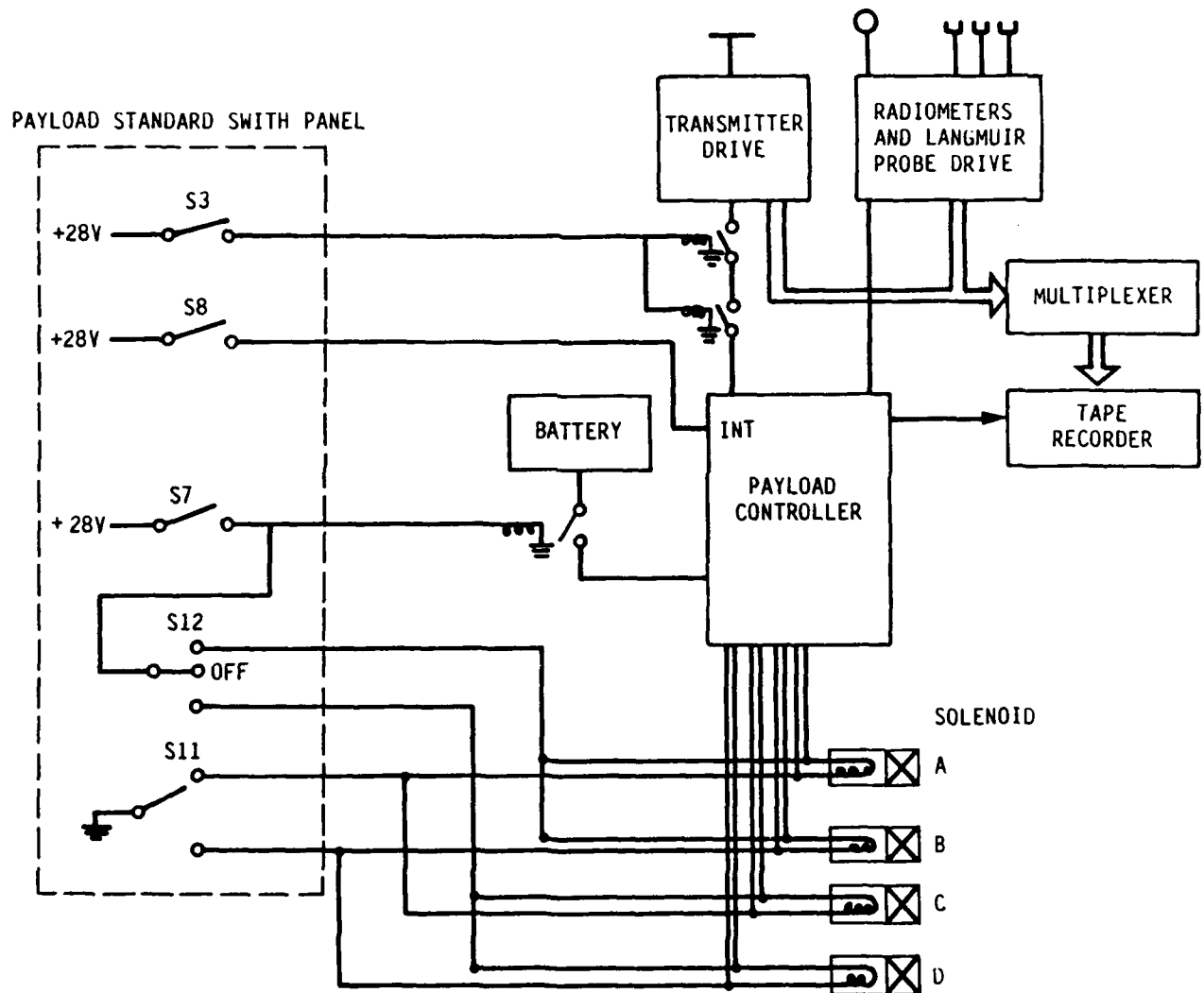
The payload support subsystem contains a programmable payload controller that coordinates CIV experiment operations, including activation of the solenoid valves for gas release in a preprogrammed sequence (additional PSSP switches can optionally activate solenoid valves directly to override the preprogrammed sequence). The data acquisition module multiplexes and formats data from the monitor subsystem instruments and the gas release diagnostic sensors and directs the data to the tape recorder. The payload support subsystem also contains a 28-volt, 50-amp-hr silver zinc battery and DC/DC converters to supply +5 and  $\pm 5$  volts to payload electronics.

The gas release subsystem is mounted on one APC and the monitor subsystem and payload support subsystem are mounted on the second APC. A wire harness will provide electrical connections for power and control between the two APC which may be mounted on opposite sides of the payload bay.

### 3.2 Flight Operations

Operation of CIV functions are initiated by a crew member on the aft flight deck through the PSSP. Three switches are utilized for baseline CIV operations, and two additional switches allow optional functions to be accomplished. The switch schematic diagrams are shown in Figure 2. The particular switch numbers referred to are for information only. Any equivalent switch would be acceptable.

CIV remains in its unpowered state until shortly before a planned gas release when the crew member activates switch S7 which drives a relay that applies CIV battery power to the payload controller. The payload controller immediately applies power to the radiometers, the Langmuir probe, and the data recorder. The payload controller also directs power to the remote plasma monitor transmitter; however, dual relays interrupt this power to inhibit transmitter operation unless switch S3 is activated. The activation of switch S3 by the crew member completes the power up and initialization of the CIV. With S7 and S3 both activated, the monitor instruments are operating and data is continually recorded.



A-6296

Figure 2. CIV Control Schematic

Prior to gas release appropriate orbiter attitude, IBBS attitude, and IBSS operational mode must be achieved. Then gas releases are initiated in one of two methods. For baseline gas releases, switch S8 is activated which produces an interrupt on the payload controller and a preprogrammed sequence of events begins. In the sequence the solenoid valve for each test gas is opened in turn for a 10-second gas release with a null period between each gas release of approximately 30 seconds.

The optional gas release method uses switches S11 and S12 to operate each solenoid valve directly, bypassing the payload controller sequencing. For such manually controlled gas releases, the crew member would first position switch S11 to the proper position, then when the gas release is desired operate switch S12. Table 1 gives typical switch positions for various gases.

Table 1. Optional Gas Release Control Switches

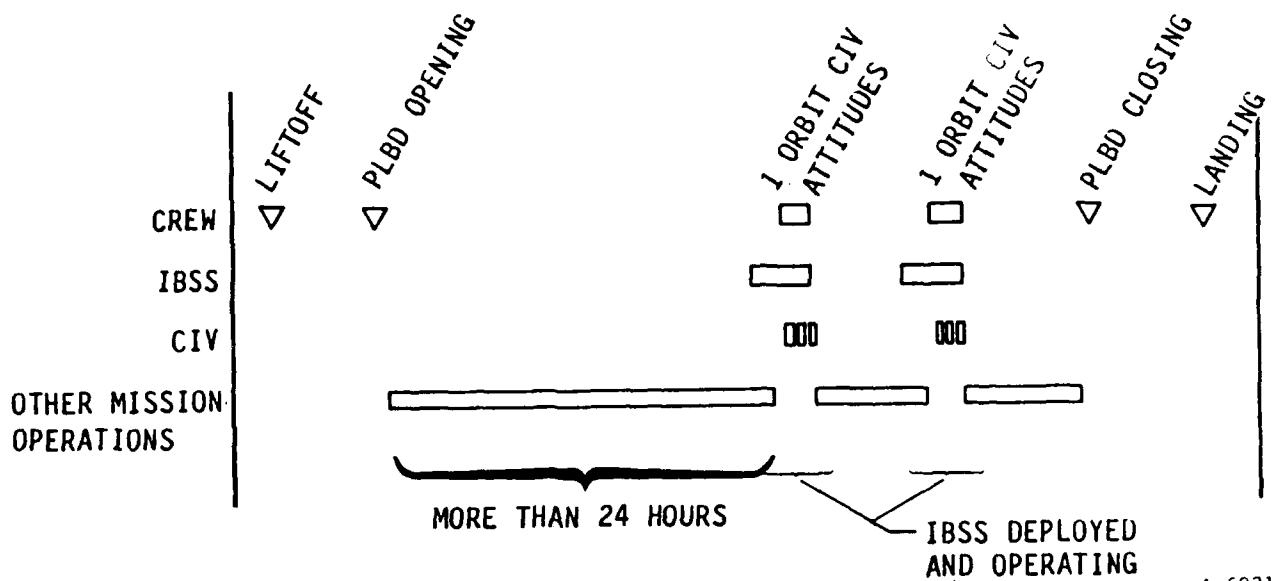
S11 Position	S12 Position	Test Gas Released
Up	Up	A
Up	Down	B
Down	Up	C
Down	Down	D

For the optional control method, the crew member would be required to manually time each gas release and the null time between gas releases.

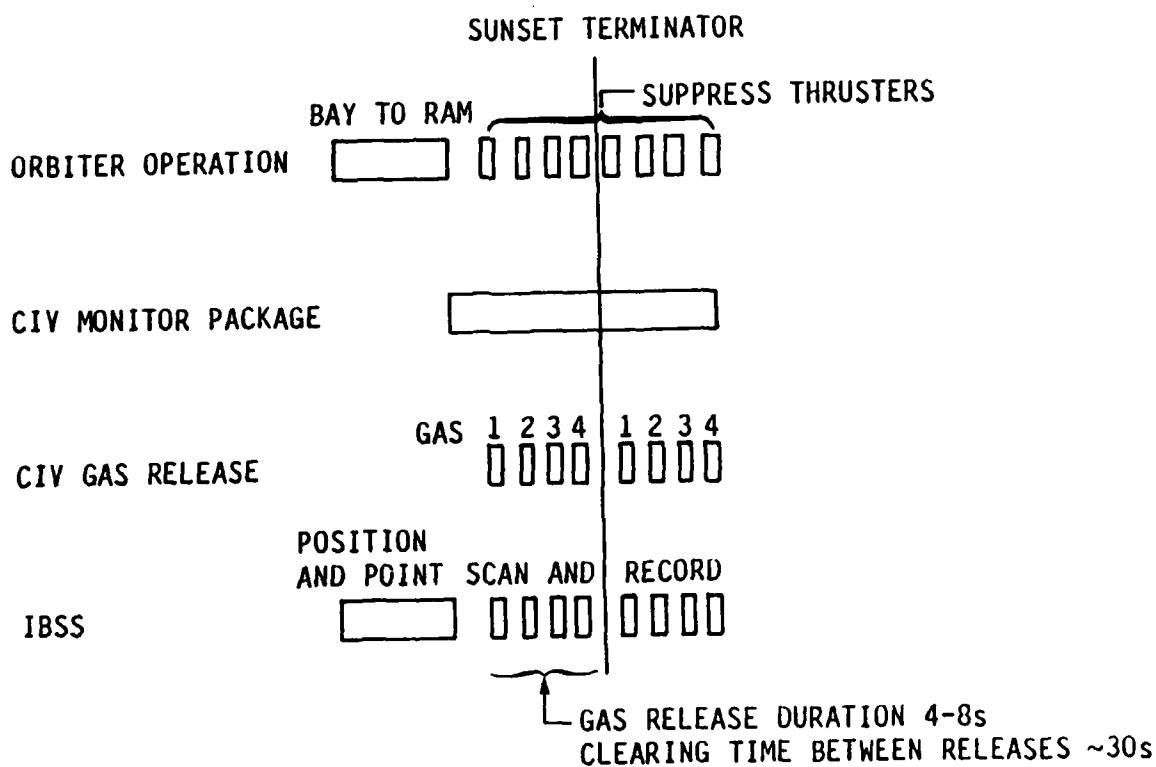
After the CIV measurement period is over, switches S3 and S7 are deactivated to terminate data acquisition and remove power from the CIV payload.

Five sets of gas release sequences are currently planned with the orbiter and IBSS in various attitudes and configurations. Depending on the length of time between gas releases, the crew member could remove power from CIV or simply leave the monitor subsystem operating.

A preliminary timeline for proposed CIV operations is presented in Figure 3.



A-6031



A-6032

Figure 3. CIV Flight Operations

#### 4. SYSTEM SAFETY CONSIDERATIONS

The CIV experiment system has been analyzed to identify safety critical components and functions in accordance with NHB 1700.7A. This section describes the results of hazard identification and discusses the general approach to hazard control in the CIV subsystems.

##### 4.1 Payload Safety Requirements Applicability Matrix

The hazard matrix for the CIV experiment is presented in Table 2.

##### 4.2 Gas Release Subsystem

Preliminary characteristics of the gas release subsystem are presented in Table 3. Identified hazards include pressure vessel explosion and collision of failed structural components.

The pressure vessels will be purchased from a manufacturer who has previously qualified the pressure vessel design for space. As such, pressure vessels will be designed, built, and tested in accordance with MIL-STD-1522A or NSS/HP 1740.1. The specified safety factor is 1.5 with a leak-before-burst design. Redundant pressure relief devices (safety relief valve and burst disk) are incorporated into the gas control system to prevent overpressurization under all thermal conditions.

All pressurized components including lines, fittings, solenoid valves, and regulators will be space qualified or military specification parts to meet guidelines of MIL-STD-1522A or NSS/HP 1740.01. All pressurized components will be rated for maximum operating pressure.

The four test gases are argon (Ar), carbon dioxide (CO<sub>2</sub>), nitrous oxide (NO), and TBD. All are non-hazardous for all flight operations. The thrust produced by the CIV gas release is small compared to the vernier reaction control system (VRCS) thrusters. Approximately 5N (1.2 lbf) of thrust is



STS PAYLOAD SAFETY REQUIREMENTS APPLICABILITY MATRIX

1 PAYLOAD/SUBSYSTEM:		2 DATE:		3 PHASE:		4 PAGE 1 OF 1	
CIV		August 1987		0/1			
5 PAYLOAD ELEMENT	Gas Release Subsystem	X		X		X	
	Monitor Subsystem	X		X		X	
	Payload Support Subsystem	X		X		X	
6		7		8		9	
NHB 1700.7A REQUIREMENTS		IMPLEMENTATION PERSONNEL		DATE		PAYLOAD ORGANIZATION PERSONNEL	
200 GENERAL		A. Lintz		Aug '87			
201 FAILURE TO EXHAUST							
202 CRITICAL HAZARDS							
203 LIQUID PROPELLANT							
204 SOLID PROPELLANT							
205 GASEOUS PROPELLANT							
206 BAY DOOR CLOSURE							
207 REMOVAL OF PAYLOAD							
208 P/L CONTINGENCY RETURN							
209 FAILURE PROXIMITY RETURN							
210 2 & 3 STRUCTURAL							
211 2 & 3 PRESSURE SYSTEM							
212 2 & 3 COMPRESSOR							
213 2 & 3 CONTAINERS							
214 2 & 3 FLAMMABLE MATERIALS							
215 2 & 3 FLAMMABLE MATERIALS							
216 2 & 3 FLAMMABLE MATERIALS							
217 2 & 3 FLAMMABLE MATERIALS							
218 2 & 3 FLAMMABLE MATERIALS							
219 2 & 3 FLAMMABLE MATERIALS							
220 2 & 3 FLAMMABLE MATERIALS							
221 2 & 3 FLAMMABLE MATERIALS							
222 2 & 3 FLAMMABLE MATERIALS							
223 2 & 3 FLAMMABLE MATERIALS							
224 2 & 3 FLAMMABLE MATERIALS							
225 2 & 3 FLAMMABLE MATERIALS							
226 2 & 3 FLAMMABLE MATERIALS							
227 2 & 3 FLAMMABLE MATERIALS							
228 2 & 3 FLAMMABLE MATERIALS							
229 2 & 3 FLAMMABLE MATERIALS							
230 2 & 3 FLAMMABLE MATERIALS							
231 2 & 3 FLAMMABLE MATERIALS							
232 2 & 3 FLAMMABLE MATERIALS							
233 2 & 3 FLAMMABLE MATERIALS							
234 2 & 3 FLAMMABLE MATERIALS							
235 2 & 3 FLAMMABLE MATERIALS							
236 2 & 3 FLAMMABLE MATERIALS							
237 2 & 3 FLAMMABLE MATERIALS							
238 2 & 3 FLAMMABLE MATERIALS							
239 2 & 3 FLAMMABLE MATERIALS							
240 2 & 3 FLAMMABLE MATERIALS							
241 2 & 3 FLAMMABLE MATERIALS							
242 2 & 3 FLAMMABLE MATERIALS							
243 2 & 3 FLAMMABLE MATERIALS							
244 2 & 3 FLAMMABLE MATERIALS							
245 2 & 3 FLAMMABLE MATERIALS							
246 2 & 3 FLAMMABLE MATERIALS							
247 2 & 3 FLAMMABLE MATERIALS							
248 2 & 3 FLAMMABLE MATERIALS							
249 2 & 3 FLAMMABLE MATERIALS							
250 2 & 3 FLAMMABLE MATERIALS							
251 2 & 3 FLAMMABLE MATERIALS							
252 2 & 3 FLAMMABLE MATERIALS							
253 2 & 3 FLAMMABLE MATERIALS							
254 2 & 3 FLAMMABLE MATERIALS							
255 2 & 3 FLAMMABLE MATERIALS							
256 2 & 3 FLAMMABLE MATERIALS							
257 2 & 3 FLAMMABLE MATERIALS							
258 2 & 3 FLAMMABLE MATERIALS							
259 2 & 3 FLAMMABLE MATERIALS							
260 2 & 3 FLAMMABLE MATERIALS							
261 2 & 3 FLAMMABLE MATERIALS							
262 2 & 3 FLAMMABLE MATERIALS							
263 2 & 3 FLAMMABLE MATERIALS							
264 2 & 3 FLAMMABLE MATERIALS							
265 2 & 3 FLAMMABLE MATERIALS							
266 2 & 3 FLAMMABLE MATERIALS							

Table 3. Gas Release Subsystem Operating Characteristics

Cylindrical pressure vessels				
Volume	- 14 liter			
Length	- 60 cm			
OD	- 20 cm			
Weight	- 14 kg			
Operating pressure	- 125 bar			
	CO <sub>2</sub>	NO	Ar	TBD
Total mass of gas (kg)	3.0	2.3	2.8	TBD
Fill pressure (bar)	35.0	125.0	125.0	< 125.0
Gas release rate (g/s)	11.0	7.5	10.0	TBD
Typical release time (s)	5.0	5.0	5.0	5.0

produced by the 5-second gas release and roughly 50 grams of gas is released. By comparison, the vernier reaction control system (VRCS) thrusters produced 114N (25 lb<sub>F</sub>) of thrust and produce a higher mass flux of species including H<sub>2</sub>O, N<sub>2</sub>, H<sub>2</sub>, CO, and CO<sub>2</sub>.

#### 4.3 Monitor Subsystem

The monitor subsystem consists of three instruments for diagnostic monitoring of the gas cloud: photodiode arrays, a Langmuir capacitance probe, and a radio frequency transmitter/receiver. The photodiode arrays are passive filter/detector packages which record the radiance of the gas cloud in various wavelength bands. The Langmuir capacitance probe is a 6-cm steel sphere which is extended on a support rod approximately 1 meter above the APC top surface. The remote plasma monitor uses a 10-watt transmitter to sweep the radio frequency while monitoring the reflected signal with a receiver. The hazards identified for this subsystem are: radiation, and collision of failed structural elements.

The active RF plasma monitor will be designed to meet the EMI allowable field strength limits specified in ICD 19001 and an analysis will be performed to insure that the RF radiation is completely compatible with all payload bay door open operations of the orbiter and other payloads. The transmitting antenna will be directed in the +Z direction through the payload bay doors. The plasma monitor will only be operated during each of four to six test gas release sequences and several short periods prior to the releases to measure background levels. The subsystem power will be off during launch and landing. Two additional relays are used as inhibits to prevent inadvertent operation of the transmitter due to payload controller EMI susceptibility or a relay failure. Because the IBSS system is expected to be free flying during plasma monitor operation, the appropriate IBSS specification/requirement (TBD) for allowable radiated field strength will be observed.

#### 4.4 Payload Support Subsystem

The payload support subsystem is an Air Force Geophysics Laboratory (AFGL) package that provides instrument control, data recording, and battery power. This subsystem was conceived to be general purpose flight hardware for small scientific payloads. AFGL is currently developing the subsystem for the Visual Photometric Experiment (VIPER) which is mounted in a GAS cannister with a motorized door assembly. The VIPER program has completed the Phase I safety review and the data package is attached as Appendix A. Currently the payload support subsystem for the VIPER program is built and component tested with subsystem level tests ongoing. Hazards associated with this subsystem are: explosion, corrosion, and/or contamination due to battery failure, fire, and collision of failed structures.

Explosion and corrosion are hazards associated with the main silver-zinc battery used to provide primary power. These hazards will be controlled by housing this battery in a sealed, corrosion proof, nylon/fiberglass box, Eagle Picher (EP) Part No. 16A10429-1. This is vented to the NASA supplied pressure relief valves. This case will be pressure tested to 22 psi. The free volume of the box will be minimized to reduce excess accumulation of gas and No. 22

Fiberglass B-50, manufactured by Johns Mansville, will be installed to contain any escaping electrolyte.

A second battery is located within the payload controller to power a real-time clock when the main battery is off. This is a Catalyst Research Corp. Model 3440 solid state lithium iodine 2.8 volt cell with a capacity of 650 milliamp-hours. Its total weight is 17.8 grams with lithium weight of 0.247 gram. It is soldered directly to the controller PC board and its hermetically sealed, welded nickel case needs no venting. Because of the battery's small size, no hazard is associated with it.

Because the payload support subsystem will be mounted directly to an APC and not in a GAS cannister, the electronics housings will be modified from their current design to make sealed enclosures that fully satisfy the appropriate structural and containment requirements.

#### 4.5 Structural Mount Subsystem

The structural mount subsystem consists of two APC plates and mounting hardware for each payload component. Each electrical component will be installed in its own structural housing and bolted directly to the APC. A mounting bracket and support structure will be designed to attach the four pressure vessels and associated fittings to the APC.

The structural design will comply with NHB 1700.7A, Para. 802. Newly designed structural components will utilize a factor of safety greater than or equal to 1.4. Fracture analysis will be performed on critical elements and redundant or fail-safe designs will be incorporated where possible. Design load factors will be based on information from ICD 19001 and from previous analyses for qualification of the APC structures.

The control and test plan for structural verification is presently being developed.

## 5. SAFETY DATA

This section includes hazard reports for each identified hazard associated with the CIV experiment flight operations.

### 5.1 Hazard List (Flight Operations)

<u>Equipment/ Subsystem</u>	<u>Hazard Report #</u>	<u>Title</u>	<u>Applicable Paragraph NHB 1700.7</u>	<u>Status</u>
All	F1	Collision of failed structural elements	208	Open
Gas release subsystem	F2	Failure of pressurized components	208	Open
Electrical	F3	Ignition of flammable atmospheres or materials	209,213,219	Open
Electrical	F4	Exposure of STS to EMI or transmitter radiation	212.2	Open
Electrical	F5	Battery explosion or release of corrosive materials into payload bay	209	Open

### 5.2 Hazard Reports

The hazard reports and appropriate annexes follow.

---

PAYLOAD HAZARD REPORT

NUMBER: F1

---

PAYLOAD: CIV

PHASE: 0/1

---

		Collision	
SUBSYSTEM: Structures	HAZARD GROUP: Corrosion	DATE: Aug 87	

HAZARD TITLE: Collision of Failed Structural Elements

---

APPLICABLE SAFETY REQUIREMENTS: NHB 1700.7, Para. 208

HAZARD CATEGORY:

X Catastrophic  
- Critical

---

DESCRIPTION OF HAZARD:

Collision of failed CIV parts with the orbiter and/or other payloads

---

HAZARD CAUSES:

Structural failure of CIV components due to:

1. Inadequate structural design
2. Faulty manufacturing and/or fabrication techniques
3. Stress corrosion cracking

---

HAZARD CONTROLS:

1. Use IBSS structural design criteria:
  - a. Ultimate factor of safety > 1.4 to IBSS design limit loads
  - b. Fail safe design (redundant structures) where possible
  - c. Fracture control to safe life > 4 times mission life where redundant structures not possible
2. Use safe design practice as in 1.
3. All materials to be selected in accordance with MSFC-SPEC-522 and all cleaning agents to be controlled by specification and manufacturing logs.

---

SAFETY VERIFICATION METHODS:

Combination of analysis, inspection, and test

---

STATUS:

Open

---

Approval

Payload Organization

STS

---

Phase 1

---

Phase 2

---

Phase 3

---

---

PAYLOAD HAZARD REPORT

NUMBER: F2

---

PAYLOAD: CIV

PHASE: 0/1

---

SUBSYSTEM: Pressure Systems HAZARD GROUP: Explosion

DATE: Aug 87

---

HAZARD TITLE: Failure of Pressurized Components

---

APPLICABLE SAFETY REQUIREMENTS: NHB 1700.7A, Para. 208

HAZARD CATEGORY:

X Catastrophic  
- Critical

---

DESCRIPTION OF HAZARD:

Explosion of pressure vessels, tubing and/or pressurized components causing release of fragments into the payload bay

---

HAZARD CAUSES:

1. Inadequate design
2. Overpressurization due to excessive temperature environment

---

HAZARD CONTROLS:

1. Pressure vessels designed, manufactured, and tested in accordance with MIL-STD-1522 or NSS/HP 1740.1 with safety of 1.5 or greater. All other pressurized components will be space qualified and/or military specification hardware with ultimate factor of safety > 4.0.
2. Space qualified pressure relief mechanism will vent gas in case of overpressurization under all thermal conditions. See attached schematic of pneumatic system layout.

---

SAFETY VERIFICATION METHODS:

1. Analysis and environmental test under full pressure - pressure vessel log
2. Test to verify safety relief on overpressure

---

STATUS:

Open

---

Approval

Payload Organization

STS

---

Phase 1

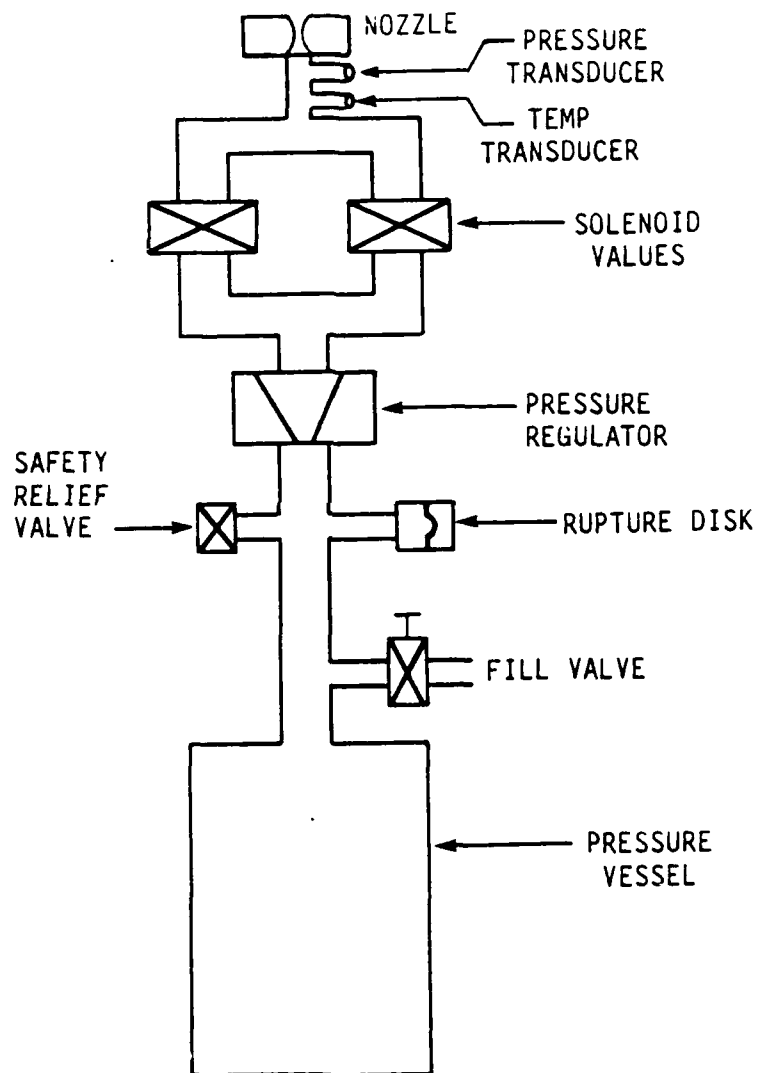
---

Phase 2

---

Phase 3

---



A-6294

CIV Gas Release Subsystem Schematic



---

PAYLOAD HAZARD REPORT

NUMBER: F3

---

PAYLOAD: CIV

PHASE: 0/1

---

SUBSYSTEM: All

HAZARD GROUP: Explosion, Fire

DATE: Aug 87

---

HAZARD TITLE: Ignition of Flammable Atmospheres or Materials

---

APPLICABLE SAFETY REQUIREMENTS: NHB 1700.7A,  
Para. 208,213,219

HAZARD CATEGORY:  
X Catastrophic  
- Critical

---

DESCRIPTION OF HAZARD:

Failure and/or overheating of electrical components causes ignition of flammable atmospheres or materials

---

HAZARD CAUSES:

1. Electrical ignition sources
2. Unrestricted flame propagation paths

---

HAZARD CONTROLS:

1. Proper design of electrical circuitry, components, and cables. Fusing utilized to limit current to appropriate level for wire size.
2. Exposed material selection in accordance with NHB 8060.1B to minimize flame propagation. See attached wiring diagrams.

---

SAFETY VERIFICATION METHODS:

- Analysis
- Review of material lists and materials assessment

---

STATUS:

Open

---

Approval

Payload Organization

STS

---

Phase 1

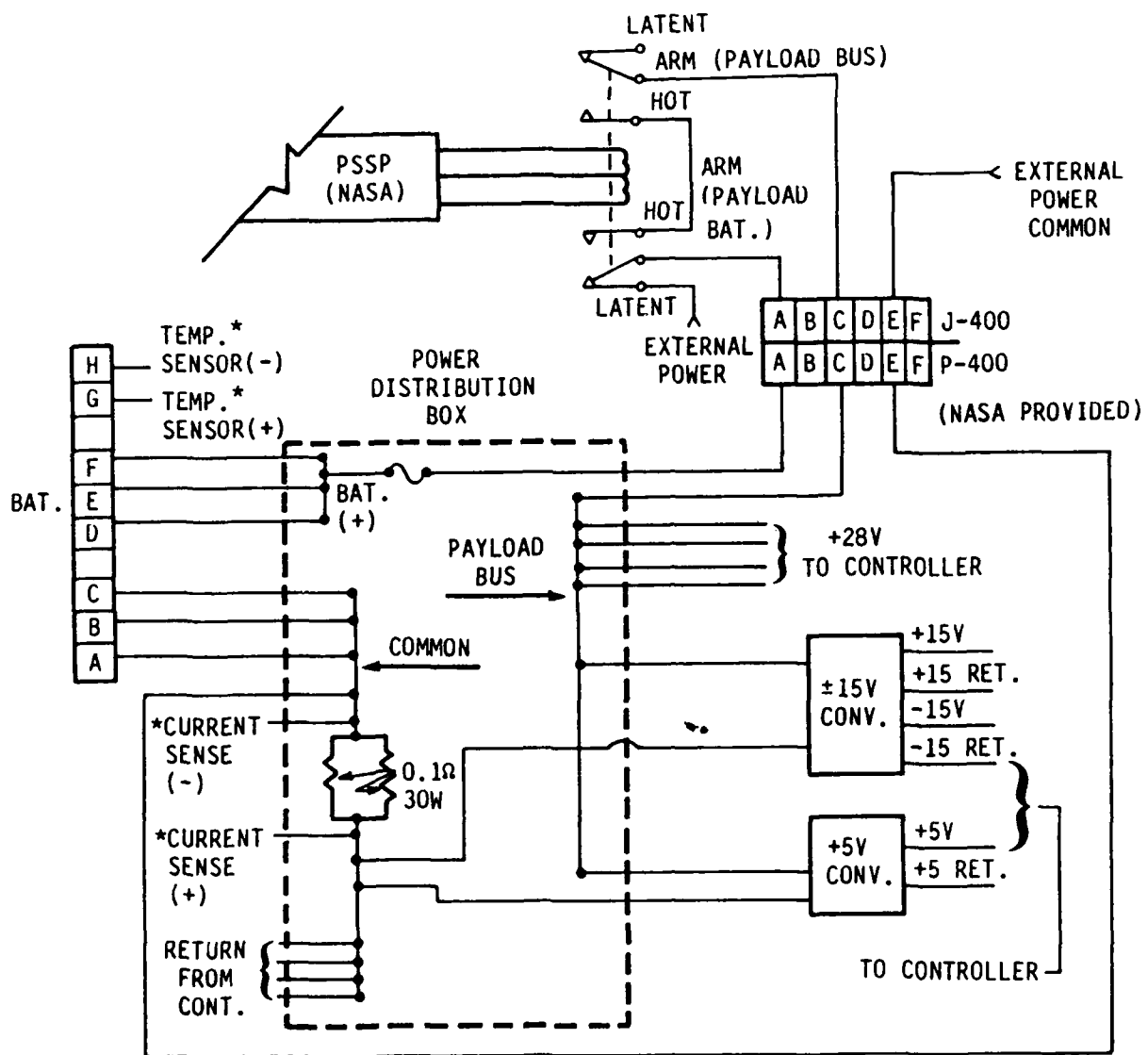
---

Phase 2

---

Phase 3

---



A-6295

Payload Support Subsystem Power Distribution Schematic

---

PAYLOAD HAZARD REPORT

NUMBER: F4

---

PAYLOAD: CIV

PHASE: 0/1

---

SUBSYSTEM: Electrical

HAZARD GROUP: Radiation

DATE: Aug 37

---

HAZARD TITLE: Exposure of STS to EMI or Transponder Radiation

---

APPLICABLE SAFETY REQUIREMENTS: NHB 1700.7A,  
Para. 212.2

HAZARD CATEGORY:  
X Catastrophic  
- Critical

---

DESCRIPTION OF HAZARD:

1. Excessive electromagnetic radiation of CIV electronics interferes with orbiter or other payloads
2. Radio wave monitor transponder generates excessive interference with orbiter or other payloads

---

HAZARD CAUSES:

1. EMI levels exceed allowance of JSC 07700 VOL XIV ATT 1 due to improper design and/or faulty shielding
- 2a. Radiation level from radio wave monitor exceeds level specified
- 2b. Inadvertant turn on of transmitter when bay doors are closed.

---

HAZARD CONTROLS:

- 1a. Design to meet ICD 19001 requirements
- 1b. Electrical bonding compliant with MIL-B-5078B/ICD 19001
- 2a. Radio wave monitor designed to meet JSC 07700 VOL. XIV ATT 1 requirements for payload bay doors open operation
- 2b. Radio wave transponder is not powered during launch and landing and three independent inhibits prevent transmitter operation (see attached)

---

SAFETY VERIFICATION METHODS:

1. System test
2. Analysis and test

---

STATUS:

Open

---

Approval

Payload Organization

STS

---

Phase 1

---

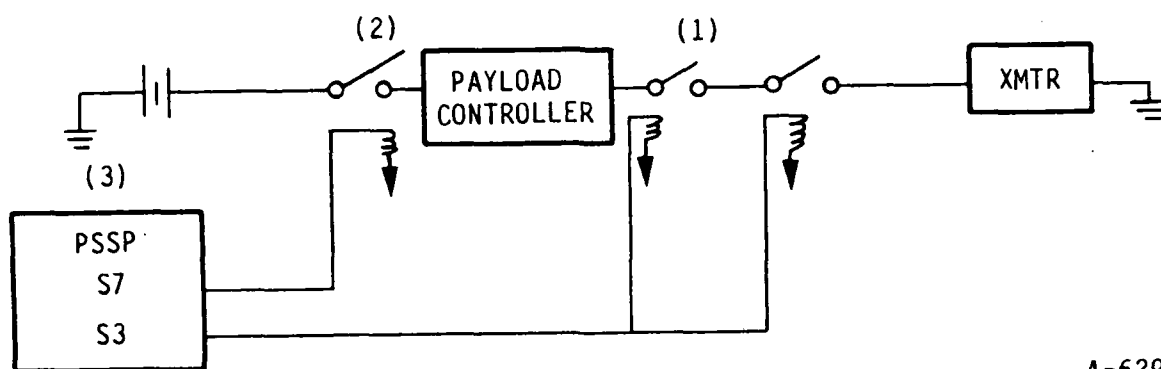
Phase 2

---

Phase 3

---

Inadvertant turn-on of the transmitter is precluded by three independent inhibits. There are three relays which must be closed before the transmitter operates (see figure below). The relays are controlled by two switches of the PSSP.



A-6297

Detailed specification of the transmitter characteristics is ongoing. Currently two different transmitter designs are being analyzed as indicated below.

Design	Operating Frequency	Output Power (Watt)	Antenna Gain (dB)	Antenna Size (cm)
Baseline	1-10 MHz Swept	1-10	1-5	50
Alternate	5 GHz Fixed	1-10	30	15

---

PAYLOAD HAZARD REPORT

NUMBER: F5

---

PAYLOAD: CIV

PHASE: 0/1

---

SUBSYSTEM: Electrical

HAZARD GROUP: Collision, Fire,  
Corrosion

DATE: Aug 87

---

HAZARD TITLE: Battery Explosion or Release of Corrosive Materials into  
Payload Bay

---

APPLICABLE SAFETY REQUIREMENTS: NHB 1700.7, Para. 209

HAZARD CATEGORY:

X Catastrophic  
- Critical

---

DESCRIPTION OF HAZARD:

Explosion/contamination/corrosion of payload bay

---

HAZARD CAUSES:

1. Excessive internal pressure due to high temperatures
2. Under or reverse voltage in cells
3. Overloads
4. Material incompatibilities or failures
5. Environmental loads

---

HAZARD CONTROLS:

1. Battery pressure relief-thermal analysis will be performed to insure adequate venting under all thermal conditions
2. Automatic switch off in undervoltage condition
3. Internal and external fusing
4. Selection of compatible materials or adequate protection
5. Compliance with structural integrity criteria

---

SAFETY VERIFICATION METHODS:

Analysis, inspection, test

---

STATUS:

Open

---

Approval

Payload Organization

STS

---

Phase 1

---

Phase 2

---

Phase 3

---